Frontal wave development over the Southern Ocean

Jérôme Patoux

A dissertation submitted in partial fulfillment of
the requirements for the degree of

Doctor of Philosophy

University of Washington

2003

Program Authorized to Offer Degree: Department of Atmospheric Sciences

University of Washington

Graduate School

This is to certify that I have examined this copy of a doctoral dissertation by

Jérôme Patoux

and have found that it is complete and satisfactory in all respects,
and that any and all revisions required by the final
examining committee have been made.

Chair of Supervisory Committee:

_____

Robert A. Brown

Reading Committee:

_____

Robert A. Brown

_____

Conway B. Leovy

_____

Greg J. Hakim

_____

Christopher S. Bretherton

Date: _____

In presenting this dissertation in partial fulfillment of the requirements for the Doctoral degree at the University of Washington, I agree that the Library shall make its copies freely available for inspection. I further agree that extensive copying of this dissertation is allowable only for scholarly purposes, consistent with "fair use" as prescribed in the U.S. Copyright Law. Requests for copying or reproduction of this dissertation may be referred to Bell and Howell Information and Learning, 300 North Zeeb Road, Ann Arbor, MI 48106-1346, to whom the author has granted "the right to reproduce and sell (a) copies of the manuscript in microform and/or (b) printed copies of the manuscript made from microform."

Signature_____

Date_____

University of Washington

Abstract

Frontal wave development over the Southern Ocean

by Jérôme Patoux

Chair of Supervisory Committee:

Professor Robert A. Brown
Department of Atmospheric Sciences

The development of frontal waves over the Southern Ocean is described using SeaWinds-on-QuikSCAT scatterometer surface winds. A planetary boundary layer model is used to construct surface pressure fields and correct the wind errors due to rain contamination and the geometry of the scatterometer antenna. The divergence and vorticity are calculated from the winds and used to diagnose frontal wave development over the Southern Ocean.

Three fronts are examined. An attribution technique is used to partition the wind field in nondivergent and irrotational components at the scale of the front and the remaining harmonic component (or environmental flow) induced by the synoptic scale flow. The front and the environment in which the front is embedded can be analyzed separately.

It is shown that frontal waves develop when the large-scale along-front stretching decreases and the environmental flow becomes frontolytic. Three of the observed frontal waves deepen into secondary cyclones. A connection with the upper-levels is observed in each case. The last frontal wave is not in a favorable configuration with the upper-levels and does not deepen significantly.

TABLE OF CONTENTS

LIST OF FIGURES

ACKNOWLEDGMENTS

I would like to thank my advisor Bob Brown for seeing the value of my tortuous path and allowing me to follow my own long winding roads. He certainly showed me a different way through the world of science and scientists, one that combines the excitement of quixotic endeavors with the satisfaction of panzaic achievement.

My thanks also go to the other members of my committee, Conway Leovy for sharing his seemingly infinite knowledge, Chris Bretherton for providing ever insightful comments, Greg Hakim for sharing his enthusiasm and penetrating understanding of atmospheric dynamics, and Jeff Richey for his encouragement.

I would like to thank Ralph Foster for guiding my first hesitant steps through the boundary layer, as well as Gad Levy and Pascale Lelong for their help and encouragement. Marc Michelsen and Neal Johnson are also deserving of many thanks.

Many friends have made this journey a fun and pleasant one. They include Jérôme Cuny, Saša Gabersek, Ian Kraucunas, Justin Sharp, John Petti, Robb Contreras and Socorro Medina. My thanks go to them and to many others, in Seattle and in France.

This dissertation and this doctoral degree are the end of an endeavor that has been possible thanks to the love, hope and dedication of a very supportive and patient family. This is now dedicated to them and to all that we, as a family, have always strived to be.

Finally, my first and last thoughts go to my soul mate, Caroline Planque, for traveling yet another road with me.

Chapter 1

INTRODUCTION

Atmospheric fronts are often persistent yet subject to instability. They are characterized by strong wind shear and a maximum in vorticity (i.e. an inflection point, in the sense of the Rayleigh criterion for instability). Given appropriate environmental conditions, perturbations can grow and extract energy from the wind shear. This is predicted by theory (Charney and Stern, 1962; Schär and Davies, 1990) and observed in satellite images and numerical analyses (Joly and Thorpe, 1990; Thorncroft and Hoskins, 1990).

In the midlatitudes, these instabilities can evolve into cyclonic systems. The secondary systems arising from a frontal instability on the trailing cold front of a mature (primary) storm are referred to as "frontal waves" and "secondary cyclones". Of intermediate scale (on the order of 1000 km), they can develop extremely fast (one or two days) and be relatively difficult to forecast.

Recently, there has been a renewed interest in frontal wave development (Parker, 1998). Several campaigns have been organized: FRONTS 87, FRONTS 92, the Fronts and Atlantic Storm Track EXperiment (FASTEX). A new insight has been gained into secondary cyclogenesis taking place on the trailing cold front of mature cyclones west of the British Isles and Western Europe (Rivals et al., 1998). However, little has been written about other regions of the world, in particular the Southern Hemisphere. Carleton (1981) describes the "instant occlusion", or "instant frontogenesis", as a comma cloud advancing upon an incipient frontal wave formation that is decelerating.

As they merge, the cyclone seems to "jump" from the incipient to the mature or dissipating stage. Although reminiscent of the frontal wave development observed over the North Atlantic Ocean, the instant occlusion has been documented only from satellite imagery and little is known of its dynamics.

In recent years, the advent of scatterometers has changed our view of the atmosphere over the oceans (Liu, 2002). Surface wind measurements are now available for almost all regions of the world ocean. Studies that were previously restricted to limited areas for technical reasons (launching and management of radiosondes, buoys, ships, etc.) can now be extended to include the whole globe and all seasons. The goal of this study is to use scatterometer data to analyze the development of frontal waves over the Southern Ocean. Few authors have used scatterometer data to study the Southern Hemisphere (Levy, 1989; Yuan et al., 1999; Milliff et al., 1999). None have used them to study frontal wave development.

Over the course of the last three years, the SeaWinds-on-QuikSCAT (QS) scatterometer was launched and has been providing an almost continuous set of surface wind measurements over most of the world ocean. On the larger scale, the recurrent period of the QS measurements provides a quasi-synoptic look at the world marine surface wind field. On the smaller scale, the 25-km grid-spacing is an opportunity to study in some detail the mesoscale features embedded in storms and fronts.

In this study, the QS measurements have been incorporated into a planetary boundary layer (PBL) model to compute surface pressure fields and estimate PBL quantities relevant to the study of storm and front development. The winds are also corrected and smoothed in the process. Divergence and vorticity are calculated and used to identify fronts and study their development. An attribution technique is used to reconstruct the environmental flow in which the front is embedded. The impact of the environmental flow on the development of the front is analyzed.

In chapter 2, a review of frontal wave theory is provided, as well as a summary of recent secondary cyclone observations. In chapter 3, the data sets and images used

in this study are presented, as well as the PBL model developed at the University of Washington, along with our ability to retrieve geostrophic winds and surface pressure fields from surface wind measurements. Chapter 4 provides general information about the Southern midlatitudes. Chapter 5 describes the methodology used to study the development of marine surface fronts and provides some results over the Southern Ocean.

Chapter 2

SECONDARY FRONTAL WAVES: A REVIEW OF CURRENT IDEAS

The Norwegian cyclone model developed by the Bergen school (Bjerknes and Solberg, 1922) does not describe the subsynoptic structures more recently observed in storms and frontal zones (Shapiro and Keyser, 1990). Whereas cyclones were originally thought to develop in sequence on the "polar front", they are now observed to develop under a wide spectrum of conditions and circumstances. In particular, mesoscale structures are thought to play a major role in the triggering and deepening of certain cyclones. A conceptual model accounting for these structures has not yet been proposed (Schultz et al., 1998).

In the 1990s, there has been a renewed interest in these subsynoptic frontal structures. Several storms of exceptional intensity have been observed and studied over the North Atlantic ocean, upstream of Western Europe. Such subsynoptic-scale cyclones are thought to develop from instabilities in the frontal zone of primary cyclones. They can deepen extremely rapidly and remain a real forecasting problem.

Since these secondary cyclones may arise from frontal instabilities, recent studies have borrowed from the classical literature on frontogenesis. The next section will provide an overview of these studies.

2.1 Frontogenesis

As a baroclinic instability grows, fronts occur as distinctive regions of the atmosphere where, in particular, the temperature gradients intensify. Quasi-geostrophic (QG)

analytic solutions have been found that could reproduce the development of a baroclinic instability (Charney, 1947; Eady, 1949) and temperature discontinuities. They led to an important result about the ageostrophic circulations taking place in the frontal region: the disruption of the thermal wind balance by the concentration of the temperature gradient is balanced by the development of an ageostrophic circulation that intensifies the vertical wind shear.

In these early studies, however, as a first approximation, the geostrophic wind alone was assumed responsible for the advection of momentum and heat. In the frontal region, this assumption breaks down. This was recently verified by Wakimoto and Cai (2002), who analyze an oceanic cold front near a "col" (i.e. a saddle point in the pressure field), a case of particular interest here (see section 4.6). Their estimate of the magnitude of the geostrophic and ageostrophic wind components are comparable. They suggest that the front is out of geostrophic balance and that the thermal wind imbalance is a result of frontogenesis.

In order to reproduce more realistic fronts, advection of momentum and temperature across the front by the ageostrophic circulation was added (semi-geostrophic equations). Infinite temperature gradients could be obtained in about 12 hours (Hoskins and Bretherton, 1972; Hoskins, 1982; Holton, 1992). In parallel, numerical simulations have attempted to reproduce ever more realistic frontal structures (Phillips, 1956; Williams, 1967, 1974). These simulations also tend to produce surfaces of discontinuity and collapsing fronts, something that is never observed in the atmosphere. This has often been blamed on the absence of diffusive effects in the simplified primitive equations used in those models. However, it is possible that ageostrophic processes alone prevent frontal collapse and explain the observation of many long-lived quasi-steady fronts (Orlanski and Ross, 1977, 1984). The respective roles played by the different frontogenetical and frontolytical processes remain uncertain.

Ley and Peltier (1978) suggest that the cross-front inertial acceleration may be-

come an important feature of the flow in the frontal region before mechanical mixing begins. They improve on the Hoskins and Bretherton (1972) model by including packets of mesoscale gravity waves propagating ahead of the front. These waves would have a wavelength of order 10 km and might explain cloud bands observed on satellite pictures and squall lines appearing in the warm sector of developing baroclinic waves. Diabatic effects are also known to play an important role in the development and stability of fronts (Orlanski et al., 1985).

Underlying the different models of frontogenesis is the assumption that there exists some interaction between the front, a mesoscale feature characterized by strong turning of the wind and consequently strong wind shear and vorticity, and the synoptic-scale flow. If we think of a front as a boundary between two air masses, characterized by a sharp temperature gradient, then this gradient will intensify as a result of the differential advection of temperature due to the synoptic-scale flow. This large-scale flow has often been modeled as a pure deformation field. The embedded front has often been modeled as a shear line (or vorticity line). In fact, most theoretical studies approach frontal development using one of the two models originally described by Hoskins and Bretherton (1972):

1. a horizontal deformation model in which the flow is purely deformational (i.e. irrotational and nondivergent)

2. or a horizontal shear model in which a frontal shear acts on an along-front temperature gradient.

As explained and illustrated in Keyser et al. (1988) (Fig. 2), a pure deformation field will act to increase the temperature gradient exponentially and rotate the isotherms toward the axis of dilatation. Shear acts to increase the temperature gradient linearly and to rotate the isotherms cyclonically (as a result of the vorticity inherent to the frontal shear) (Fig. 6 in Keyser et al. (1988)).

Keyser and Pecnick (1985) incorporated the two processes into their model by constructing a wind field from a nondivergent, irrotational and purely deformational components. Recent frontal wave studies have concentrated on the role played by the interaction between these components in the development of the secondary cyclones. Bishop (1993) suggested that the baroclinicity of a frontal region can be affected by the confluent-diffluent characteristic of a large-scale deformation flow, and that the stability of developing or decaying fronts can be affected by a large-scale strain field. He also suggested that barotropic instabilities should be suppressed more strongly by frontogenetic strain than baroclinic instabilities.

Schultz et al. (1998) found from observations of two cyclones and from idealized simulations that a large-scale confluent-diffluent flow could affect the structure of extra-tropical cyclones. If embedded in a diffluent flow, the cyclones possess a strong meridionally-oriented cold front and are reminiscent of the Norwegian cyclone model. If embedded in a confluent flow, the cyclones possess strong zonally-oriented warm and bent-back fronts, and are reminiscent of the Shapiro-Keyser cyclone model.

Data analysts who have approached frontogenesis from an observational point of view have designed various methods for extracting relevant kinematic quantities from observed surface wind fields that could be compared to the theoretical nondivergent, irrotational and deformational components described above. The attribution technique developed by Bishop (1996a,b) to extract frontal information from surface wind analyses is used here and will be described in section 5.1.

2.2 Secondary cyclogenesis

Although there is an implicit understanding in the recent literature that frontal waves and secondary cyclones take place on the mesoscale, there is no objective classification for differentiating them clearly from other types of cyclones. 1000 km is usually retained as the order of their horizontal scale. They also have significantly large

growth rates (equivalent e-folding times of less than a day). But the separation of scales between these *intermediate*-scale or *subsynoptic*-scale cyclones and *primary* cyclones is not clear-cut.

However, it is now widely accepted that the dynamics of frontal waves and secondary cyclones differ from those of synoptic-scale primary cyclones in several ways (Parker, 1998). In particular, the large-scale deformation, the frontal shear and diabatic heating are thought to play a more critical role. (Note that although they share some characteristics and dynamical features, frontal waves and secondary cyclones are technically different from *polar lows*). Because the resulting spectrum of potential frontal waves is fairly broad, observations and detailed analyses are still insufficient for establishing a general theory of secondary cyclogenesis.

In their study based on 10 years of ECMWF analyses over the North Atlantic Ocean, Ayrault et al. (1995) suggested the existence of two types of frontal waves: a "type 1" where the surface cyclone is clearly associated with an upper-level anomaly, and a "type 2" characterized by the lack of a clear precursor. They also found that the large-scale flow in which "type 2" cyclones are embedded is more frontolytic and that the baroclinicity is weaker. Joly and Thorpe (1990) suggested that all frontal waves are shallow in their early stage.

Schär and Davies (1990) modeled a mature cold front as a two-dimensional frontal surface with a band of warmer air ahead of the front (representing the "warm conveyor belt"). They found the most unstable mode to grow through mixed barotropic-baroclinic processes and to have a horizontal scale and growth rates similar to those of observed frontal waves. They suggested that the low-level warm band might be the source of low-level potential vorticity (PV) for the initiation of the instability before it deepens. The instability then connects with the upper-level troposphere and enters a fully baroclinic mode. The warm band might offer a preferred location and horizontal spatial scale for subsequent surface/upper-level interaction. They did not rule out the effect of other processes absent from their model, in particular the need

for a suitable cyclogenesis environment. Using a primitive equation model, Malardel et al. (1993) and Joly (1995) similarly showed that barotropic frontal perturbations can break the frontal flow but will saturate within two days. The perturbation will grow and the secondary cyclone will deepen only if the wave enters a fully baroclinic cycle.

The scenario outlined above has been gaining proponents over the last decade. It is now widely accepted that significantly deepening frontal waves are reinforced by an upper-level disturbance. However, the processes determining the location, scale and growth of the frontal waves in their early stage remain unclear. In particular, if frontal waves are indeed initiated by a surface PV anomaly, there is still some discussion about how the wind field, both at the frontal scale and at the synoptic scale, affects that PV anomaly.

Thorncroft and Hoskins (1990) found that the deformation inherent to a developing front can suppress frontal waves. In their analysis of a "dry" cold front, they found only weakly growing waves in the 1000-2000 km wavelength range, easily suppressed by the deformation field. When they included a simple latent heat parameterization, however, the waves were destabilized and their growth rate increased. Joly and Thorpe (1990) also noted that the latent heat released by condensation in regions of frontogenesis and frontal ascent can create a region of higher PV. Moreover, the high deformation characterizing the front in its early stage will act to distribute that PV anomaly along the axis of dilatation (i.e. approximately along the front). In their subsequent contribution (Joly and Thorpe, 1991), they modeled the front with a time-dependent basic-state and also found that latent heat release dramatically increases the growth rates. They did not consider the role of stretching deformation but found that shearing deformation favors growth in the early stages.

The impact of stretching deformation on the development of frontal waves was investigated by Bishop and Thorpe (1994, hereafter BT94). They suggested that in the early stages of frontal evolution, deformation acts to intensify the PV extremum,

but at the same time suppresses wave growth. If the along-front stretching due to the basic-state deformation field decreases under a certain threshold at a later stage, wave(s) can transition from a linear to a non-linear mode and grow out of the unstable structure. They proposed a strain rate of 0.6×10^{-5} s^{-1} as the threshold over which frontal waves cannot make that transition and therefore cannot grow significantly. This value has been used ever since in the frontal wave literature.

In a frontal wave case study, Rivals et al. (1998) adopted Bishop's perspective and used Bishop (1996a)'s attribution technique (see section 5.1) to show that the cross-frontal ageostrophic circulation plays two conflicting roles: (1) it stabilizes the front through convergence (i.e. frontogenesis) (2) it increases the potential for instability by redistributing upward the PV anomaly created by diabatic heating at the surface. Results from these last studies seem to convey the general idea that a surface PV anomaly is critical for the initiation of a secondary cyclone. They identify one mechanism for creating such a PV anomaly (latent heat release). They also stress the importance of understanding the balance between two processes: (1) the destabilization effect of the PV anomaly (2) the stabilization effect of the wind at different scales (frontal scale and synoptic scale).

In the last 20 years, several intense cyclones hitting Western Europe have been recognized to develop on the trailing cold front of mature systems. These observations have been the starting point for theoretical studies of secondary cyclogenesis and two international observation campaigns: FRONTS 92 and FASTEX (Joly et al., 1997). The observations and analyses obtained during the FASTEX campaign have shed some light on the development of several frontal cyclones (Bouniol et al., 1999, 2002; Mallet et al., 1991; Wakimoto and Cai, 2002).

Bouniol et al. (1999) presented a method for incorporating airborne radiosonde data into their analysis of the IOP16 cyclone. It revealed a low-level PV anomaly associated with the frontal surface, an upper-level anomaly associated with a dry intrusion of stratospheric air, as well as conditions favorable to moist slantwise instability, all

potential candidates for the explosion of the cyclone. In their latest contribution (Bouniol et al., 2002), they calculate the ageostrophic flow from European Centre for Medium-Range Weather Forecast (ECMWF) data using a variational analysis. They find that the coupling between the upper-level-jet and frontal ageostrophic circulation is the major process involved in deepening the cyclone.

These analyses over the North Atlantic Ocean are limited in number and in time. This is due to the difficulty and costs to organize large-scale field campaigns, but also to the fact that the fronts are short-lived. They often only span 4 to 6 synoptic-time analyses. In the above studies, the calculations are often based on 4 to 6 "snapshots" of the evolving front. Over the Southern Ocean, cold fronts can survive their parent cyclone by several days. As will be illustrated, up to 12 or 15 "snapshots" of a single front can be obtained with QS observations. This greatly improves the analysis. Moreover, the details of the mesoscale structures embedded in the front are observed with a 25-km resolution, as opposed to $1^\circ \times 1^\circ$ grid resolution at best with typical model analyses.

Chapter 3

MODELS AND DATA

The study of extratropical marine storms has evolved greatly since the era when only radiosonde data were available. The major improvement was in the form of routinely available infrared and visible satellite imagery. From the cloud signature of cyclones, inferences were made about their structure, their evolution throughout their whole life cycle and the vertical motions associated with their horizontal development. Concurrently, numerical weather prediction (NWP) models evolved and increased in resolution, to the point where frontal structures can now be represented (Atlas et al., 1999).

More recently, a whole generation of space-borne sensors has broadened the horizon even more, in particular the Seasat-A Satellite Scatterometer (SASS), the European Space Agency (ESA) Remote-Sensing Satellite (ERS) 1 and 2, the National Aeronautics and Space Administration (NASA) NSCAT and QuikSCAT scatterometers, as well as the Special Sensor Microwave Imager (SSM/I). In this study, different sets of data are used, each of which will be presented briefly.

3.1 SeaWinds-on-QuikSCAT

Since the three-month SASS mission in 1978, the first mission during which near-surface vector winds over the ocean were measured from space, meteorologists and oceanographers have been using a variety of scatterometer winds. These include the ESA ERS1 and ERS2 scatterometer wind measurements (1992 to present), as well as the NASA scatterometer (NSCAT, July 1996 - May 1997) and SeaWinds-

on-QuikSCAT (July 1999 to present) wind measurements. The three types of scatterometers have distinct features, some of which are crucial for the analysis of storm dynamics. The impact of swath geometry is illustrated in Fig. 3.1 which shows the swaths (i.e. ground surface covered) corresponding to each type of scatterometer.

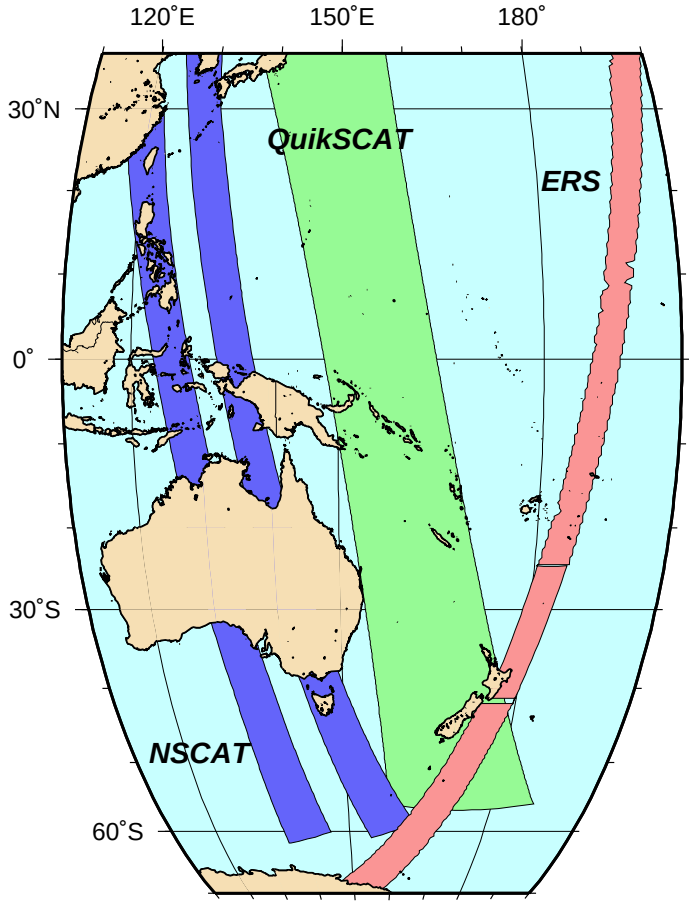

Figure 3.1: Three types of scatterometer swaths

The ERS scatterometer measured a limited amount of wind vectors in a 500-km swath at each pass of the satellite. Two consecutive swaths were relatively far apart and could hardly be used simultaneously to study the same synoptic system. NSCAT had antennas looking to both sides of the satellite track, measuring wind vectors in two 500-km swaths separated by a 200-km gap at nadir. Figure 3.2 shows how

a developing low (two lows in this case, off the coast of Japan) could be captured by NSCAT (only half of the vectors are plotted for clarity – really 12 wind vectors across each swath are measured). The corresponding ECMWF surface pressure field is

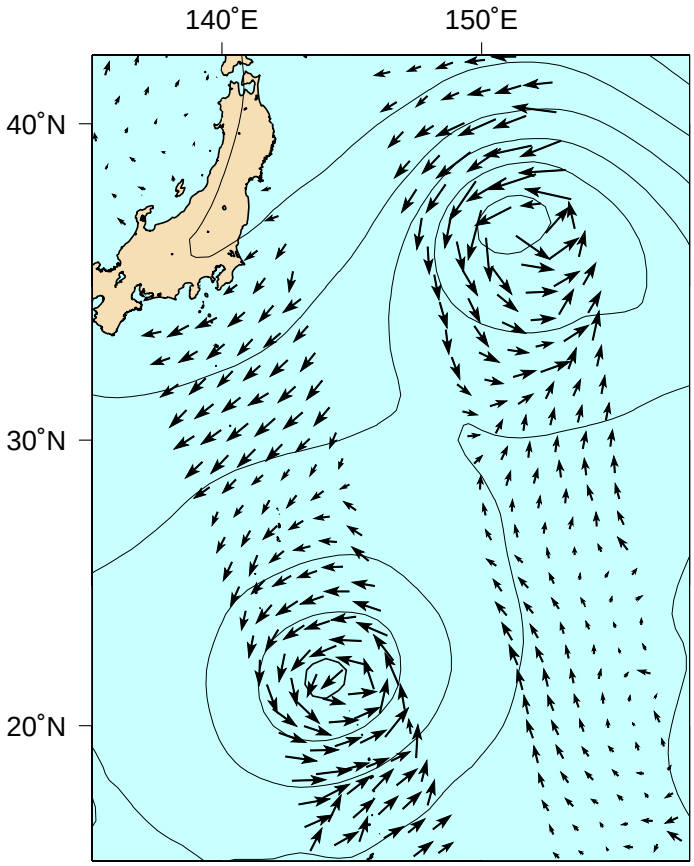

Figure 3.2: An example of the NSCAT dual swath scanning through two cyclones off the coast of Japan

plotted in the background for reference (4-mb contours). Part of the work described here was originally achieved using NSCAT data. However, because mature storms span thousands of miles and because the associated fronts can survive large distances (see chapter 5.2), the NSCAT data set is still insufficient for a thorough analysis of storm development.

In July 1999, QuikSCAT was launched with the SeaWinds scatterometer on board. With a new design, the scatterometer now scans the ocean surface with a rotating antenna and two beams at 46° and 52°. The microwave radiation emitted by the scatterometer is scattered by centimeter-scale waves at the surface of the water. The intensity and direction of these waves is dynamically related to the strength and direction of the wind stress upon the surface. The backscatter received by the scatterometer is therefore related empirically to the surface wind vector. The conjunction

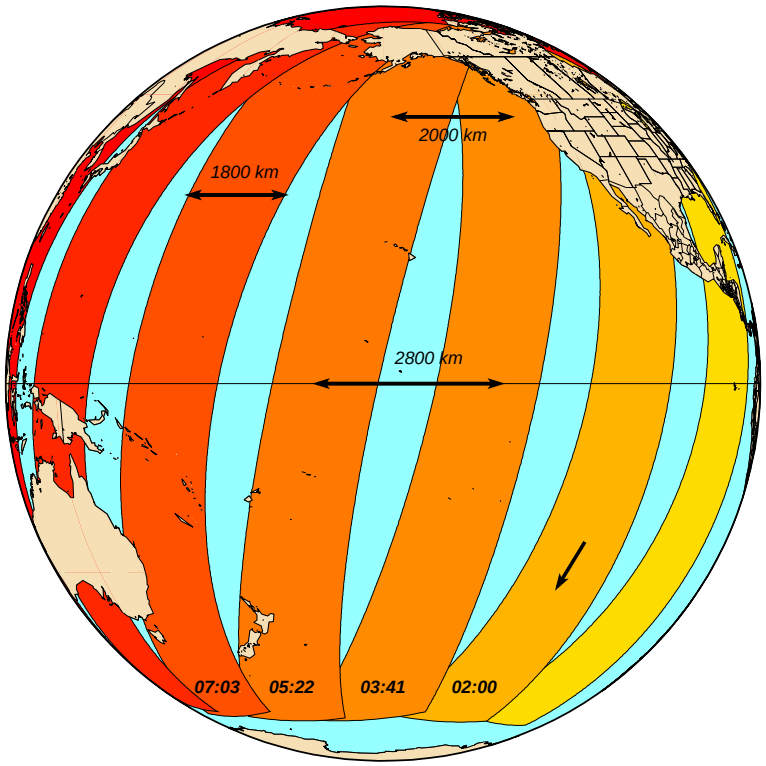

Figure 3.3: Successive QuikSCAT swaths covering the Pacific Ocean

of several looks at the same ocean unit surface element at different angles by the two antennas, and an empirical geophysical model function enable the reconstruction of a wind field with a 25-km grid-spacing. The swath is 1800 km wide (see Fig. 3.1). The orbital period is 101 minutes. Two swaths 101 minutes apart in time are separated

by 2800 km at the Equator, and roughly 2000 km in the midlatitudes. This leaves a gap of 1000 km and 200 km respectively between two adjacent swaths. The recurrent period is 4 days. This is summarized in Fig. 3.3, where several successive descending swaths are shown.

Figure 3.3 also shows that the entire Pacific Ocean, or equivalently an entire hemisphere, can be scanned by the scatterometer in 6 or 7 passes, that is less than 12 hours. Thus we can obtain "quasi-synoptic" pictures of the surface wind field. The present study takes advantage of this characteristic to obtain a quasi-synoptic history of storms and their associated fronts.

On December 14, 2002 the Advanced Earth Observing Satellite II (ADEOS-II "Midori-II") was launched from Tanegashima Space Center with a second SeaWinds scatterometer on board. Starting in April 2003, the two (identical) scatterometers will orbit the Earth in tandem and provide the current ocean coverage twice as fast (i.e. 6-hour quasi-synoptic wind fields). The dual coverage will be available until the current QS instrument is turned off, the date of which is yet to be determined.

3.2 QuikSCAT surface winds

3.2.1 The L2B dataset

The Jet Propulsion Laboratory (JPL) produces three levels of data sets. Level L1 contains the raw backscatter measurements. Level L2 contains the surface wind vectors georeferenced in swath coordinates. Level L3 is a gridded product containing averaged and interpolated surface wind values on a regular longitude-latitude grid. There also exists a QS/NCEP blended ocean wind vector dataset (Jan Morzel, Colorado Research Associates), in which the gaps between the swaths are filled with the low-wavenumber NCEP wind vectors augmented with a high wavenumber component derived from QS statistics. Hilburn et al. (2003) are developing an alternate methodology for continuously updating the global wind field at each pass of the satellite.

However, averaging artifacts are known to exist in the gridded products (Dudley Chelton, QS science team meeting, January 2003). Improved gridding techniques are still under development. The artifacts are expected to be significantly reduced during the tandem mission, due to the improved sampling of the ocean.

The L2B surface wind measurements are used here, concentrating on the period July 1999-June 2000. Hereafter, the term "swath" is used to describe a hemispheric section of the data set (as opposed to a complete orbit, covering the whole Earth, i.e. an ascending and a descending swaths approximately 180° apart). A swath contains 812 lines of vectors pole-to-pole ; each line contains 76 wind vector measurements (across the swath, i.e. roughly west-east). Because the resulting grid of vectors is dense, it is impractical to plot all of them and every other or every fourth vector will often be plotted in the following figures.

3.2.2 The limits of SeaWinds-on-QuikSCAT

Very early in the process of evaluating the quality of the retrieved surface winds, the science team was concerned with recurrent problems in the observed wind fields: an obviously erroneous directional retrieval sometimes occurs in the central and edge sections of the swath and a degenerated retrieval is performed in rainy areas. This last problem was recognized early as a contamination of the backscatter by the impact of rain drops on the surface of the water and attenuation of the signal by the raindrops.

The directional problems are due to the new geometry of the antennas. At nadir (i.e. right below the satellite), the range of azimuth angles under which the surface of the ocean can be observed is reduced to 0°and 180°(ahead and behind the satellite). Because the geophysical model function requires a broad range of azimuth angles to correctly estimate the direction of the wind, the directional retrieval is poor in the nadir section of the swath, especially when the wind happens to be oriented along the direction of the swath (roughly north-south).

On the edges, only the 52°-beam is scanning the surface of the ocean, thus re-

ducing the number of looks entering the geophysical model function from 4 to 2. Consequently, the directional retrieval is also poorer there. On top of providing a wrong wind estimate locally, this can also create artificial divergence and deformation zones which can cause a significant bias in the analysis of fronts.

3.2.3 Rain-flagging

The rain contamination has been addressed by the JPL team, who provided rain flags for wind vectors corresponding to areas of biased backscatter. An example is shown in Fig. 3.4 for a storm in the Gulf of Alaska on September 14, 1999. The black dots represent "flagged" wind vector cells (i.e. no usable data). The ECMWF surface pressure field at synoptic time (12:00 UTC) is shown for reference. In this particular case, the swath was measured at 15:00 UTC approximately, or three hours later than ECMWF. Note how convection and rain are present along the cold front and in the usually more stratiform region north of the low. This can be a significant problem in storm and front analyses. Cases where the flagged areas are too large are therefore identified and discarded.

In the rest of this study, only wind vectors flagged with "no rain" are used. It is verified that the number of wind vectors affected by rain remains small compared to the total number of vectors available and that it does not impair significantly the calculations.

3.2.4 The DIRTH filter

As a way of resolving the directional problems encountered at nadir and on the edges of the swath, the JPL team developed a median filter referred to as Direction Interval Retrieval with Thresholded Nudging (DIRTH). It basically uses the direction of surrounding wind vectors to check and correct each vector of the swath. Patoux and Brown (2001b) showed that the DIRTH algorithm removes a significant amount of

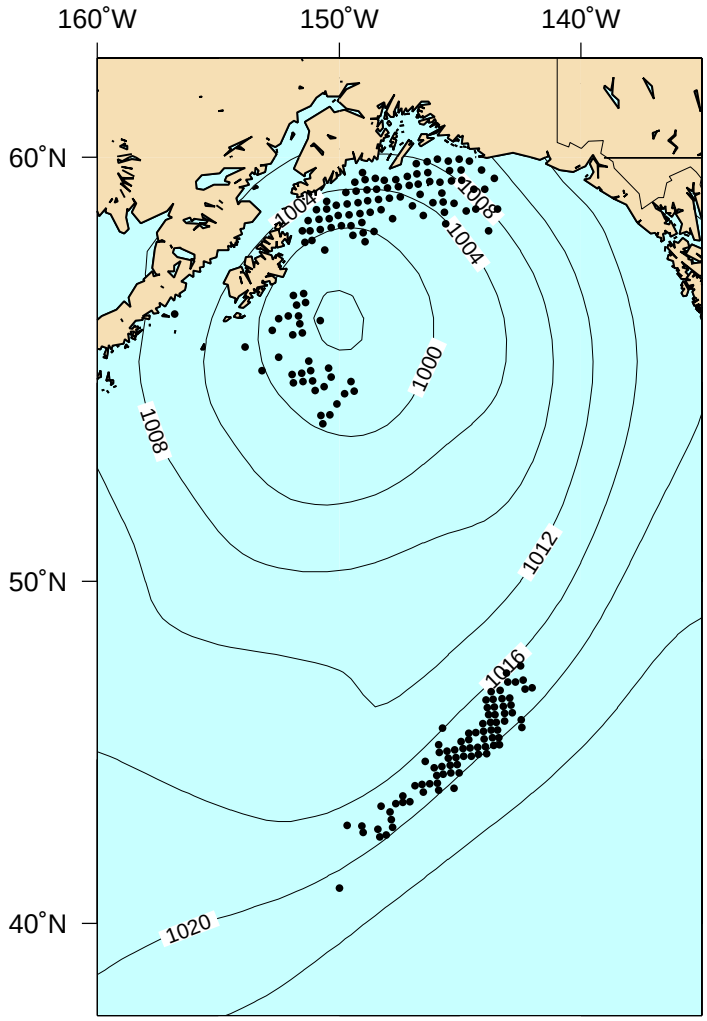

Figure 3.4: An example of rain-flagging in the Gulf of Alaska (September 14, 1999). Black dots represent flagged wind vector cells.

the small-scale variance. They performed a spectral analysis on a year of data and obtained the mean spectra shown in Fig. 3.5.

The spectral analysis was performed on the regular wind vector set, on the DIRTH wind vector set, and on both sets restricted to the sections of the swath where the directional retrieval is supposed to be more accurate (or wind vector cells 15-26 and 51-62), labeled "regular limited" in Fig. 3.5. This figure shows how the spectra agree remarkably well in the mesoscale range of the kinetic energy spectrum (1,700-200 km), but differ greatly in the small-scale range (less than 200 km), where the DIRTH spectra imply a much lower variance. Since the DIRTH algorithm "smoothes" out the wind vector field, that difference is to be expected. However, the variance of the wind vector fields limited to the sections of the swath where the directional retrieval is supposed to be of better quality (regular limited), although smaller than the variance of the regular data set, is still much larger than the DIRTH variance. There is some question as to how much of the small-scale real signal is "filtered" with the noise by the DIRTH algorithm. The assimilation of the DIRTH wind vectors rather than the regular QuikSCAT winds (i.e. as initialization data) seems to improve the forecasting abilities of NWP models (Robert Atlas, personal communication). However, a careful inspection of the DIRTH wind fields still brings some suspicion about the consistency of the wind vector fields in some cases.

Here we choose a different approach using a PBL model to correct the erroneous wind vectors. The approach is described in Patoux and Brown (2001a) and summarized in the next section.

3.3 Scatterometer-derived surface pressure

Since 1970, Brown's (1970) nonlinear equilibrium PBL model has been integrated into a wide array of tools relating dynamical conditions at the bottom and the top of the boundary layer, estimating surface pressure fields from scatterometer surface

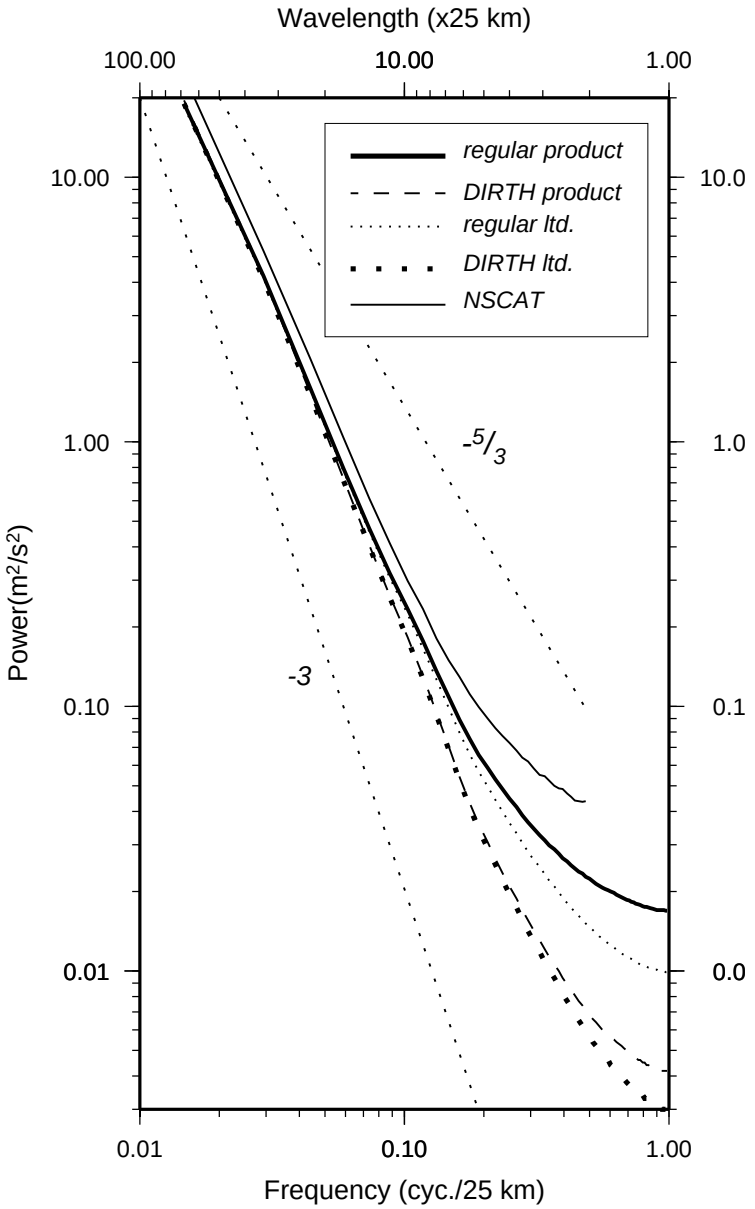

Figure 3.5: Mean energy spectra of the QuikSCAT wind fields

winds (originally SASS and NSCAT winds), as well as various schemes to estimate the role of stratification, baroclinicity, sensible and latent heat fluxes at the air-sea interface and organized large eddies (see below). Here an improved surface pressure retrieval model is used that incorporates Brown's PBL model in the midlatitudes and a mixed layer model in the Tropics. It takes advantage of the characteristics of the QS scatterometer (wide swath with a fine resolution). The midlatitude model is described in detail in a 54-page technical note (Patoux, 2000), and will be only briefly described here.

3.3.1 A two-layer similarity model in the midlatitudes

The wind profile in the boundary layer is approximated by patching a modified Ekman spiral (outer layer) to a logarithmic profile (inner layer, or surface layer, or constant-flux layer). In the outer layer:

$$\frac{U(\xi)}{G} = \cos\alpha + \frac{U_2}{G} + \frac{U_T}{G}\xi - e^{-\xi}[\cos(\alpha - \xi) - \frac{U_h}{G}\cos\xi] \tag{3.1a}$$

$$\frac{V(\xi)}{G} = \sin\alpha + \frac{V_2}{G} + \frac{V_T}{G}\xi - e^{-\xi}[\sin(\alpha - \xi) - \frac{U_h}{G}\sin\xi] \tag{3.1b}$$

where (U,V), (U_T,V_T) and (U_2,V_2) are the zonal and meridional components of the wind, the thermal wind and the secondary flow respectively (see below), and G is the magnitude of the geostrophic wind. Boundary conditions are such that the surface wind vector $\overrightarrow{U_h}$ and the surface layer profile are parallel to the x-axis. The geostrophic wind $\overrightarrow{G}$ is at an angle α with $\overrightarrow{U_h}$ (α is the *turning angle* through the boundary layer). ξ is a non-dimensional vertical coordinate:

$$\xi = \frac{z}{\delta} \tag{3.2}$$

where δ is the *Ekman depth*:

$$\delta = \sqrt{\frac{2K_M}{f}} \tag{3.3}$$

and f is the Coriolis parameter. K_M is the eddy viscosity from first-order turbulence closure theory. K_M is assumed to be constant in the Ekman layer.

In the surface layer:

$$\frac{U(\xi)}{G} = \frac{u_*}{kG}[\ln\left(\frac{z}{z_0}\right) - \psi_M(\zeta)] \tag{3.4}$$

where u_* is a turbulent velocity scale (the friction velocity) and ζ is the vertical coordinate non-dimensionalized by the stratification parameter L (the Obukhov length): $\zeta = z/L$. k is called *von Karman's constant* and is determined empirically ($k \approx 0.4$). z_0 is called the *roughness length* and its relation to u_* above the ocean is tied to the generation of waves by air-sea momentum fluxes.

The matching conditions at the patch height h_p between the Ekman layer and the surface layer yield simple similarity relations between the surface stress u_* and the geostrophic flow $\overrightarrow{G}$ (Brown, 1974, 1978, 1982). Two resistance laws are obtained:

$$\frac{kG}{u_*}(\sin\alpha + \beta) = -B \tag{3.5a}$$

$$\frac{kG}{u_*}(\cos\alpha + \gamma) = -A\prime \tag{3.5b}$$

where $A\prime$, B, β and γ are functions U_T, V_T, U_2, V_2, G, δ, the roughness length z_0, the stratification correction at the patch height and a dimensionless parameter $\lambda = h_p/\delta$. Two alternate expressions are obtained:

$$\frac{u_*}{kG} = \frac{-\gamma A\prime - \beta B + [A\prime^2 + B^2 - (\gamma B - \beta A\prime)^2]^{1/2}}{A\prime^2 + B^2} \tag{3.6}$$

$$\left(1 + \frac{B^2}{A\prime^2}\right)\sin^2\alpha + 2\left(\beta - \gamma\frac{B}{A\prime}\right)\sin\alpha + \left(\gamma\frac{B}{A\prime} - \beta\right)^2 - \frac{B^2}{A\prime^2} = 0 \tag{3.7}$$

These equations are used to determine u_* and α as a function of $A\prime$, B, β and γ.

In this analytic solution, (U_2, V_2) is a parameterization resulting from Brown's (1970) nonlinear equilibrium analytic solution. A zero-mean secondary perturbation

(u_2, v_2, w_2) was added to the mean flow and the equations of motion were solved for a modified Ekman spiral and a superimposed helical secondary flow. The finite amplitude perturbation solution was chosen to be the most unstable infinitesimal perturbation to the linear stability equation. It brings the velocity profile to a new equilibrium. The amplitude of these finite perturbation solutions is determined by an energy balance in that new stable equilibrium state. Test cases under all conditions were run and a parameterization was established.

This solution explains the irregularly turning wind profiles observed in radiosonde data, as well as the well-ordered mesoscale flows, the Langmuir-type circulations in the PBL (referred to in the literature as *coherent structures*, *helical vortices*, *instabilities*, *horizontal roll vortices* or simply *rolls*, and detected in particular with the presence of *cloud streets*).

3.3.2 The pressure retrieval model

As described earlier, a scatterometer measures the roughness of the ocean surface, from which an estimation of the surface wind vector is inferred. A *swath* of surface wind vectors is thus obtained with a 25-km spacing in the case of SeaWinds-on-QuikSCAT. These values are interpolated to a regular longitude-latitude grid.

In the midlatitudes and at each point of this grid, the surface wind vector is used as an input to the model described in section 3.3.1 to obtain an estimate of the corresponding geostrophic wind vector. The grid of geostrophic wind vectors can be viewed as a swath of zonal (p_λ) and meridional (p_ϕ) pressure gradients. We can write, in matrix notation:

$$Hx = y \qquad \text{where} \quad H \equiv \begin{vmatrix} \dfrac{1}{a\cos\phi}\dfrac{\partial}{\partial\lambda} \\ \dfrac{1}{a}\dfrac{\partial}{\partial\phi} \end{vmatrix} \qquad x \equiv P \qquad \text{and} \qquad y \equiv \begin{vmatrix} P_\lambda \\ P_\phi \end{vmatrix} \tag{3.8}$$

where a is the radius of the earth, λ is the longitude and ϕ the latitude. We can then find an approximate solution for x by a least-squares optimization scheme (Brown

and Zeng, 1994):

$$\|H^T H x - H^T y\|^2 \equiv 0. \tag{3.9}$$

The solution matrix x defines a grid of zero-mean relative pressure values. Absolute values of pressure can be obtained with a least-square fit to pressure observations such as buoy measurements. The pressures can be smoothed by applying a low-pass filter (see appendix A). A gradient wind correction is applied to the pressure fields to account for the strong curvature of the flow in highs and lows (Patoux and Brown, 2002).

The surface pressure fields produced by the original version of the UWPBL inverse model showed agreement with the NCEP Numerical Weather Prediction (NWP) and the ECMWF products within 1-2 mb in the Northern Hemisphere (Brown and Levy, 1986; Brown and Zeng, 1994). In Patoux and Brown (2002), the accuracy of the present pressure retrieval model is assessed by two methods in 14 cases of mature cyclones in the Gulf of Alaska. The first method compares the pressure difference between two buoy measurements (bulk pressure gradients ranging from 17 to 72 mb) and the corresponding pressure difference in the QS-retrieved swath of pressures. The model reproduces the buoy bulk pressure gradients with a 7% error on average. The second method calculates the mean square difference between the swath of pressures and the corresponding pressure values obtained from a NWP model. The two pressure fields are in agreement within 3 mb on average. Extreme cases were chosen on purpose to obtain an upperbound on the error. In most cases, the agreement is within 1-2 mb.

Patoux and Brown (2002) also show that major features of the pressure fields are captured by this method (e.g. position of low centers, curvature change across fronts, regions of intense winds/tighter isobars, intensity of highs and lows). The ability to determine surface pressure fields from scatterometer wind fields has also been demonstrated by Harlan and O'Brien (1986), Zierden et al. (2000) and more recently by Hilburn et al. (2003).

3.3.3 Surface pressure in the Tropics

As we approach the equator, the Coriolis force decreases and the midlatitude model fails to approximate the boundary layer dynamics correctly, primarily due to its assumption of Ekman layer dynamics and its lack of entrainment processes. The Ekman depth becomes infinite and the modified Ekman spiral model is not valid. The surface pressure retrieval model has been recently extended to include the Tropics with a simple mixed layer model in which entrainment at the top of the PBL is parameterized. Since the tropical PBL model is not used in this study, the reader is referred to Patoux et al. (2002).

An example of a QS-derived pressure field is shown in Fig. 3.6 and compared with the corresponding ECMWF analysis.

3.3.4 Correcting the QS winds

The surface pressure fields are obtained by calculating the geostrophic wind vectors from the surface wind vectors through a PBL model. The inverse calculation can be performed to obtain a new set of surface wind vectors from the geostrophic wind vectors (or equivalently, from the pressure field). Because the pressure field is smoothed by the pressure fit (Eq. 3.9) and can be smoothed further with a low-pass filter (appendix A), the new set of surface winds will also be smoother. In particular, it can be used to correct the erroneous wind vectors due to rain contamination and antenna geometry, as explained in Patoux and Brown (2001a). Because this method does not use only the surrounding wind vectors (like DIRTH) but the whole pressure field at the synoptic scale, the wind vectors can be corrected in patches of different sizes and are consistent with the flow at different scales.

An example is shown in Fig. 3.7. Panel a shows a section of a QS swath in the vicinity of a front. The original QS vectors are plotted in gray. The UWPBL-derived winds are plotted in black and fill the gaps where rain was probably contaminating

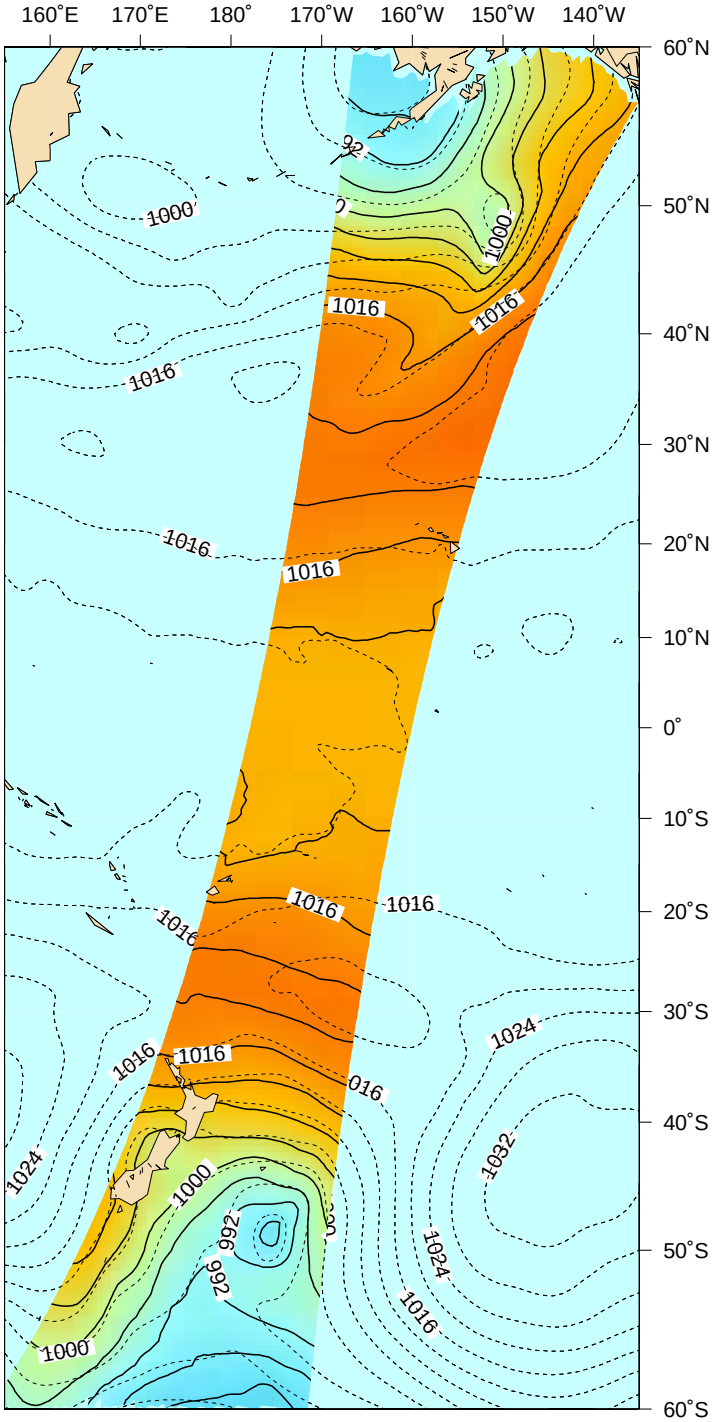

Figure 3.6: Comparison between the final pressure field calculated from QS data at 05:30 UTC (solid lines) and the corresponding ECMWF pressure field at 06:00 UTC (dashed lines), on September 20, 1999. Labels appearing inside (outside) the swath refer to the QS-derived (ECMWF) contours.

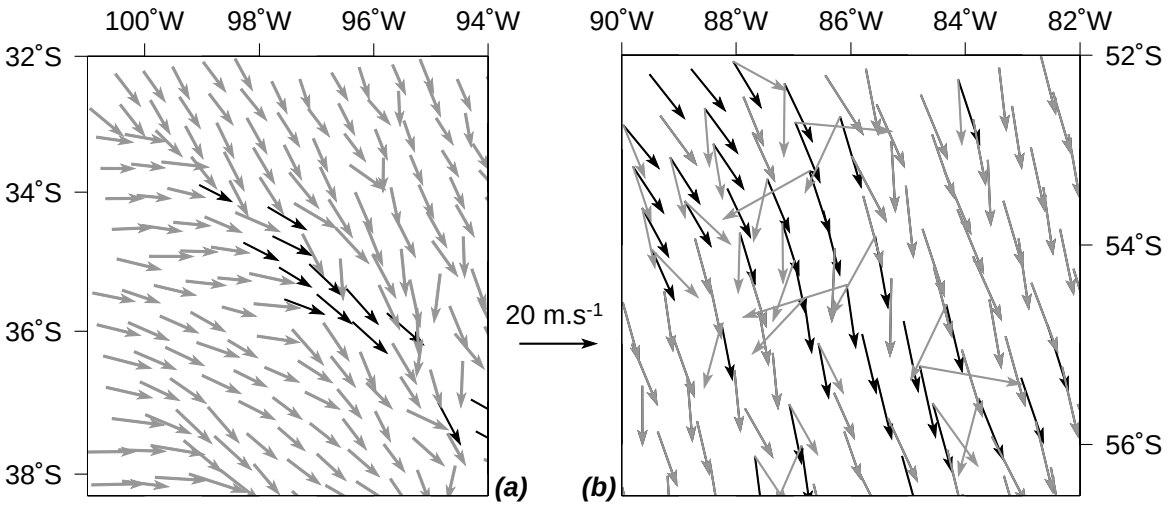

Figure 3.7: (a) Filling the QS gaps with wind vectors calculated with the UWPBL model (black vectors) (b) Correcting the erroneous QS wind vectors (gray) at nadir with UWPBL-derived surface winds (black)

the signal. Panel b shows another section of a QS swath at nadir in which some of the original vectors (in gray) can be seen to follow an erratic behavior. The UWPBL-derived vectors are plotted in black and will replace the erroneous QS vectors in subsequent analyses. These two examples are chosen in challenging areas of the swath or rainy conditions. In general, the UWPBL-derived winds simply reproduce the QS winds.

Figure 3.8 compares the UWPBL-corrected winds and the DIRTH winds. Panel (b) shows a set of original QS wind vectors in an extreme case of degenerated winds at nadir. Panel (a) shows the UWPBL-corrected winds. Whereas the small-case variability (real physical signal or noise) is conserved, the larger-scale flow has been corrected to convey a more consistent picture of the wind field. Panel (c) shows the DIRTH winds. The small-scale variability has been removed, which can be advantageous for some applications (e.g. less noise when forcing ocean models). However, a large number of suspicious wind vectors are still present.

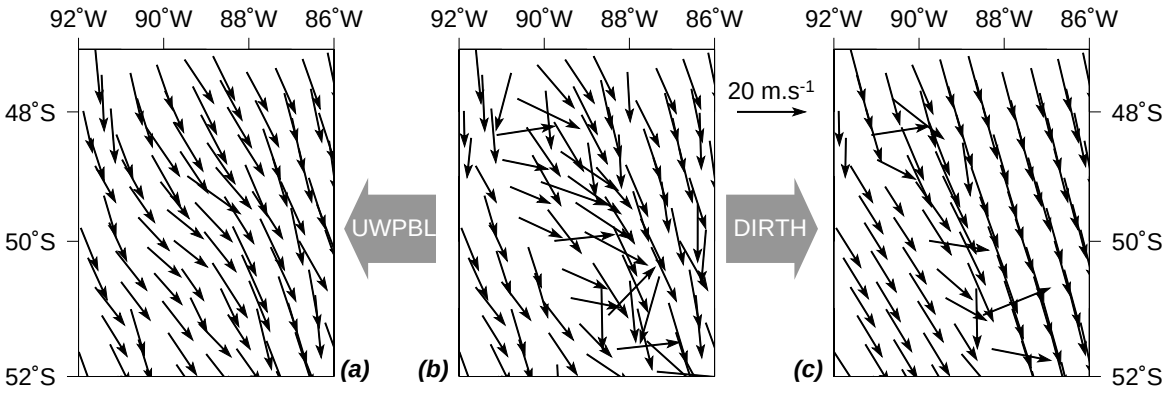

Figure 3.8: Comparison of two methods for correcting erroneous QS wind vectors. (a) UWPBL winds. (b) Original QS winds. (c) DIRTH winds.

Further comparisons will be possible when the two SeaWinds scatterometers fly in tandem. In the meantime, the UWPBL method is preferred and the corrected winds will be used in the rest of this study.

3.4 ECMWF

For the period July 1999-June 2000, the ECMWF standard model outputs were used. These are provided on a 1.25°×1.12°longitude-latitude grid. The surface pressure fields were used for comparisons and as a background reference for the UWPBL pressure fitting when necessary (i.e. as an *anchor*; see section 3.3.2). The surface air temperature, surface sea temperature and relative humidity were also used when running the UWPBL model in stratified and/or baroclinic mode. ECMWF outputs were used at synoptic time 00:00 and 12:00 UTC.

3.5 NCEP GDAS

As a means of analysis and of comparison with the UWPBL surface pressure fields, the NCEP GDAS surface pressure fields for the period September 20-25, 1999 were

used (courtesy of Tsann Wang Yu). GDAS uses the Medium Range Forecast (MRF) model [now Global Forecast System (GFS)] to generate a six-hour forecast. With a 3D variational analysis scheme, it combines global observations with the six-hour forecast to produce a cycle of analysis fields (Parrish and Derber, 1992) at 00, 06, 12, and 18:00 UTC. It is important to note that these are not forecasts, or initialization data, but analyzed fields in which, in particular, scatterometer observations have been included (ERS 1/2). It is thus an improved product (compared to ECMWF) for comparisons with the UWPBL surface pressure fields obtained from QuikSCAT data. Moreover, GDAS fields have a $1^\circ \times 1^\circ$ resolution. Four fields a day are available from GDAS.

3.6 Southern Hemisphere composite satellite imagery

Because the lack of measurements is an obstacle in the Southern Hemisphere, the availability of satellite imagery is crucial for the study of Southern Hemisphere extra-tropical storms. The composite satellite images produced by the Global Hydrology Resource Center (GHRC) are used here, hourly images covering most of the planet and constructed from the measurements of the four geostationary satellites GOES-8, GOES-10, GMS-5 and METEOSAT-7.

Chapter 4

EXTRATROPICAL STORMS IN THE SOUTHERN HEMISPHERE

Since this study concentrates on frontal waves developing over the Southern Ocean, a brief overview of our current knowledge and understanding of Southern Hemisphere synoptics will first be provided, followed by a description of the method used to identify and track midlatitude storms using QS data. This will serve as a background before concentrating on mesoscale features embedded in fronts.

4.1 Overview of the meteorology of the Southern Hemisphere

Extratropical cyclones of the Northern Hemisphere have been studied extensively in the past. In the Southern Hemisphere, however, only regional studies have been conducted in the Australasian sector and in the vicinity of South America. Climatologies have been constructed from ECMWF and NCEP analyses (Sinclair, 1997; Sinclair and Revell, 2000; Simmonds, 2000; Simmonds and Keay, 2000). However, detailed analyses of storm development are crucially lacking over a large part of the Southern Ocean. In their review of the meteorology of the Southern Hemisphere, Reeder and Smith (1998) note that although the fundamental dynamics underlying storm development can be expected to be similar in both hemispheres, regional topography plays a major role in modulating this development. The extent to which the current understanding of Northern Hemisphere extratropical cyclones can be carried over to the Southern Hemisphere is uncertain.

The scene designed by nature in the Southern Ocean is strikingly different from

the Northern Hemisphere: 80% water and an unobstructed corridor for cyclones to circle through and around the pole. The tip of South America is the only real obstacle on their way, although the presence of Africa and Australia is also critical in understanding the preferred regions of cyclogenesis. Poleward of 60°S, storms run over an ice sheet whose extent varies throughout the year. Poleward of 65°S, the 3000 meter-high continent of Antarctica completely alters the dynamics of the lows that made it up to that latitude (i.e. shrinking of the vortex column).

Bromwich and Parish (1998) give a good general description of the meteorology of Antarctica. The presence of the cold Antarctic continent induces an almost permanent baroclinic zone separating cold continental air from warmer maritime air. In turn, the intensified temperature gradient supports a large thermal wind and strong upper-tropospheric westerlies. By and large, the circulation is characterized by subsidence of cold air at the pole and a strong katabatic flow off Antarctica feeding extremely cold air into the cyclones revolving around the continent. It is possible that the topography enhances the confluence of the katabatic flow in preferred locations, in turn favoring cyclogenesis in those regions. The contrast between the ice- or snow-covered continent with surrounding ice sheet and the warmer waters probably plays a major role in both the maintenance of the baroclinic zone and the heat fluxes at the air-sea interface. Yuan et al. (1999) found a correlation between three groups of storms identified with the NSCAT 1996 winds and extrema in sea ice extent. Monthly and seasonal means of the QS surface winds also seem to describe patterns that follow the extent and shape of the ice sheet (Tim Liu, personal communication).

Extratropical cyclones evolve eastward and poleward and decay when they cross over the 60-65° region. They are an integral part of the thermally direct circulation characterizing the Antarctic continent. Warmer air is drawn into the circumpolar vortex at middle- to upper-tropospheric levels, converges and subsides, and regains more northerly latitudes in the form of the katabatic wind. The rising branch appears to be associated with cyclone activity between 65°S and 55°S (Bromwich and Parish,

1998).

In discussing the cyclonic activity on a larger scale, Bromwich and Parish (1998) note that the Antarctic continent serves as an anchor for the upper-level circulations and limits the variability of the polar trough and the storm tracks. However, the frequency of cyclonic activity in the Southern Hemisphere is higher than in the Northern Hemisphere, with a peak in August (Carleton, 1981). Sinclair and Revell (2000) extract 4 categories of extratropical cyclogenesis in the Southern Hemisphere from their composite analysis. Three categories involve a direct interaction with the entrance or exit region of the upper-level jet. Cyclones in the fourth category form beneath an intense pre-existing upper-level trough.

At the scale of individual storms, the relative importance of the factors possibly affecting cyclone development in the Southern Hemisphere is still unclear. A general view of the life cycle of individual cyclones as well as how they might be inter-connected is still missing.

4.2 Observations over the Southern Ocean

The advent of satellite imagery certainly improved the description of Southern Hemisphere storms. Carleton (1981) describes different modes of extratropical cyclogenesis as analyzed from satellite pictures. He mentions the development of vortices in the vicinity of fronts, but can only identify the different dynamic components using their cloud signature. His description of the *instant occlusion* or *instant frontogenesis* is reminiscent of the frontal waves observed over the North Atlantic. It seems to be related to strong meridional blocking and cold air outbreak occurring to the west of a major long wave trough.

Little has been done to tie these observations to quantitative measurements such as surface wind vectors. Obviously, the absence of routine measurement of the necessary dynamical quantities has always been and is still a major constraint to such

analyses. McMurdie and Katsaros (1991) use the Seasat and Nimbus-7 Scanning Multichannel Microwave Radiometers (SMMR) measurements to study the water vapor distribution in cyclones over the global ocean. Levy and Brown (1991) and Levy (1994) built a picture of surface winds and synoptic weather over the Southern Ocean from SASS winds. They detected the presence of storms that were 10-20 mb deeper than predicted by the Australian Bureau of Meteorology (ABM) and the ECMWF analyses. They also found large differences in the positioning of the storm centers. 10 years later, increased resolution in the numerical models, together with initialization with satellite data (including NSCAT and QS) has improved the analyses. Still, such discrepancies can be detected between NCEP and the UWPBL-derived pressure fields on a regular basis. In a recent study, Hilburn et al. (2003) detected major storm events in their Southern Hemisphere scatterometer-derived pressure fields that were largely underestimated in the NCEP/NCAR reanalyses (by as much as 20 mb).

The extensive coverage of the Southern Ocean by SeaWinds-on-QuikSCAT and its higher resolution are undoubtedly significant improvements for the analysis of cyclones and fronts, as will now be illustrated.

4.3 A quasi-synoptic look at storms

By running the pressure retrieval model (see section 3.3.2) on 7 successive QS orbits (ascending and descending swaths), a *quasi-synoptic* picture of the surface of the atmosphere can be obtained. The term *quasi* is used because the individual orbits are separated by 101 minutes. Figure 4.1 shows an example of such a plot.

Since each pressure swath is a swath of relative pressure values, a coherent picture is obtained by matching in a least-square sense the individual swaths to the same background ECMWF pressure field (the swath times are centered around the ECMWF synoptic time). This ensures that the absolute isobars roughly match from one swath to the next without changing the structure of the pressure gradients inside

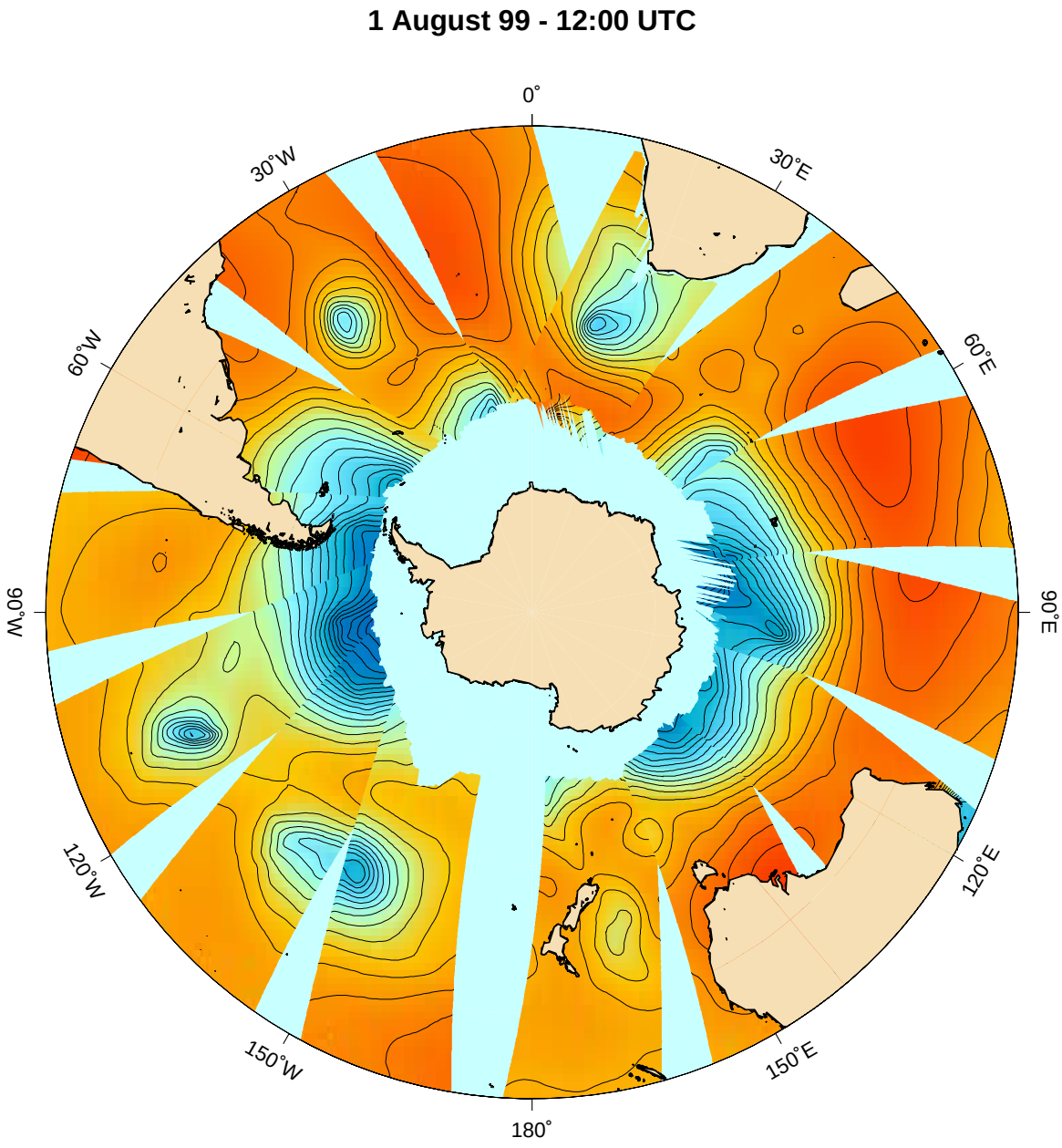

Figure 4.1: Quasi-synoptic hemispheric view of the Southern Ocean obtained by running the pressure retrieval model on seven consecutive QuikSCAT orbits

each swath. For reference, the ECMWF field corresponding to Fig. 4.1 is shown in Fig. 4.2.

As can be observed, the pressure field obtained by running the pressure retrieval model on the QS data is very similar to ECMWF. Similar in the average pressure values, of course, since the swaths are matched against ECMWF. But also similar in structure, with more detail in some satellite-derived cases (e.g. sharper curvature change across fronts, deeper lows).

Similar plots were created for the July 1999-June 2000 period and animated along with the divergence of the QS winds (see below). Storms and fronts of interest were identified and documented. The analysis presented in chapter 5.1 was then applied to these particular fronts.

4.4 Observations of fronts by QuikSCAT

There is now ample evidence that scatterometer winds contain more information than is available from model analyses (Atlas et al., 1999). Early on in the examination of the QuikSCAT wind vectors, outstanding features could be detected, in particular strongly marked convergence or shear lines and very detailed cyclonic structures. Yeh et al. (2002) describe the propagation of a front from Southern China to Taiwan typical of the mid-May to Mid-June period (a "mei-yu" front). They show that the positioning of the front, identified as the wind shift line in synoptic analyses, is substantially improved by using QS winds. Cyclones and fronts present some characteristics that GCMs have rarely produced. Only when decreasing the resolution of the Goddard Earth Observing System GCM to $0.5^\circ \times 0.5^\circ$ do Conaty et al. (2001) produce frontal features that are "reminiscent of those seen in high-resolution scatterometer wind data" (pp 1854).

An example of a mature cyclone in the Southern Hemisphere is shown in Fig. 4.3. Note the strong winds wrapping around the low, the area of very low wind speed in

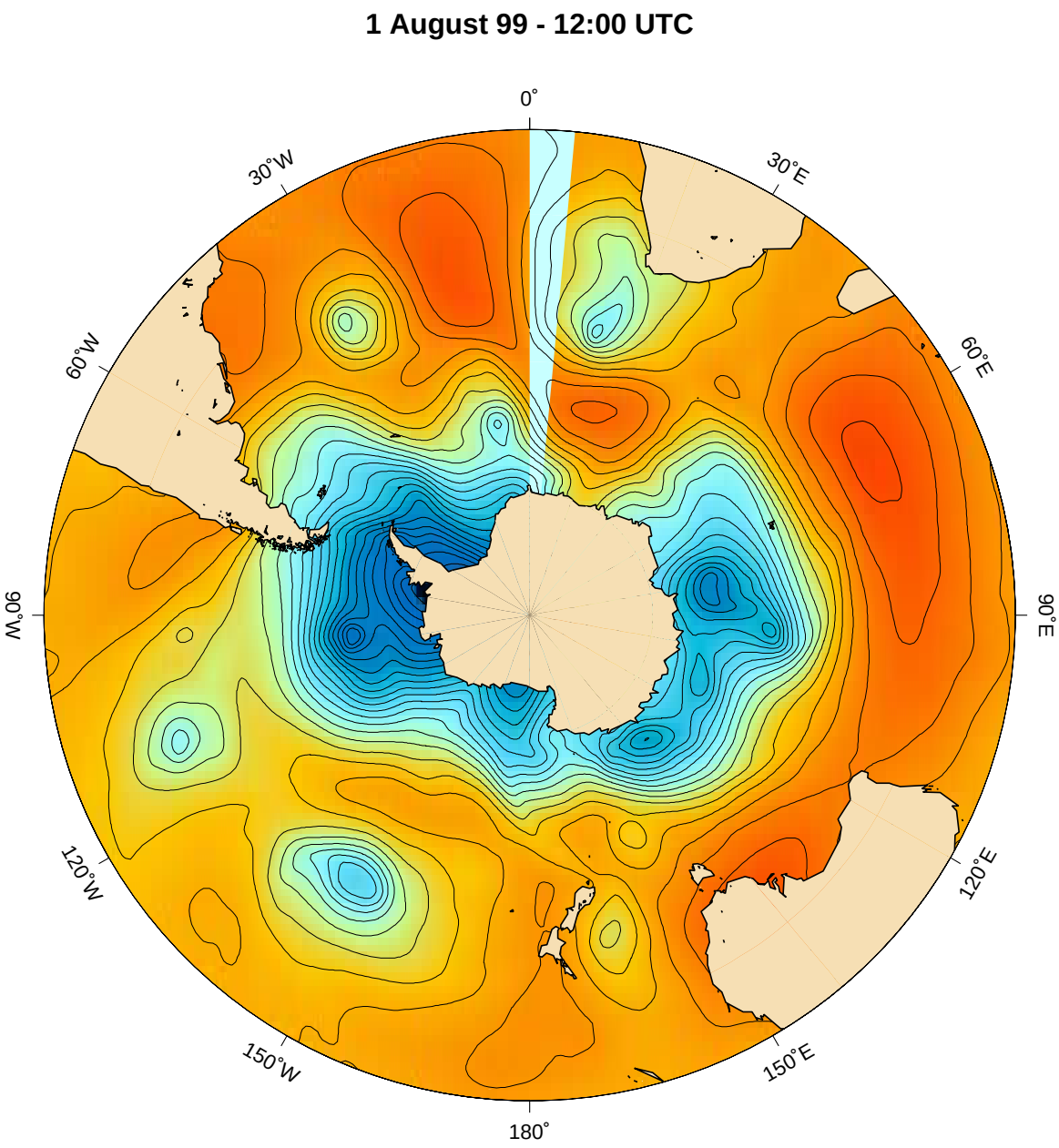

Figure 4.2: ECMWF surface pressure field corresponding to Fig. 4.1

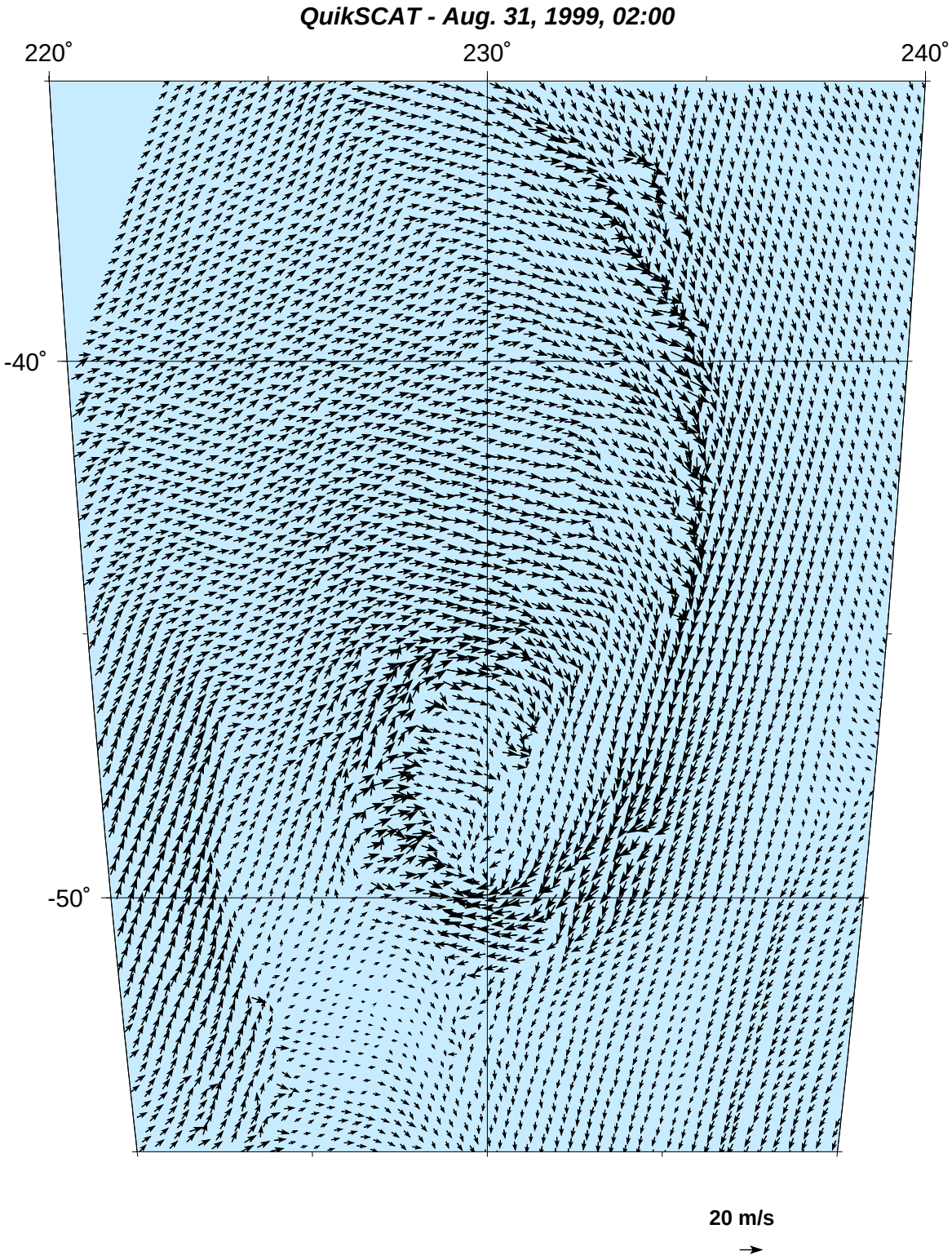

Figure 4.3: Mature cyclone over the Southern Pacific Ocean - August 31, 1999

the center of the low and on the southwestern flank of the cyclone, and the sharply defined cold front. There is no visible warm front. However, one could argue that secondary convergence lines are visible in the cold air sector. Similarly, the sharp transition in wind speed in the southwestern corner of the figure is peculiar.

This last example is not an exception and many dramatic storms were indeed observed over the Southern Ocean in the winter of 1999. Figure 4.4 is another such example where fewer wind vectors are plotted for clarity (panel a) and the divergence field is plotted in panel b. A double front is visible and three other lines of con-

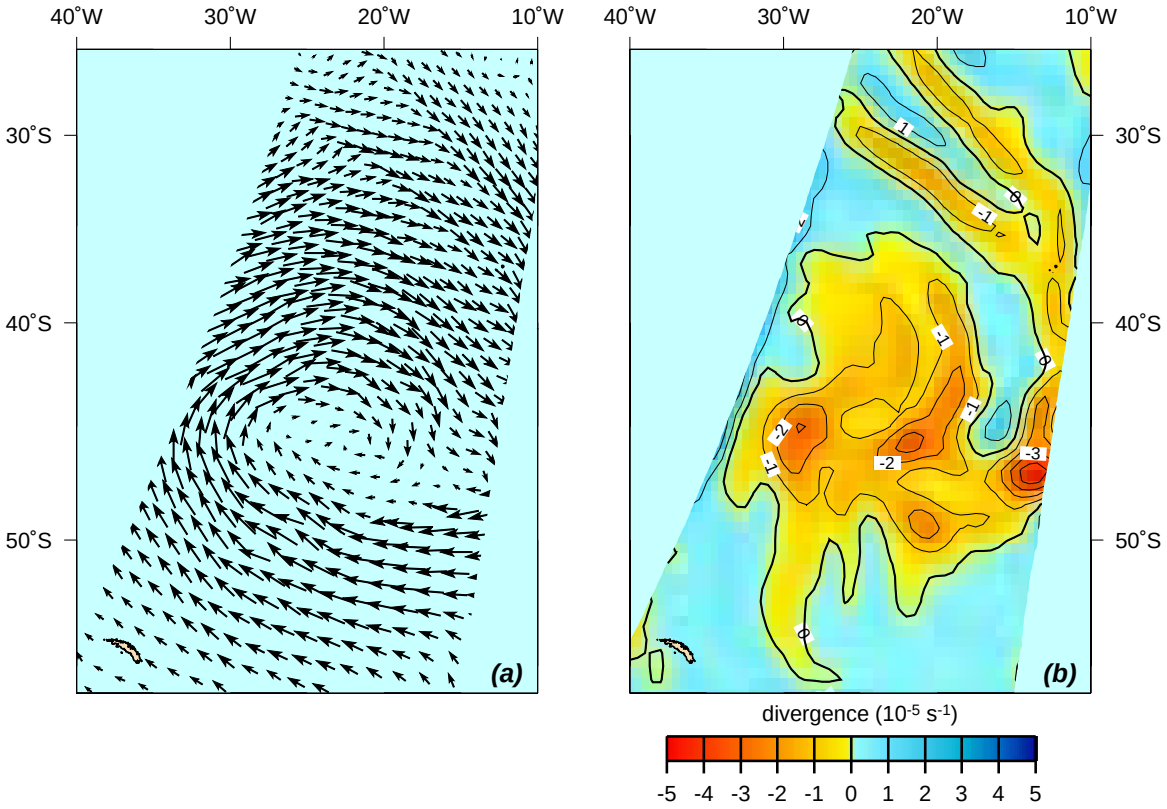

Figure 4.4: Mature cyclone over the Southern Pacific Ocean - September 20, 1999 (a) QuikSCAT surface wind field (b) Divergence field

vergence are extending from the low, one of which (the southernmost one) could be hypothesized to be the warm front, giving way to an occluded front wrapping around

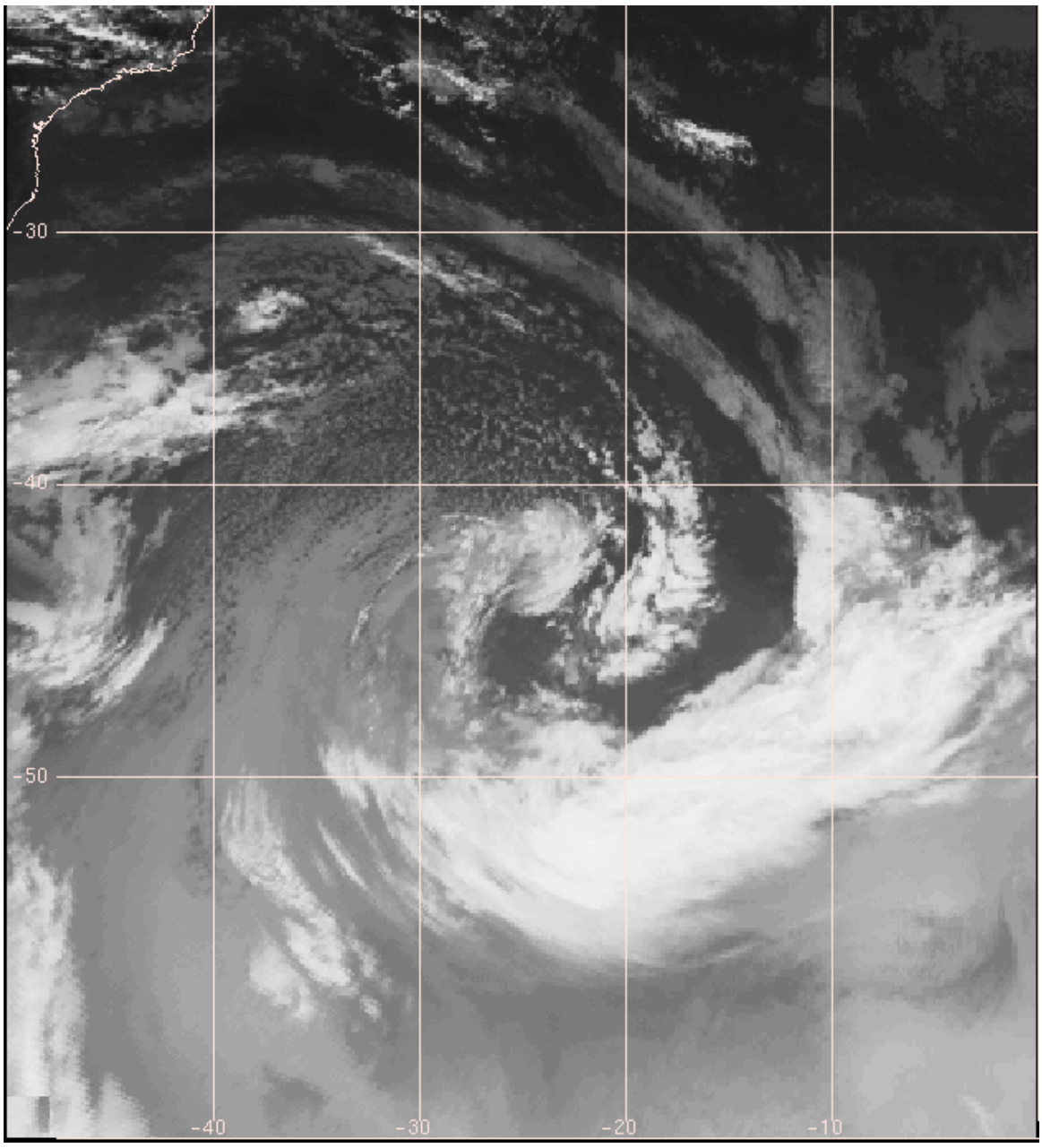

Figure 4.5: Same as 4.4 - Infrared image

the low (more data would be necessary to verify this).

Interestingly enough, these features have a counterpart in the corresponding infrared satellite image, as can be seen in Fig. 4.5 (less than ten minutes apart). Two bands of clouds are visible along the two convergence lines mentioned above. Moreover, a third cluster of clouds appears closer to the center, where another area of convergence was observed. This could correspond to enhanced convection and cloud formation in areas of convergence and then implies that the features visible in the filtered QuikSCAT surface wind fields are real and not a mere artifact.

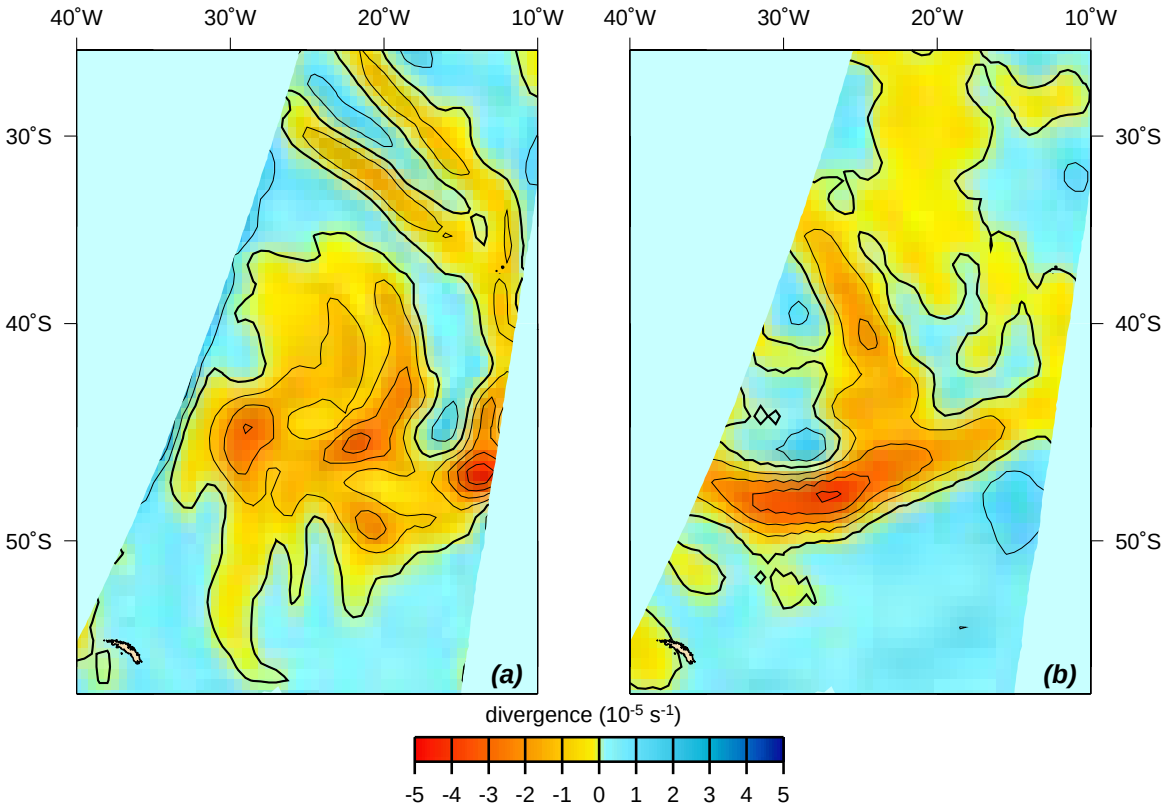

Figure 4.6: Same as figure 4.4b (a) from QuikSCAT (b) from NCEP (18:00 UTC)

For reference, the divergence fields obtained from QuikSCAT and from NCEP surface wind fields respectively are shown in Fig. 4.6. NCEP clearly indicates the presence of an occluded system, but with far less detail than the analysis made from

QuikSCAT data.

Reed and Albright (1997) note that the frontal structure in an extratropical cyclone can present a lot a variety, including different types of occluded fronts, from some fronts terminating ahead of the low center to fronts wrapping around the low more than one time. Many analyses are based on satellite imagery interpretation. Few studies have evidenced similar structures in measured surface wind fields. These structures are now visible in great detail in the QS wind fields. Future studies will involve documenting these different frontal structures, in particular dramatic examples of "T-bone" structures visible over the Southern Ocean (see next section).

The repeated observations of "dramatic" fronts led to the idea of following their evolution using their signature in divergence or deformation. This provides both a global view of cyclogenesis, frontogenesis and frontal wave development and a detailed view of the inner structure of those fronts and cyclones at 25-km resolution.

4.5 A quasi-synoptic look at fronts

Quasi-synoptic plots such as Fig. 4.1 were constructed and animated for the period July 1999-June 2000. Surface pressure and various kinematic fields were plotted. Figure 4.7 shows an example of surface divergence and pressure in July. One notes the presence of four major cyclonic systems separated by four high pressure ridges (actually an anticyclone at 160°W). The subtropical region is marked by the presence of four anticyclones. The presence of fronts can be inferred from the sharp change in curvature in the isobars and the lines of convergence in the upper plot. A striking example appears at 90°E where the observed T-bone structure is reminiscent of Shapiro and Keyser (1990)'s "bent-back" warm front. The decrease in convergence observed at the triple point is also reminiscent of their "frontal fracture".

Numerous other fronts are revealed in connection with the other systems. The 110°W cyclone is at the mature stage, its original cold front has moved ahead and

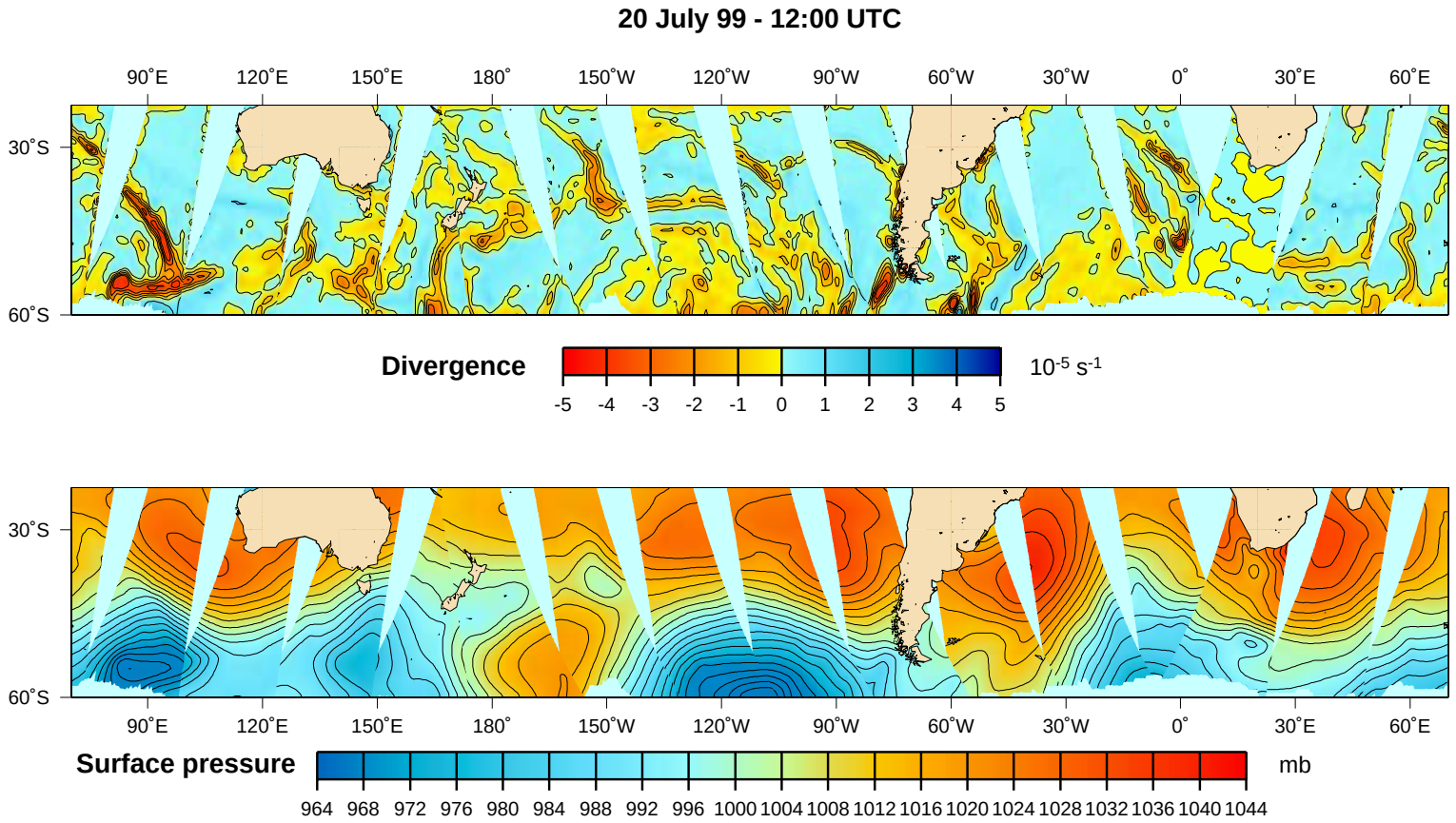

Figure 4.7: Quasi-synoptic view of the Southern Ocean obtained by running the pressure retrieval model on seven consecutive QuikSCAT swaths (a) Divergence (b) Surface pressure

is now hugging the coast of Chile. Other lines of convergence are present in the post-frontal sector (one between 90 and 100°W and another one reaching back to the shallow depression at 150°W). This shallow depression is itself associated with a front extending northward from the low. The 10°W cyclone contains at least two convergence lines. Similar lines of moderately strong convergence are observed in association with the 150°W storm. Note finally that a front is developing at 60°E in the lee of the first cyclone described above.

The pressure and divergence fields are next compared to the corresponding satellite imagery. The 12:15 UTC infrared composite image is shown in Fig. 4.8, where the divergence field from Fig. 4.7 has been reproduced for comparison. It can be easily verified that each of the features described above in the pressure and divergence fields has a counterpart in the cloud pattern. Note, in particular, the sharp frontal bands along the convergence lines classified as cold fronts (90°E, along the coast of Chile and the double-line at 10°W and 0°). These features also have counterparts in the vorticity and deformation plots (not shown here).

4.6 A front story

The animation of quasi-synoptic pictures of surface divergence and pressure over the Southern Ocean suggests an intricate relationship between the birth, maturation and decay of storms and that of fronts. As noted by Reeder and Smith (1998), fronts and storms generally move eastward but fronts sometimes have an equatorward component, while the parent cyclone sometimes moves southeastward. Some fronts reach far to the north, sometimes into the tropical regions. Other fronts maintain their surface characteristics (i.e. strong convergence and vorticity along with a signature in the surface isobars) for several days as they travel eastward, after the parent cyclone has reached maturation.

The sequence extracted from the July 1999-June 2000 period and used hereafter

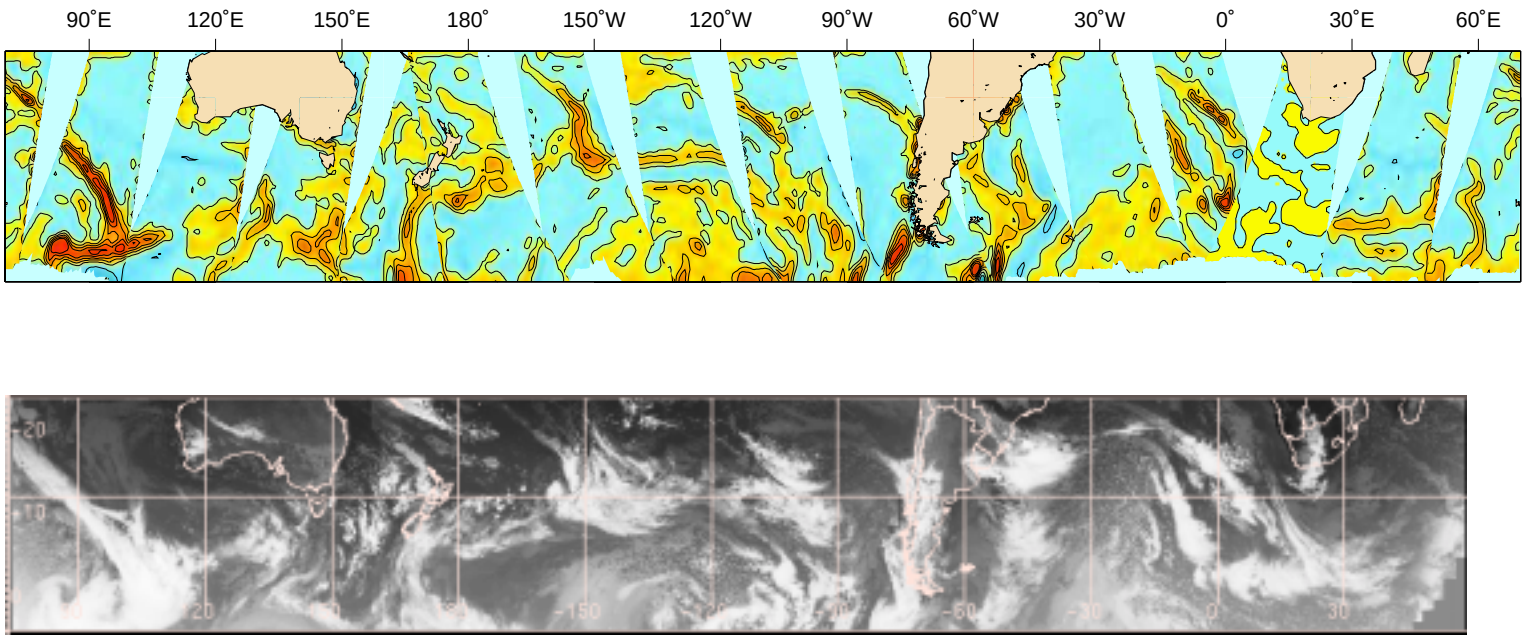

Figure 4.8: Divergence field and infrared composite image on July 20, 1999 at 12:15 UTC

to illustrate the evolution and interconnection of fronts and frontal cyclones is shown in Fig. 4.9 in 25 steps labeled (a) to (y). The 25 figures are separated each by roughly 12 hours, starting on July 20, 1999 at 12:00 UTC.

In panel (a), a major trough can be seen in the bottom part of the figure, with low pressure and cyclonic vorticity. A smaller perturbation appears in the northwestern sector, associated with a frontal structure extending north and appearing as a line of curvature change in the surface isobars. In the next panels, the perturbation merges with the trough as the ridge at 160° strengthens into an elongated anticyclone. The perturbation has a strong signature in convergence. In panel (f), the two entities have merged and the remaining cold front appears as an extension of the low pressure system. From panel (g) to (j), however, a small wave appears *along the cold front* and exhibits a clear comma-type signature in the divergence field.

In panel (k), the trailing cold front can be seen extending back to 110°W and 30°S. In the following steps, whereas the trough is moving eastward and over the tip of South America, a small cyclone develops very quickly and reaches its mature stage in about 24 hours. Note the clear comma-type signature in the divergence field in panel (o). The comma-structure can also be inferred from panels (p) and (q). Note that there does not appear to be a warm front.

In panels (r) and (s), the low merges with the polar trough and panel (t) shows the resulting structure exhibiting a strong North-South convergence line after it has passed over South America. Note also the weak pressure gradients on the western side of the convergence line, east of South America, and the very strong pressure gradients on the eastern side. Panel (u) re-emphasizes the meridional character of the resulting structure. The ridge seems to be "squeezed" between the two lows. The isobars are "packed" and reveal a very strong northerly flow from Brazil and south to Antarctica. The wind turning through the front is extremely sharp. This is also exchanging very cold air from the pole and warm and moist air from the Tropics on a very short longitudinal band. The front is more than 3000 km in extent, not a rare

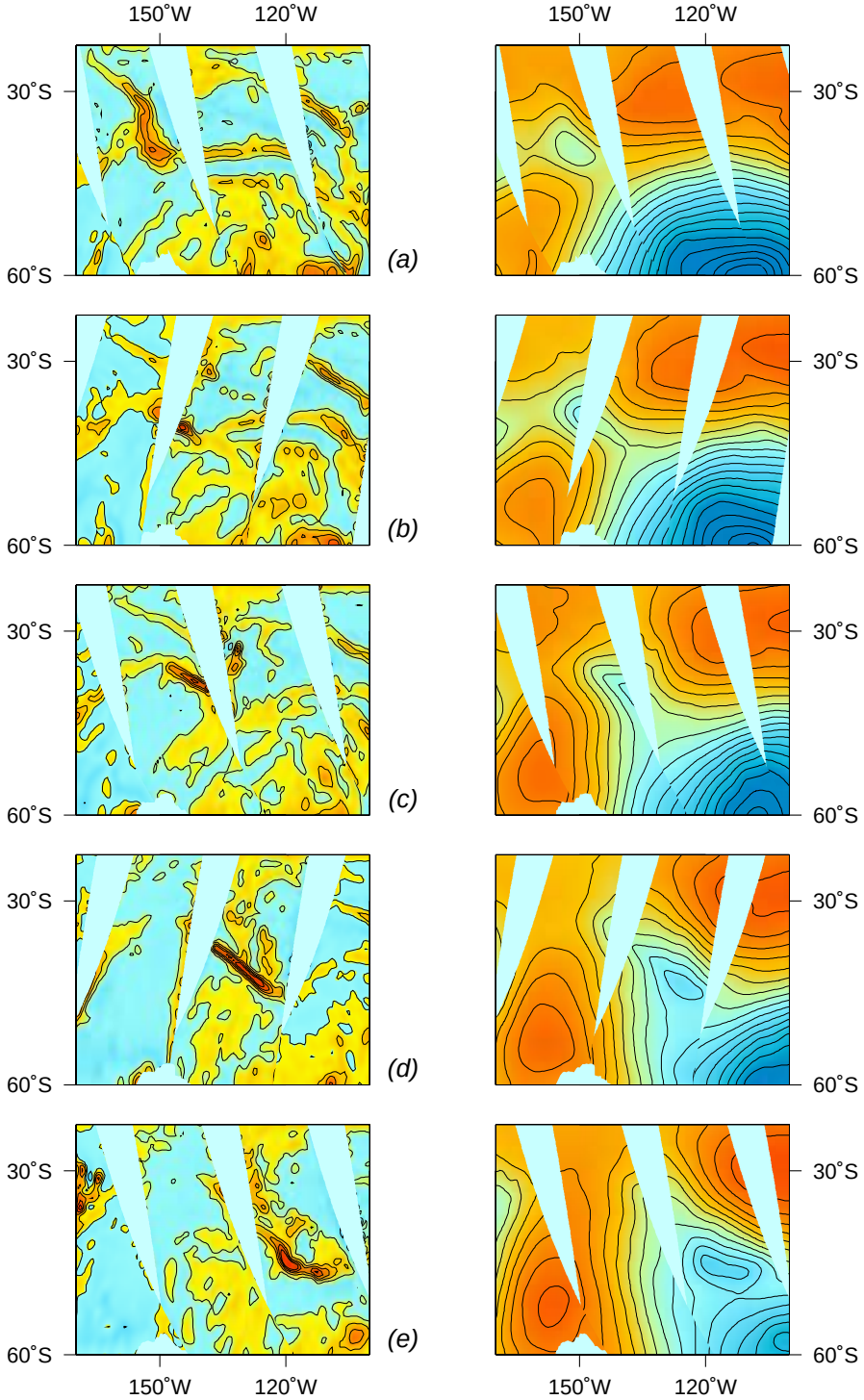

Figure 4.9: Evolution of a perturbation in the Southern Pacific - Left: divergence - Right: surface pressure (same scales as figure 4.7)

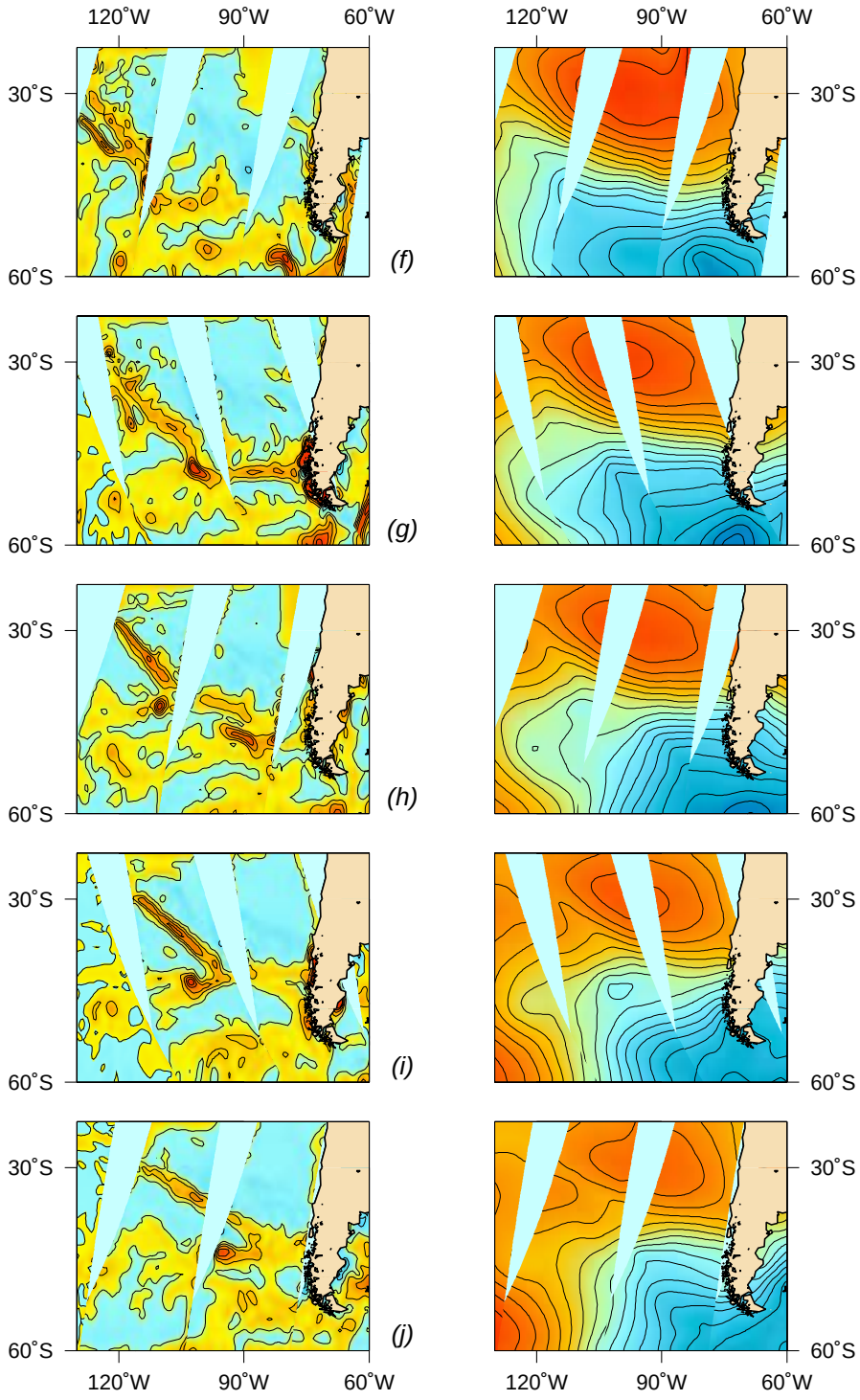

Figure 4.9: (Con't)

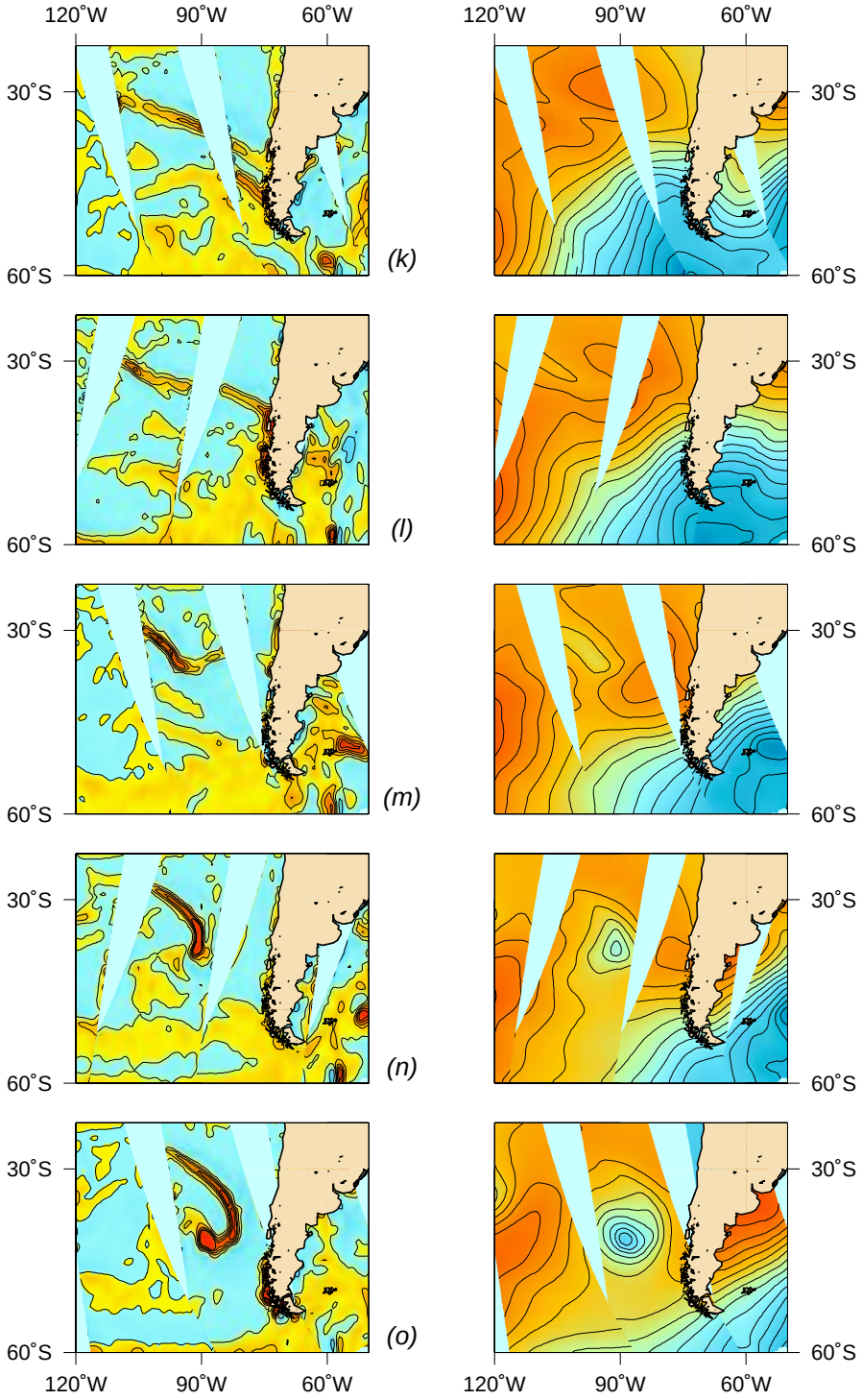

Figure 4.9: (Con't)

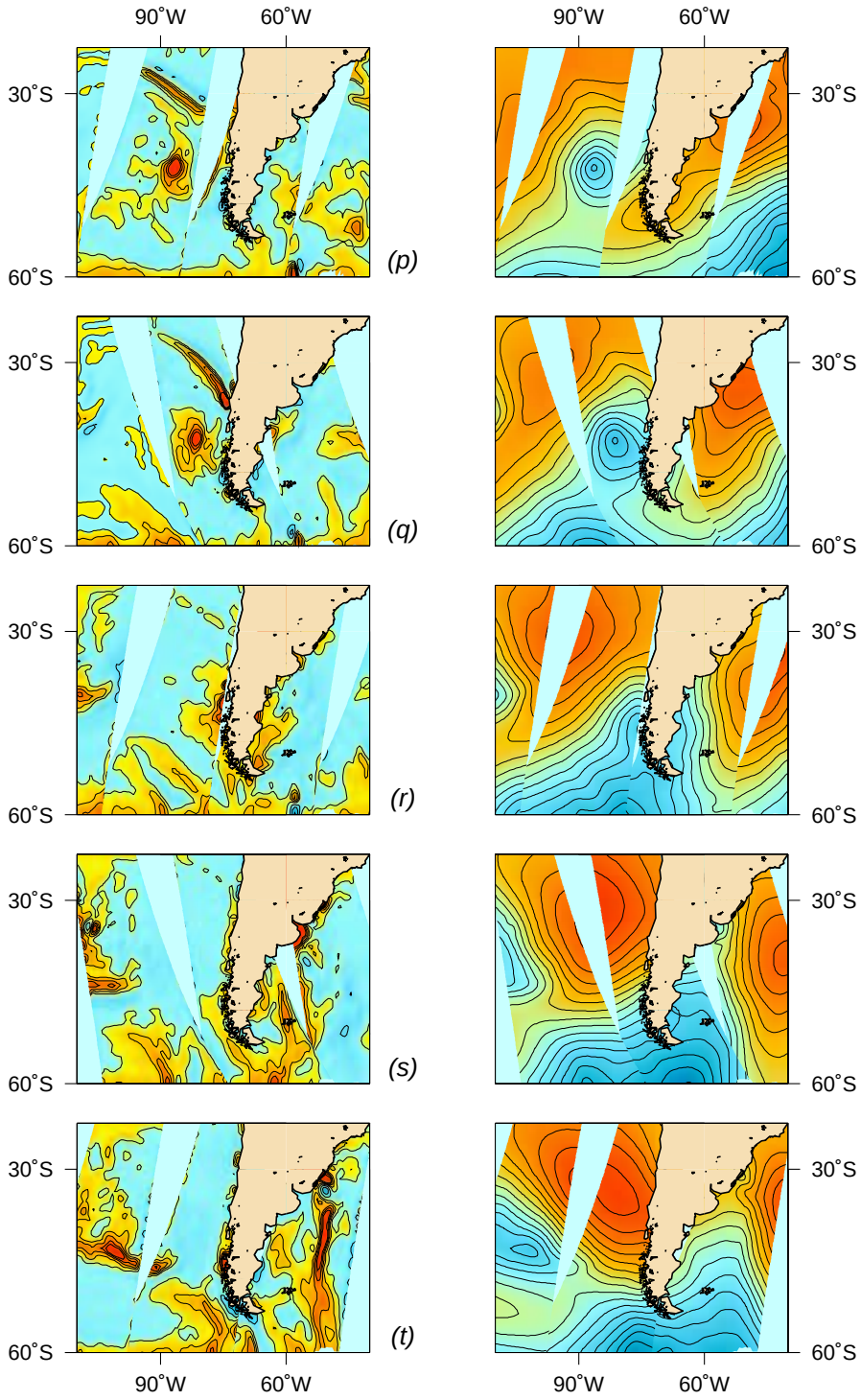

Figure 4.9: (Con't)

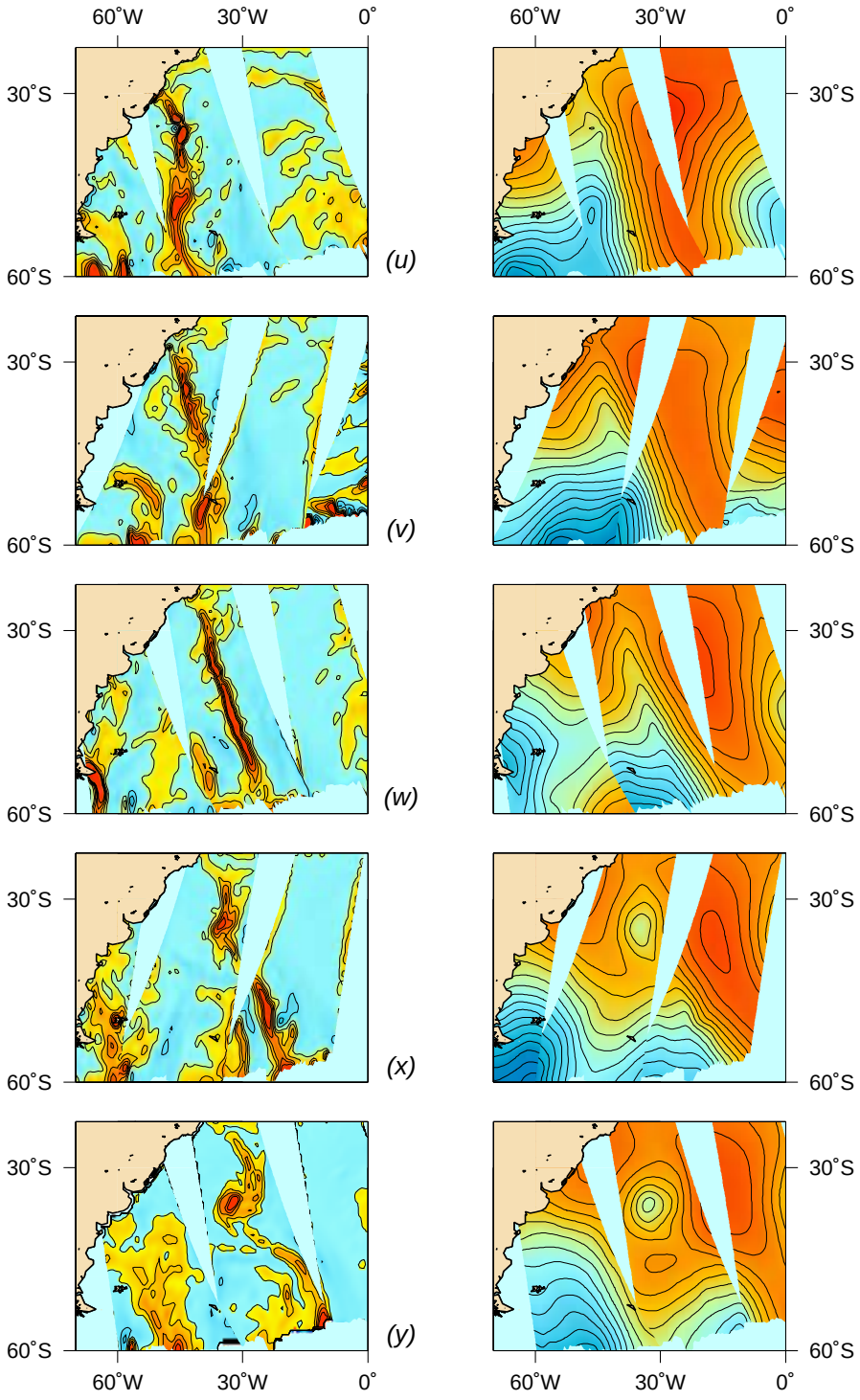

Figure 4.9: (Con't)

observation in the animation. It is also being sustained in its North-South alignment and with a fairly strong intensity for more than 60 hours.

In panel (x), a small pocket of vorticity appears *on the front* and develops into a new vortex that eventually follows the typical cyclone development (not shown). Since the vortex develops more than 60 hours after the front has passed over the mountain range, vortex stretching in the lee of the Andes probably plays a minor role in intensifying the vorticity in the region where the vortex is observed.

This type of frontal wave development is a recurrent feature of frontal evolution and many other examples can be found in the period of analysis (July 1999-June 2000). However, visual inspection of the QS-derived pressure fields and kinematic fields also reveals the presence of numerous frontal "lows" that do not deepen significantly (less than 5 mb). The reasons why some frontal waves deepen explosively while others are not developmental are not clearly understood (Parker, 1998).

The next chapter will describe the attribution technique used to partition the wind field and diagnose the respective roles played by the environmental flow and the front itself on the development of the frontal wave. The analysis is two-dimensional and limited to the lower boundary of the atmosphere. Although an atmospheric front is a three-dimensional structure, the frontal dynamics are often most intense near the surface (Orlanski and Ross, 1984) and the analysis reveals some interesting characteristics of three marine surface fronts. Reasons will be proposed as for why some fronts produce secondary cyclones whereas others do not.

Chapter 5

SCATTEROMETER-BASED FRONTAL WAVE ANALYSIS

5.1 Attribution technique with Green's functions

As mentioned earlier, frontal waves arise from a mesoscale instability on the trailing cold front of a mature system. Since they are of intermediate scale and embedded in a larger synoptic system, it is of interest to "separate" the frontal wave from its environment and to study the influence of the latter on the development of the former. Such a partitioning of the wind field has been the basis of several theoretical studies of frontogenesis (see section 2.1). The approach used by Bishop (1996a) consists in identifying the front with a strip of vorticity and convergence and reconstructing the corresponding nondivergent and irrotational wind fields. By subtraction from the total wind, the environmental flow can be calculated.

By applying classical "potential theory", the vorticity ζ and the divergence D characterizing the front can be associated with a streamfunction ψ and a velocity potential χ respectively (e.g. Acheson, 1990). We then have, in a general sense:

$$\nabla^2 \psi = \zeta \tag{5.1a}$$

$$\nabla^2 \chi = D \tag{5.1b}$$

and, to the extent that ψ and χ can be calculated, the corresponding wind components:

$$\boldsymbol{u}_\psi = -\boldsymbol{\nabla} \times \psi \boldsymbol{k} \tag{5.2a}$$

$$\boldsymbol{u}_\chi = \boldsymbol{\nabla}_h \chi \tag{5.2b}$$

These two wind fields can be thought of as the non-divergent and the irrotational components of the total wind field. By subtraction, the remaining component $\boldsymbol{u}_\theta = \boldsymbol{u} - \boldsymbol{u}_\psi - \boldsymbol{u}_\chi$ is irrotational and non-divergent, and represents the "background" wind, or "environmental" wind. It is generally modeled as a pure deformation wind field. Bishop's attribution technique provides a convenient way of estimating $\boldsymbol{u}_\theta$ and is adapted here to QuikSCAT data to study the impact of the environmental flow on the development of frontal waves over the Southern Ocean. The method will first be described and an example given.

5.1.1 Mathematical background

Green's functions

When solving a partial differential equation (PDE) system such as:

$$L[\phi] = f(\boldsymbol{x}) \qquad in\ \Omega \tag{5.3}$$

where $L[\quad]$ is a linear, second-order PDE operator, ϕ and f are both functions of $\boldsymbol{x}$ and suitable boundary conditions are specified, it is useful to look for solutions of the form:

$$\phi(\boldsymbol{x}) = \int_\Omega G(\boldsymbol{x}, \boldsymbol{\xi}) f(\boldsymbol{\xi}) d\boldsymbol{\xi} \tag{5.4}$$

where $G(\boldsymbol{x}, \boldsymbol{\xi})$ is referred to as the "Green's function" for $L[\quad]$. If such a function exists, then it is the solution of:

$$L[G] = \delta(\boldsymbol{x} - \boldsymbol{\xi}) \tag{5.5}$$

i.e. the original PDE system where the forcing is replaced by a Dirac delta-function. A solution to 5.5 is called a singularity solution for $L[\quad]$ to reflect the fact that the solution has a singular behavior at $\boldsymbol{\xi}$ (the infinite "spike"). Conversely, if equation

5.5 can be solved and the singularity solution (i.e. the Green's function) can be determined, then by multiplying both sides of 5.5 by $f(\boldsymbol{\xi})$ and integrating on $\boldsymbol{\xi}$:

$$\int_\Omega L[G]f(\boldsymbol{\xi})d\boldsymbol{\xi} = \int_\Omega \delta(\boldsymbol{x}-\boldsymbol{\xi})f(\boldsymbol{\xi})d\boldsymbol{\xi} \tag{5.6}$$

By definition of the Dirac function, the right-hand side of the above equation is equal to $f(\boldsymbol{x})$ and because $L[\quad]$ is a linear operator:

$$L\left[\int_\Omega G(\boldsymbol{x},\boldsymbol{\xi})f(\boldsymbol{\xi})d\boldsymbol{\xi}\right] = f(\boldsymbol{x}) \tag{5.7}$$

which is our original PDE. In the process, the solution $\phi(\boldsymbol{x})$ has been determined by superposition of the singular solutions modulated by the forcing field.

Singular solution for the Laplacian

In our particular case, $L[\quad]$ is the Laplacian operator:

$$\nabla^2(\psi) = \zeta(\boldsymbol{x}) \qquad in\ \mathbb{R}^2 \tag{5.8a}$$

$$\nabla^2(\chi) = D(\boldsymbol{x}) \qquad in\ \mathbb{R}^2 \tag{5.8b}$$

for which the Green's function can be shown to be:

$$G(\boldsymbol{x},\boldsymbol{\xi}) = \frac{1}{2\pi} log|\boldsymbol{x}-\boldsymbol{\xi}| \tag{5.9}$$

(see Appendix B). The streamfunction ψ and velocity potential χ are thus obtained by superposition:

$$\psi(\boldsymbol{x}) = \frac{1}{2\pi}\int_{\mathbb{R}^2} \zeta(\boldsymbol{\xi}) log|\boldsymbol{x}-\boldsymbol{\xi}|d\boldsymbol{\xi} \tag{5.10a}$$

$$\chi(\boldsymbol{x}) = \frac{1}{2\pi}\int_{\mathbb{R}^2} D(\boldsymbol{\xi}) log|\boldsymbol{x}-\boldsymbol{\xi}|d\boldsymbol{\xi} \tag{5.10b}$$

An important advantage of a solution using Green's functions (as opposed to, for example, a solution obtained by overrelaxation) becomes apparent in the above formulation: the Green's function is not dependent on boundary conditions on the edges

of a finite region and the solution is obtained by integration over the whole domain (or, stated slightly differently, the boundary conditions are removed to infinity). For that reason, the singularity solutions are often called *free-space Green's functions*. Here the globe is mapped onto a plane using a conformal projection (see section 5.1.3). Thus the domain of integration is the infinite plane.

Because we aim at studying the front separately from its environment, it is of interest here to attribute a streamfunction and a velocity potential to the elements of vorticity and divergence contained in a subdomain Ω of the infinite plane (i.e. a box surrounding a frontal region). In that case, the solutions are:

$$\psi_\Omega(\boldsymbol{x}) = \frac{1}{2\pi} \int_{\zeta \in \Omega} \zeta(\boldsymbol{\xi}) log|\boldsymbol{x} - \boldsymbol{\xi}| d\boldsymbol{\xi} \tag{5.11a}$$

$$\chi_\Omega(\boldsymbol{x}) = \frac{1}{2\pi} \int_{D \in \Omega} D(\boldsymbol{\xi}) log|\boldsymbol{x} - \boldsymbol{\xi}| d\boldsymbol{\xi} \tag{5.11b}$$

and the nondivergent and irrotational parts of the wind field attributable to the elements of vorticity and divergence contained in the subdomain Ω are defined as:

$$\boldsymbol{u}_\psi = -\boldsymbol{\nabla} \times (\psi_\Omega \boldsymbol{k}) \tag{5.12a}$$

$$\boldsymbol{u}_\chi = \boldsymbol{\nabla}_h \chi_\Omega \tag{5.12b}$$

If we write the total wind $\boldsymbol{u}$ as a sum of three components:

$$\boldsymbol{u} = \boldsymbol{u}_{\psi\Omega} + \boldsymbol{u}_{\chi\Omega} + \boldsymbol{u}_{\theta\Omega} \tag{5.13}$$

then $\boldsymbol{u}_{\theta\Omega}$ is the part of the wind field that is not attributable to elements of vorticity or divergence contained in Ω. It is therefore usually referred to as the harmonic part of the wind, and is attributable to elements of vorticity and divergence outside of Ω. It is also referred to as the environmental flow. This wind partitioning is thus an ideal way of separating the wind components on two different scales: local contributions at

the frontal scale ($\boldsymbol{u}_{\psi\Omega}$ and $\boldsymbol{u}_{\chi\Omega}$) and contributions from surrounding systems at the synoptic scale ($\boldsymbol{u}_{\theta\Omega}$).

Note that $\boldsymbol{u}_{\theta\Omega}$ might also contain a global harmonic component that is not attributable to any element of vorticity or divergence inside or outside Ω (i.e. a global background harmonic wind field). However, if such a component $\boldsymbol{u}_{\theta\Omega'}$ exists and we further decompose $\boldsymbol{u}_{\theta\Omega}$ into $\boldsymbol{u}_{\theta\Omega 0}$, due to elements of vorticity and divergence outside the domain, and $\boldsymbol{u}_{\theta\Omega'}$, then $\boldsymbol{u}_{\theta\Omega'}$, being irrotational, can be written as:

$$\boldsymbol{u}_{\theta\Omega'} = \nabla_h \theta \tag{5.14}$$

where θ is a velocity potential. Since the infinite plane is here really a mapping of the globe, θ must converge toward a constant at infinity (i.e. the point opposite the center of projection). Since θ is harmonic, it must then be constant everywhere, and $\boldsymbol{u}_{\theta\Omega'}$=0 (Bishop, 1996a). Consequently, $\boldsymbol{u}_{\theta\Omega}$ is attributable solely to elements of vorticity and divergence outside of the domain Ω.

Estimating $\boldsymbol{u}_{\theta\Omega}$ on a finite grid

Since Bishop (1996a) goes into great detail about adapting the reconstruction technique to discrete data, only a brief summary will be given here. The integrand of equation 5.10 can be viewed as the contribution at $\boldsymbol{x}$ of a vorticity or divergence element centered at $\boldsymbol{\xi}$. If we follow Bishop (1996a)'s notation and index of the grid boxes with $1 < k' < M-1$ (along the x-coordinate) and $1 < l' < N-1$ (along the y-coordinate), then $(x'_{k'l'}, y'_{k'l'})$ stand for the coordinates of the center of the $k'l'$ grid box (finite version of $\boldsymbol{\xi}$ above), $C_{k'l'}$ and $F_{k'l'}$ represent the circulation around and the flux out of the $k'l'$ grid box (ζ and D above), $r_{k'l'}$ is the distance between $\boldsymbol{x}$ and $\boldsymbol{\xi}$, and the non-divergent part of the wind field $\boldsymbol{u}_\psi$ becomes:

$$u_{\psi\Omega} = \frac{1}{2\pi} \sum_{1}^{M-1} \sum_{1}^{N-1} C_{k'l'} \frac{-(y - y'_{k'l'})}{r^2_{k'l'}} \tag{5.15a}$$

$$v_{\psi\Omega} = \frac{1}{2\pi} \sum_{1}^{M-1} \sum_{1}^{N-1} C_{k'l'} \frac{(x - x'_{k'l'})}{r^2_{k'l'}} \tag{5.15b}$$

whereas the irrotational part of the wind field $\boldsymbol{u}_\chi$ takes the form:

$$u_{\chi\Omega} = \frac{1}{2\pi} \sum_{1}^{M-1} \sum_{1}^{N-1} F_{k'l'} \frac{(x - x'_{k'l'})}{r^2_{k'l'}} \tag{5.16a}$$

$$v_{\chi\Omega} = \frac{1}{2\pi} \sum_{1}^{M-1} \sum_{1}^{N-1} F_{k'l'} \frac{(y - y'_{k'l'})}{r^2_{k'l'}} \tag{5.16b}$$

The environmental flow $\boldsymbol{u}_{\theta\Omega}$ is obtained by difference with equation 5.13.

5.1.2 Example

The attribution technique is now illustrated with an example over the Southern Ocean, West of Chile, on July 25, 1999 at 13:00 UTC (panel k of Fig. 4.9). Figure 5.1a shows a QS-derived pressure field where a trailing cold front is visible around 34°S. The corresponding mature system is merging with the polar trough South of the Drake Passage. The front is located between two anticyclones (95°W-30°S and 110°W-37°S) which make the (100°W-35°S) point a saddle point often referred to as a *col* point. The front is clearly visible in the divergence field shown in Fig. 5.1b. A box is drawn around the front, as shown in Fig. 5.1c where the figure has been rotated in such a way as to line the front up with the vertical axis of the page. This will define the x-axis (across the front, pointing toward the warm air) and the y-axis of the frontal box (along the front, pointing toward the tail). In the rest of this study, all the fronts will similarly be rotated to allow for comparison. Figure 5.1d is an enlargement of the frontal box showing both the line of convergence (background yellow and orange colors) and the QS winds. The box is 1000 km wide and 2000 km long.

The partitioning of the wind using the attribution technique described above is shown in Fig. 5.2, where $\boldsymbol{u}_\psi$,$\boldsymbol{u}_\chi$ and $\boldsymbol{u}_\theta$ are shown respectively. One can clearly

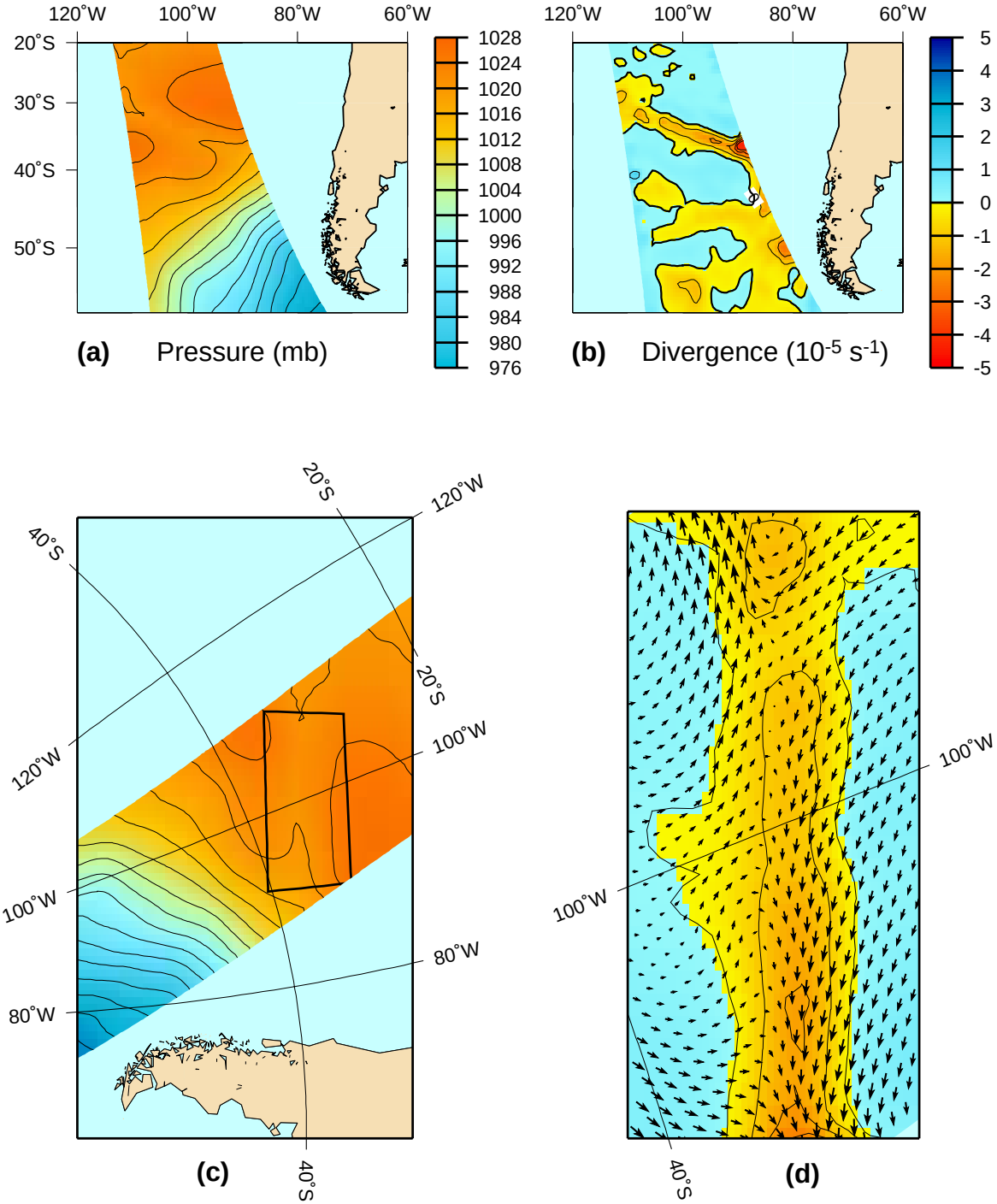

Figure 5.1: Different views of a front on July 25, 1999 at 13:00 UTC (a) QS-derived pressure field (b) QS-derived divergence (c) Same as in (a) after rotation, with frontal box shown around the front (d) QS divergence and winds in frontal box

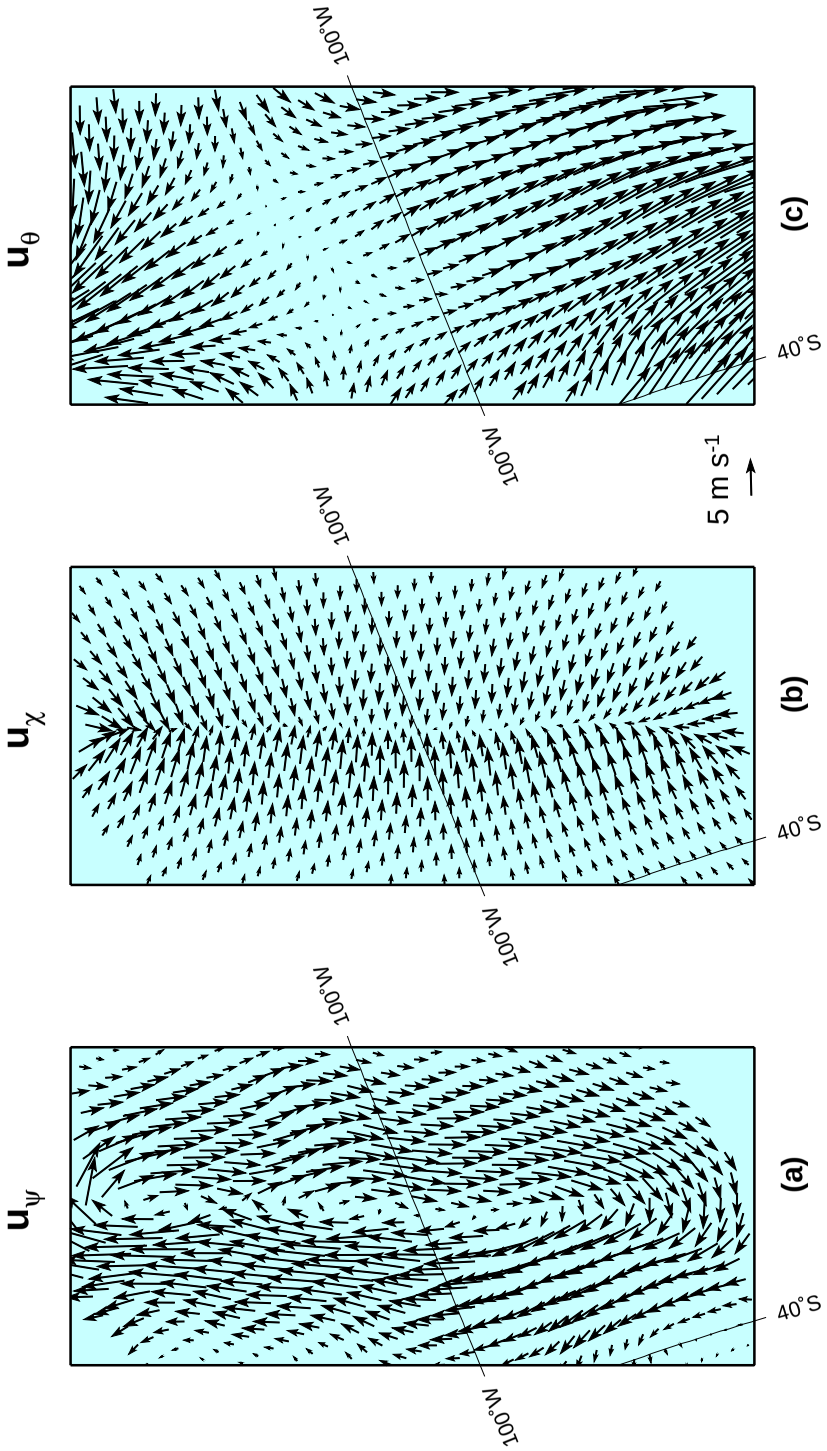

Figure 5.2: Partitioning of the QS winds shown in 5.1d - (a) $\boldsymbol{u}_\psi$ (b) $\boldsymbol{u}_\chi$ (c) $\boldsymbol{u}_\theta$

appreciate how $\boldsymbol{u}_\psi$ describes the *vortical* part of the flow and $\boldsymbol{u}_\chi$ describes the divergent (here mainly convergent) part of the flow. One also notes that the remaining environmental flow $\boldsymbol{u}_\theta$ is characterized by strong stretching deformation. One of the objectives of this study will be to determine how this stretching deformation affects the growth of frontal instabilities.

This attribution technique enables us to partition the wind in a way that is consistent with and comparable to the theoretical partitions proposed in section 2.1. The impact of the environmental flow calculated with this technique can be studied in much the same way as the impact of the deformation flow in theoretical models. Furthermore, a more dynamical meaning can be associated with the nondivergent and irrotational components of the wind. $\boldsymbol{u}_\psi$ clearly contains the vorticity characterizing the turning of the wind in the frontal zone. If we "lift" the nondivergent wind $\boldsymbol{u}_\psi$ and the background flow $\boldsymbol{u}_\theta$ (also nondivergent), we lift, in effect, the geostrophic component of the wind and the rotational part of the ageostrophic wind. What remains is the "divergent" component $\boldsymbol{u}_\chi$, which can be thought of as the divergent component of the ageostrophic wind. It is therefore of interest to understand how this ageostrophic (cross-frontal) wind contributes to the development of the frontal wave.

Note that the identification of the front with the line of maximum convergence is motivated by the application of the attribution technique. Positioning of the front following, for example, the dynamical conditions specified by Reed and Albright (1997) would lead to a slightly different location. Since the lateral shear of the along-front wind component should be more cyclonic on the cold side of the front (i.e. within the frontal zone) and the cyclonic curvature of the isobars should be stronger in the frontal zone than in the adjacent warm air, the cold front identified following these criteria would be drawn slightly northeastward of the center line of the box.

5.1.3 Projections and mapping

All the above calculations are carried in spherical coordinates, to ensure minimum distortion. Once the wind field is partitioned, the components are projected onto a flat plane using a polar stereographic projection:

$$x_p = \frac{2a\cos(\phi)\sin(\lambda)}{1-\sin\phi} \tag{5.17a}$$

$$y_p = \frac{2a\cos(\phi)\cos(\lambda)}{1-\sin\phi} \tag{5.17b}$$

where a is the mean radius of the earth, λ the longitude and ϕ the latitude. This allows for easy rotation of the box while still ensuring minimum distortion in the midlatitudes.

5.1.4 Sensitivity analysis

Bishop (1996b) discusses the advantages of this method over other techniques. Evaluating the stretching rate from the total wind along vorticity lines can lead to large errors because the waviness of the front will induce a wavy pattern in the calculated stretching rate. Similarly, evaluating the stretching rate from the mean stretching in the box can lead to significant errors due to the orientation of the box. The method used here ensures that the environmental flow is effectively calculated, by subtraction, from the vorticity and divergence elements surrounding the frontal box.

The error associated to the grid spacing in the calculation of the stretching rate can be evaluated by considering that the grid spacing induces an uncertainty of $\pm\tan^{-1}(\Delta x/L)$ on the angle of the front, where Δx is the length of one grid square and L the length of the frontal box (Bishop, 1996b). In the case described above, with a grid spacing of 50 km and a frontal box length of 1100 km, this amounts to an uncertainty of $\pm 2.6°$ on the orientation of the box. When repeating the above analysis after rotation of the box to these two extremes, the along-front stretching is observed to vary by less than 0.1%.

Bishop (1996b) also discussed the domain independence of the attribution technique to the size of the box and verified that u_ψ, u_χ and u_θ were domain-independent up to the precision of the calculation. A more detailed sensitivity study is provided by Renfrew et al. (1997) who varies the width of the box by $\pm 25\%$ and the angle by $\pm 3°$. He obtained a variation of only 0.06×10^{-5} s^{-1} in $\partial v_e / \partial y$ from real data, as opposed to 0.25×10^{-5} s^{-1} when using the total wind. Similar calculations were carried out on the example described above and a maximum variation of 0.06×10^{-5} s^{-1} was found. This is consistent with Renfrew et al. (1997) and can be understood by considering panel (d) of Fig. 5.1. Because the elements of vorticity and divergence are concentrated in a narrow strip along the central line of the frontal box, decreasing or increasing the size of the box will not affect significantly the number of vorticity and divergence elements taken into account in the attribution calculations. Similarly, by considering panel (c) of Fig. 5.2, one will see that rotating the frontal box by $\pm 3°$ amounts to rotating the environmental wind vectors by $\pm 3°$, which will not affect the estimate of along-front stretching in any significant way. This is, indeed, one of the main advantages of Bishop's method and one of the reasons for its popularity.

5.1.5 Characteristics of the environmental flow

The impact of the environmental flow u_θ on the development of the front is assessed by calculating the mean kinematic components of u_θ. This is illustrated in Fig. 5.3 for the same front as in the previous sections. Note that x, y, u and v now correspond to the frame of reference defined by the frontal box.

Panel (a) shows u_θ for reference. The along-front stretching component $\partial v / \partial y$ is shown in panel (b). It is furthermore averaged along lines parallel to the front and plotted as a function of x in the upper-part of panel (b). The along-front stretching is fairly homogeneous across the frontal box, with a mean of $0.6 \times 10^{-5} s^{-1}$.

Cross-frontal shear $\partial v / \partial x$ is plotted in panel (c) and averaged in the upper diagram. It is relatively homogeneous except for a region close to and along the front

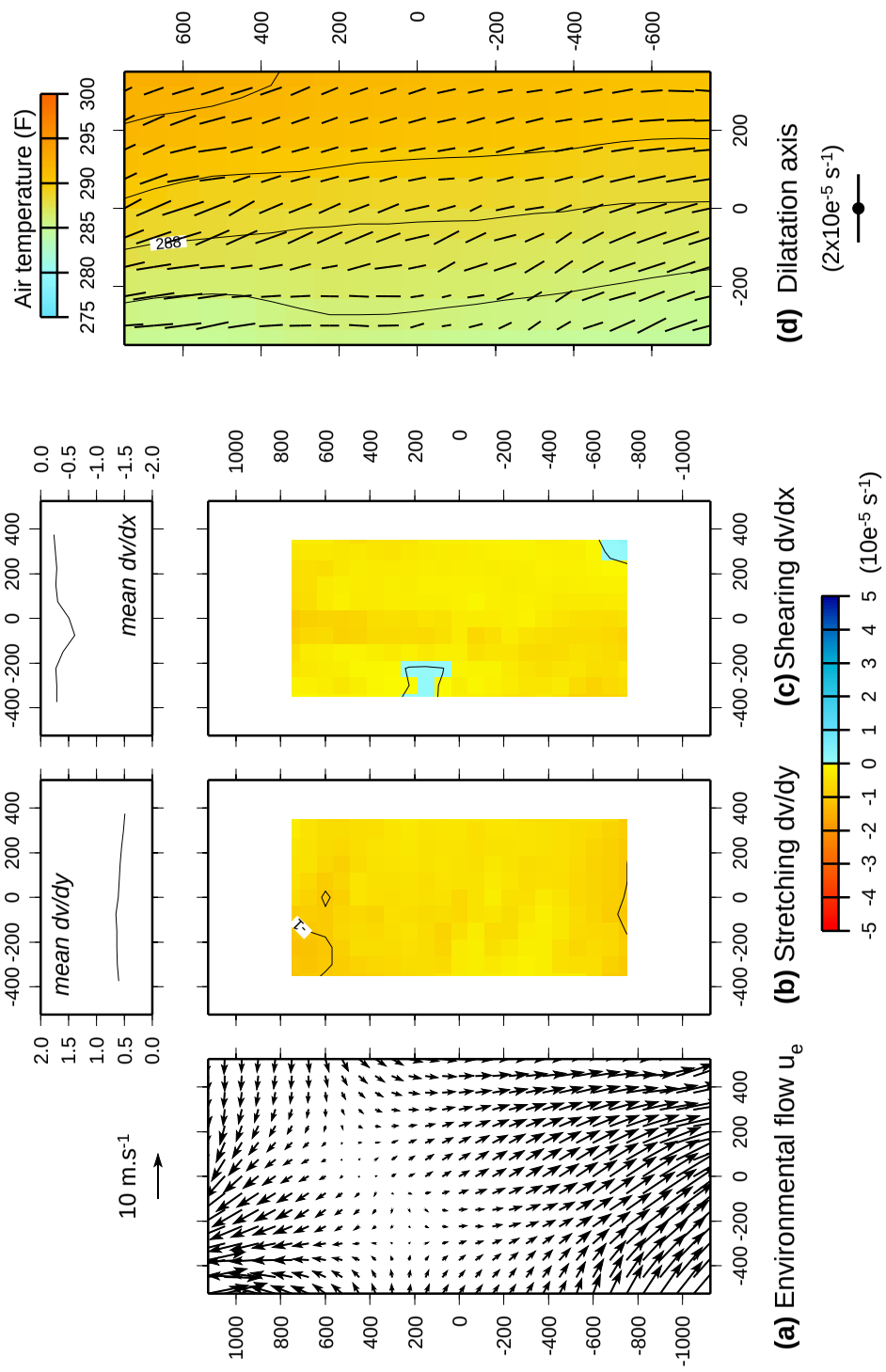

Figure 5.3: Kinematic analysis of the environmental flow

where the shear increases. This shows that the environmental flow contains a frontal characteristic that was not captured by the vorticity and the divergence contained in the frontal box.

The axis of dilatation of the environmental flow is plotted in panel (d) with surface air temperature (plain lines and colors). The axis of dilatation is on average at an angle with the isotherms which will, in this case, tend to rotate the front in an anticlockwise direction. It is competing with the vorticity of the front itself, which tends to rotate the front in a clockwise fashion.

A time series of averaged along-front stretching will be constructed from these kinematic values at different stages of the life cycle of a front in section 5.2.

5.1.6 Frontal wave growth

In order to evaluate how a frontal wave grows, an adequate measure of the growth is necessary. Several measures have been used in the past, including the amplification of the wave slope (Bishop and Thorpe, 1994) and the vorticity waviness (Renfrew et al., 1997). On a two-dimensional plane, the wave slope is measured as the angle between a line of vorticity and its basic-state position, which is difficult to extract from observations. The vorticity waviness W is defined as the peak vorticity ζ_{peak} in the frontal box minus the maximum along-front average vorticity $\bar{\zeta}^y$, where the latter is calculated on each line of points parallel to the front. Using Renfrew et al. (1997)'s notation, the waviness is then:

$$W(\zeta) = \zeta_{peak} - \max(\bar{\zeta}^y) \tag{5.18}$$

The peak vorticity ζ_{peak} characterizes the growing instability. But if the vorticity of the whole front also increases significantly, the instability cannot be said to grow as a separate entity. Subtracting the along-front average vorticity $\bar{\zeta}^y$ ensures that the vorticity waviness reflects how the instability is growing as compared to the rest of the front. The two quantities can be evaluated easily from observations and this second

method is therefore used in this study.

The derivative of the waviness, calculated by finite differences, can then be used as a proxy for growth. Since a QS look at an evolving front can be obtained roughly every 12 hours, an approximate time series of $W(\zeta)$ and its derivative can be obtained and explosive growth, if it occurs, can be detected. Applications will be shown in the next section.

5.1.7 Frontogenesis

As suggested by recent analyses (e.g. Rivals et al., 1998), characterizing the frontogenetical or frontolytical impact of the different wind components might be crucial in understanding the timing and location of frontal wave growth. It is therefore of interest to evaluate these impacts from the calculated winds.

Frontogenesis can be defined as the rate of change of the magnitude of the horizontal potential temperature gradient following parcel trajectories (Petterssen, 1936):

$$\frac{d}{dt}|\nabla\theta| = -\frac{1}{2}|\nabla\theta|(D - E\cos 2\beta) \tag{5.19}$$

In Cartesian coordinates, the expression derived by Keyser et al. (1988) is preferred:

$$F_x = \frac{d}{dt}\left(\frac{\partial\theta}{\partial x}\right) = -\frac{\partial u}{\partial x}\frac{\partial\theta}{\partial x} - \frac{\partial v}{\partial x}\frac{\partial\theta}{\partial y} \tag{5.20a}$$

$$F_y = \frac{d}{dt}\left(\frac{\partial\theta}{\partial y}\right) = -\frac{\partial u}{\partial y}\frac{\partial\theta}{\partial x} - \frac{\partial v}{\partial y}\frac{\partial\theta}{\partial y} \tag{5.20b}$$

In turn, if we use the above wind partitioning (Eq. 5.13), we can also partition the frontogenesis vector $\boldsymbol{F_0}$ into its three components, respectively frontogenesis due to $\boldsymbol{u_\psi}$, $\boldsymbol{u_\chi}$ and $\boldsymbol{u_\theta}$:

$$\boldsymbol{F_0} = \boldsymbol{F_\psi} + \boldsymbol{F_\chi} + \boldsymbol{F_\theta} \tag{5.21}$$

Note that $\boldsymbol{F_\chi}$ corresponds to frontogenesis due to the ageostrophic (cross-frontal) wind, of particular interest in understanding the role played by cross-frontal convergence in the development of frontal waves.

ECMWF surface air temperatures are interpolated onto the frontal box grid and frontogenesis is calculated by finite differences using the above equation. Note that there is a resolution difference between the frontal box grid (50 km) and ECMWF ($1.25° \times 1.12°$). The fronts are not as "sharp" in the ECMWF surface air temperature fields as in the QS-derived pressure fields. Moreover, the QS passes are close to synoptic time at the beginning of the following analysis (within one hour) but not at the end. There is therefore some uncertainty in the collocation of the temperature front and wind-derived front. For lack of better data, the temperature and wind fields were only inspected for visual consistency.

Because frontogenesis is of interest only in the vicinity of the frontal region, F_x is averaged on a smaller box within the frontal box of 300×1000 km. Time series of the three components are constructed at each stage of the front life cycle.

5.2 Life cycle of a front

In this chapter, the methodology described above is applied to the front described in section 4.6. The front experiences two successive frontal wave developments over the Southern Pacific and Southern Atlantic Ocean. Its life cycle is summarized in Fig. 5.4 in 15 steps lettered (a) through (o). In each panel, the pressure and divergence fields are shown with the frontal box drawn around the front. The bottom part of each panel shows the environmental flow in the box. The frontal boxes have been rotated for comparison. The x-axis is always pointing toward the warm air (i.e. roughly northeastward or eastward). The y-axis is pointing toward the tail of the front (i.e. roughly northwestward or northward).

The first feature of interest appearing in steps (a)-(e) is the strong deformation signature of the environmental flow, which seems to validate the representation of the background flow by a deformation field in past theoretical studies. As explained in the previous section, the environmental flow in the frontal box is induced by vorticity

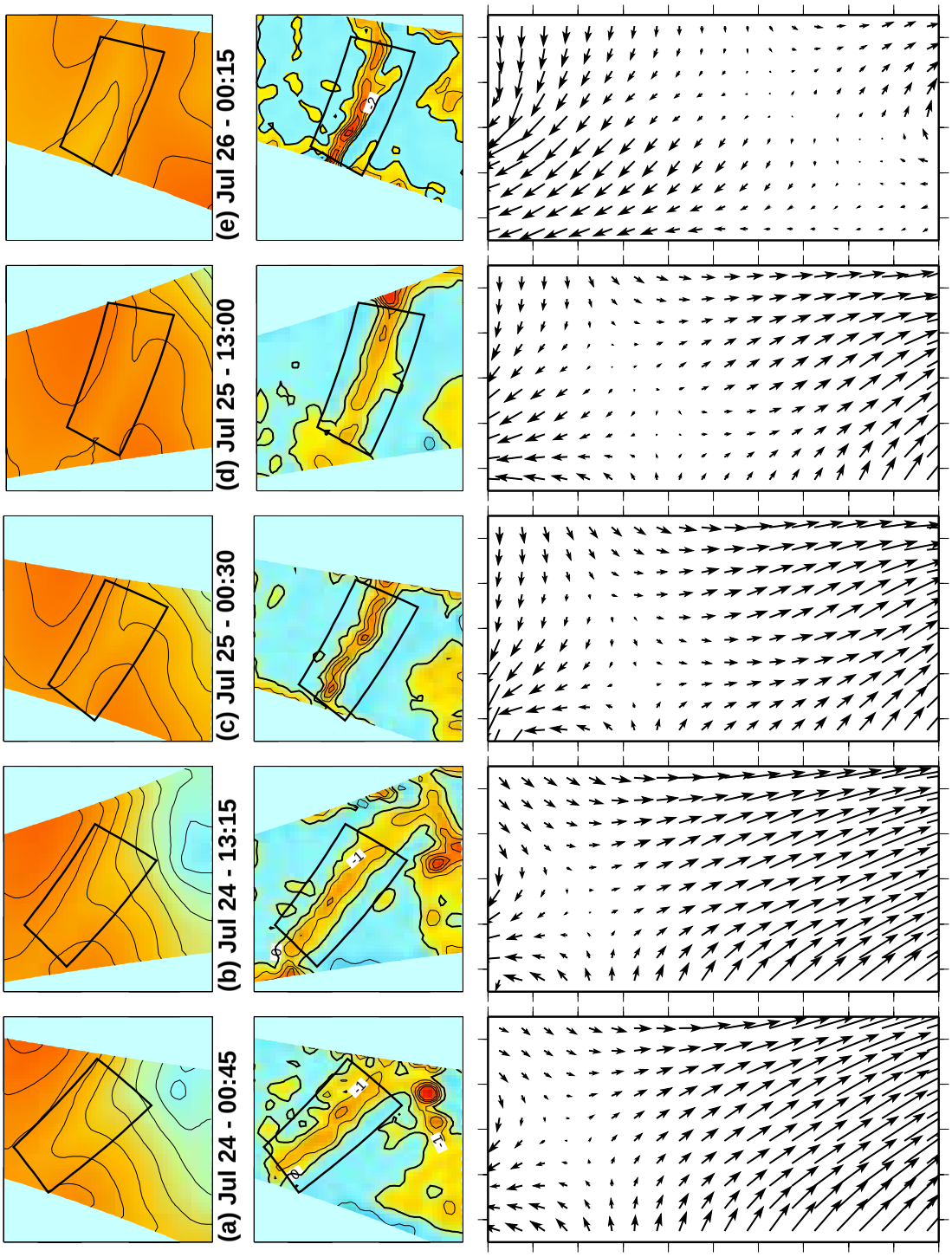

Figure 5.4: Evolution of the environmental flow during the development of two successive frontal waves

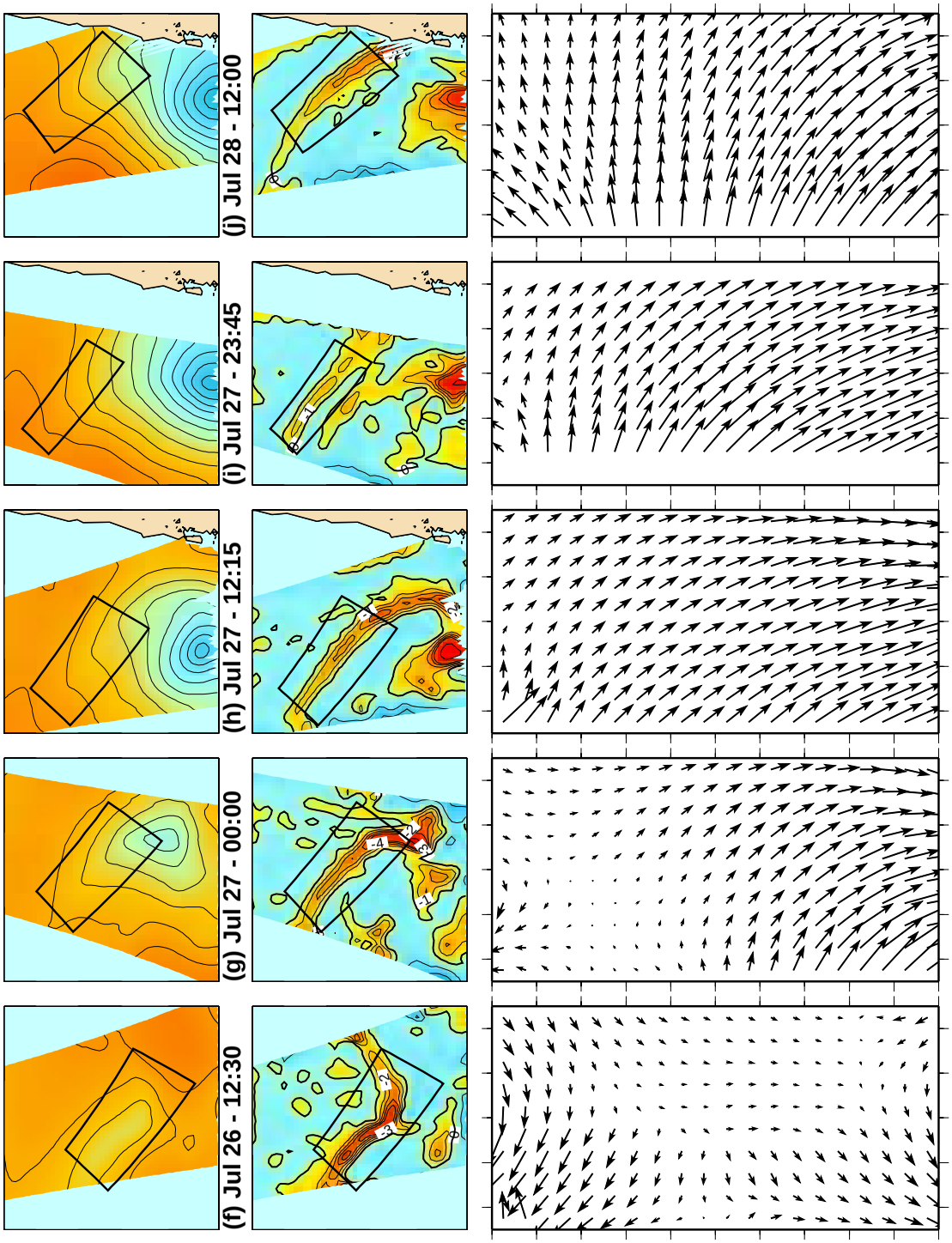

Figure 5.4: (Con't)

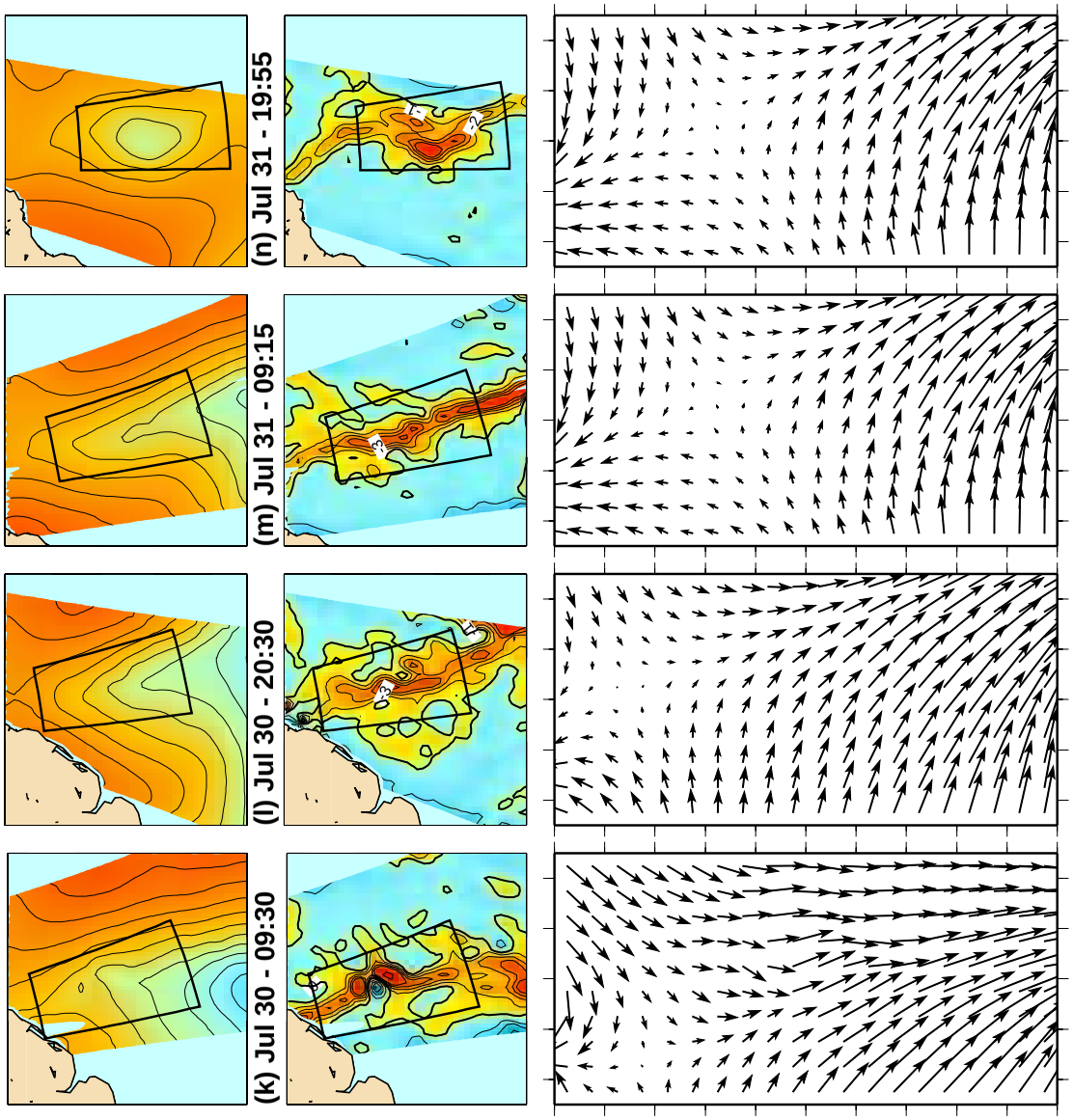

Figure 5.4: (Con't)

and divergence elements outside the box. Figure 5.5 explains how these surrounding elements create the background deformation flow in panel (a). The anticyclone northeast of the box (labeled H2) induces a northerly/northwesterly flow into the box. The smaller anticyclone southwest of the box (H1) induces a southerly flow in the frontal box. The low center (L) induces a cyclonic circulation in the southern part of the box. Recall that the magnitude of the wind induced by the highs and lows is inversely proportional to the distance from the vorticity and divergence elements in those highs and lows. The combination of the induced wind fields result in the deformation field observed in Fig. 5.4, with a strong cyclonic component in panels (a) and (b) due to the proximity of the low center (L).

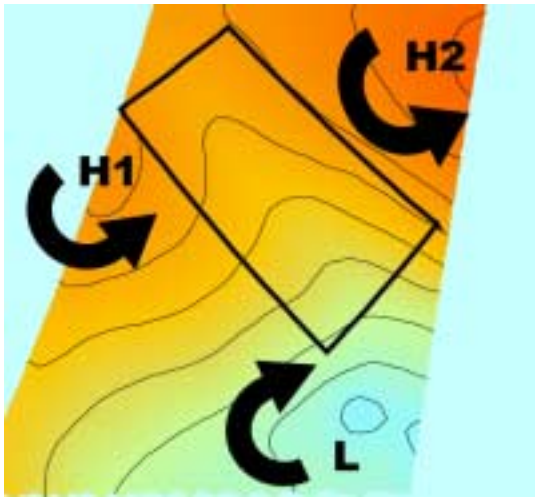

Figure 5.5: Role played by surrounding synoptic features in the environmental flow

On July 26, at 12:30 UTC (step f), the front is taking on the shape of a classical incipient wave. An elongated, almost closed isobar is visible. This step shows the first signs of secondary wave growth. Note that the positioning of the frontal box is more arbitrary in this case since the wave has more of a V-shape. However, the estimation of the along-front stretching remains within the uncertainty discussed in section 5.1.4.

In steps (g) through (j), the environmental flow bears the signature of the strongly cyclonic pocket of vorticity corresponding to the low. The influence of the low is stronger at the bottom of the frontal box and decreases northwestward as we move away from the low center. This can also be said of July 29. However, in steps (l) through (o), as the low center migrates southeastward (i.e. away from the box, not shown in the figures), the environmental flow is characterized once again by a strong confluent-diffluent component. On July 31 at 09:15 UTC, a new vortex appears, characterized by closed isobars and an incipient wave signature. This cyclone later follows its own life cycle (not shown in the figures).

The time evolution of the along-front stretching ($\partial v/\partial y$) by the environmental flow is shown in the top panel of Fig. 5.6. The x-axis is labeled in hours, starting on July 24, at 00:00 UTC. The divergence fields for 6 of the 14 steps are plotted for reference. The along-front stretching decreases over the first 60 hours to reach its lowest value (0.2×10^{-5} s^{-1}) at step (f), when the first frontal wave starts to grow significantly. The stretching increases anew as the cold front develops, rotates and crosses over South America (steps (f) through (l)). Then it decreases to reach 0.2×10^{-5} s^{-1} again when the second frontal wave starts to grow. This is remarkably consistent with the theoretical results of BT94, who predict that the basic-state strain rate should decrease below a 0.6×10^{-5} s^{-1} threshold before frontal waves can grow significantly.

In the bottom panel of Fig. 5.6 is plotted the along-front average vorticity (dashed line). It doubles over the 60 hours preceding the initiation of each frontal wave. This makes sense intuitively, since the shear and vorticity of the front are increasing as a result of frontogenesis. Values ranging from 0.5×10^{-4} to 1.1×10^{-4} s^{-1} are also consistent with Rivals et al. (1998). The vorticity waviness (solid line) shows a minor peak at t=24 hours and two major peaks at steps (f) and (n) when the two frontal waves start to grow. The instabilities grow when the vorticity maximum (i.e. the inflection point shear) exceeds a critical value (Brown, 1980). These two peaks correspond to

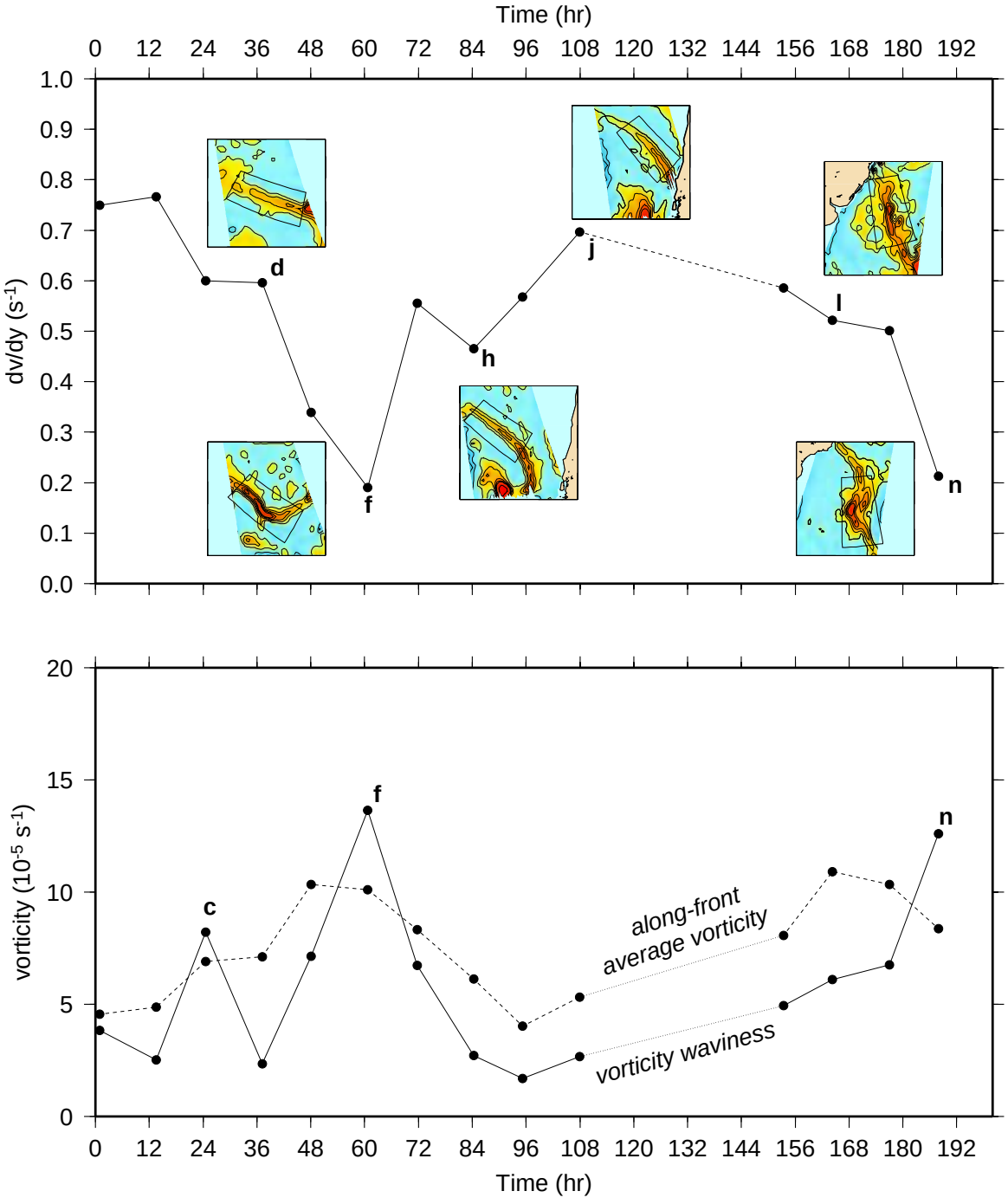

Figure 5.6: Time evolution of the along-front stretching by the environmental flow

the times when the instabilities stand out the most against the average vorticity of the front and match the times when the strain rate reaches its lowest value.

In Fig. 5.7, these results are presented in a different format for comparison with Renfrew et al. (1997) and Rivals et al. (1998). On the x-axis, the along-front stretching is normalized by BT94's 0.6×10^{-5} threshold. This clearly identifies the values that theoretically allow frontal wave growth (left of the x=1 line) from the values that prevent frontal wave growth (right of the x=1 line). The y-axis is the derivative of the waviness, used as a proxy for growth. In this graph, points are expected to fall either in the top left quadrant (low strain rates - high growth rates) or in the bottom right quadrant (high strain rates, low growth rates). Letters corresponding to several time steps of Fig. 5.4 are indicated for reference. By following the curve from (a) to (n), one can capture at a glance the environmental conditions in which the front evolves and verify if the frontal waves grow under the stretching conditions predicted by theory. In our case, the growth rates are high (e and n) only when the strain rate is small (top left quadrant). When the strain rate is high, the growth rates are smaller than 1×10^{-9} s^{-2} and sometimes negative (although not exclusively in the bottom right quadrant). The values are in overall agreement with Rivals et al. (1998) (but their analysis contains only 4 points) and Renfrew et al. (1997) (although they plot only the individual points and do not connect the different life cycles). A number of our points fall between 0.8 and 1 in normalized stretching. This suggests that BT94's theoretical threshold might be greater than the threshold under which the stretching should fall for growth in the real atmosphere. For the second wave in particular, the three points preceding the stage when the wave starts to grow (n) fall between 0.8 and 1. Yet, the wave only grows when the strain rate falls much lower (0.35 normalized stretching).

Figure 5.8 shows average frontogenesis (F_x) due to each wind component. In the top panel, absolute values are plotted, starting with the total frontogenesis F_0, then the individual components F_ψ, F_χ and F_θ. The general tendency of F_0 is to increase

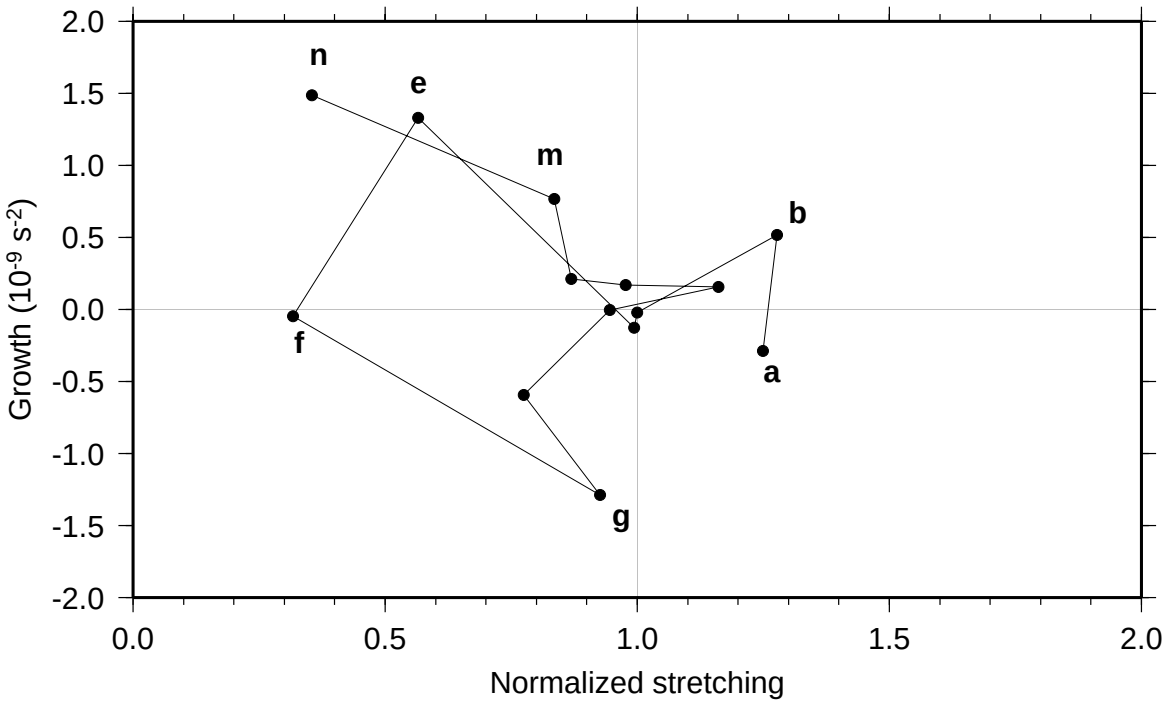

Figure 5.7: Frontal wave growth rate vs. normalized stretching

during the development of each front and reach a local maximum when the frontal wave starts to grow. For the first frontal wave, the maximum is reached at t=60 hours (i.e. same as the local maximum in vorticity waviness). For the second frontal wave, the maximum is reached 12 hours before the peak in waviness. This increase in F_0 is consistent with the concept of increasing frontogenesis as the front develops. However, notable differences can be observed in the three components of F_0. This can be seen in the top panel of Fig. 5.8 or in the bottom panel, where F_ψ, F_χ and F_θ are plotted in relative values (relative to the total F_0), for comparison with Rivals et al. (1998). Whereas F_χ increases significantly as the first front develops (from t=0 to t=60 hours), F_ψ varies mildly and F_θ decreases to a (negative) minimum at t=60 hours. This suggests that the cross-frontal ageostrophic circulation plays a major role in strengthening the front (F_χ), whereas the background deformation becomes frontolytical when the first frontal wave starts to grow (F_θ). Rivals et al. (1998) also

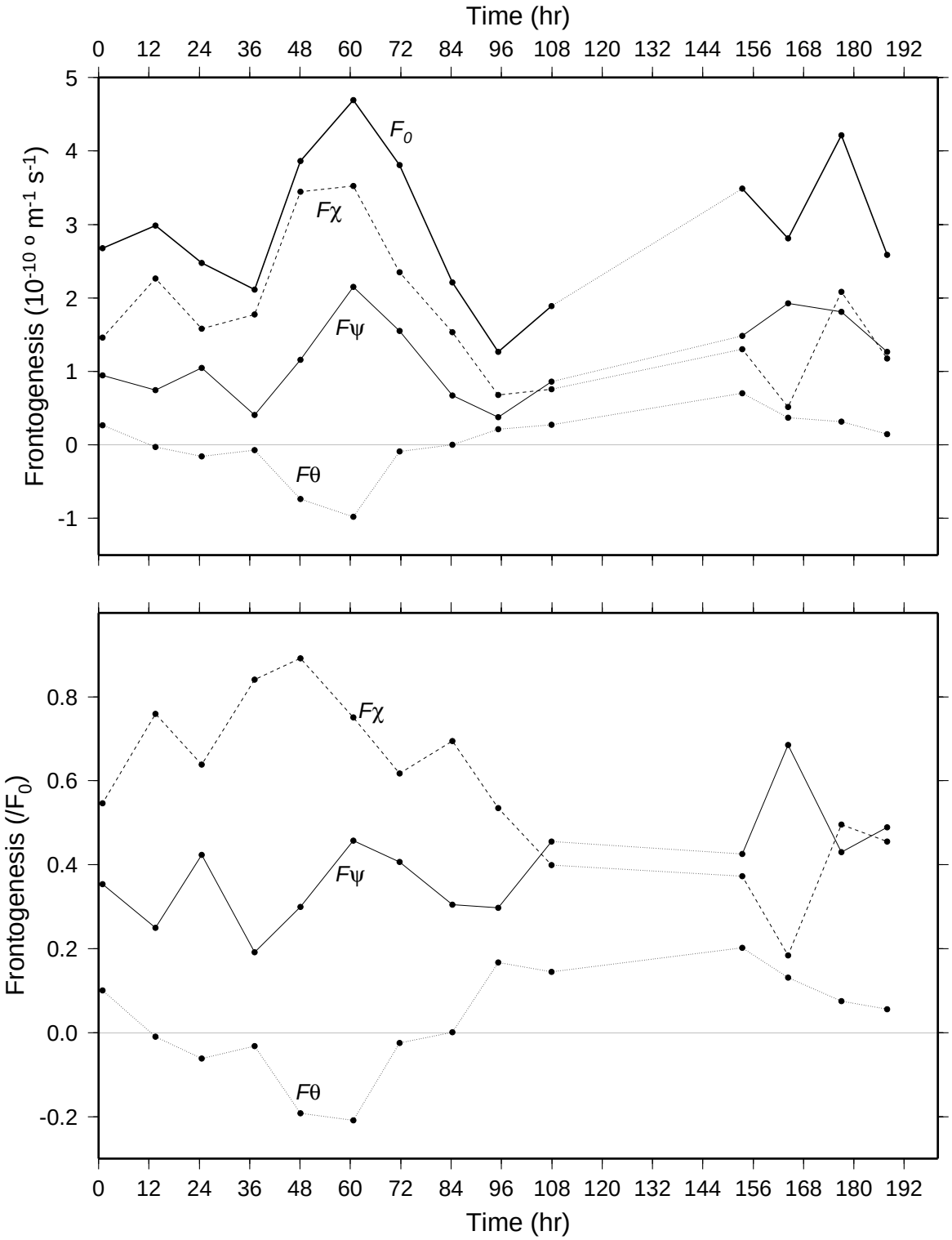

Figure 5.8: Frontogenesis due to the different wind components. Top: absolute values. Bottom: values relative to F_0.

observe a predominant role played by the ageostrophic circulation. However, they observe (in a 5-point time series) that the frontal wave grows at a time when F_χ decreases. The reverse is observed in our case.

In stark contrast, frontogenesis during the second frontal wave development is characterized by F_ψ and F_χ of similar magnitude and only a mild decrease in F_θ. This suggests that the two frontal waves might follow different scenarios. The first one might require a relaxation of the environmental deformation and associated frontogenesis, possibly counteracting frontogenesis due to the cross-frontal ageostrophic circulation, whereas the second one grows in a front where the ageostrophic flow has ceased to play a dominant role.

In order to better characterize that difference, we turn to upper-level analyses. 500-mb heights were obtained from ECMWF and are shown in Fig. 5.9, along with the 500-mb vorticity calculated from the gridded wind vectors. In the left column, the QS-derived pressure fields are plotted for reference (same as Fig. 5.4 - 4-mb contour intervals, reds (blues) represent high (low) pressures). The center column shows 500-mb heights (60-m intervals, reds (blues) represent high (low) heights). The right column shows 500-mb vorticity, with cyclonic (anticyclonic) vorticity in red (blue).

The main feature of interest is highlighted by small black arrows in panels (c), (d) and (e). As the surface front develops and strengthens, a short wave on the upper-level jet moves in. Its signature is weak but apparent as a wavy pattern in the 500-mb heights and as a maximum in upper-level vorticity. The subsequent growth of that upper-level feature is coincident with the deepening of the frontal wave beneath it (panel (f) through (j)), which suggests a baroclinic growing mode in the later stages. In the early stages, the type of kinematic analysis performed here does not reveal which of the surface or upper-level feature is driving the other. Although there has been some discussion about surface PV anomalies inducing upper-level anomalies (in this case, the surface frontal wave inducing the upper-level short wave), current thinking favors the notion of upper-level anomalies existing first and independently of

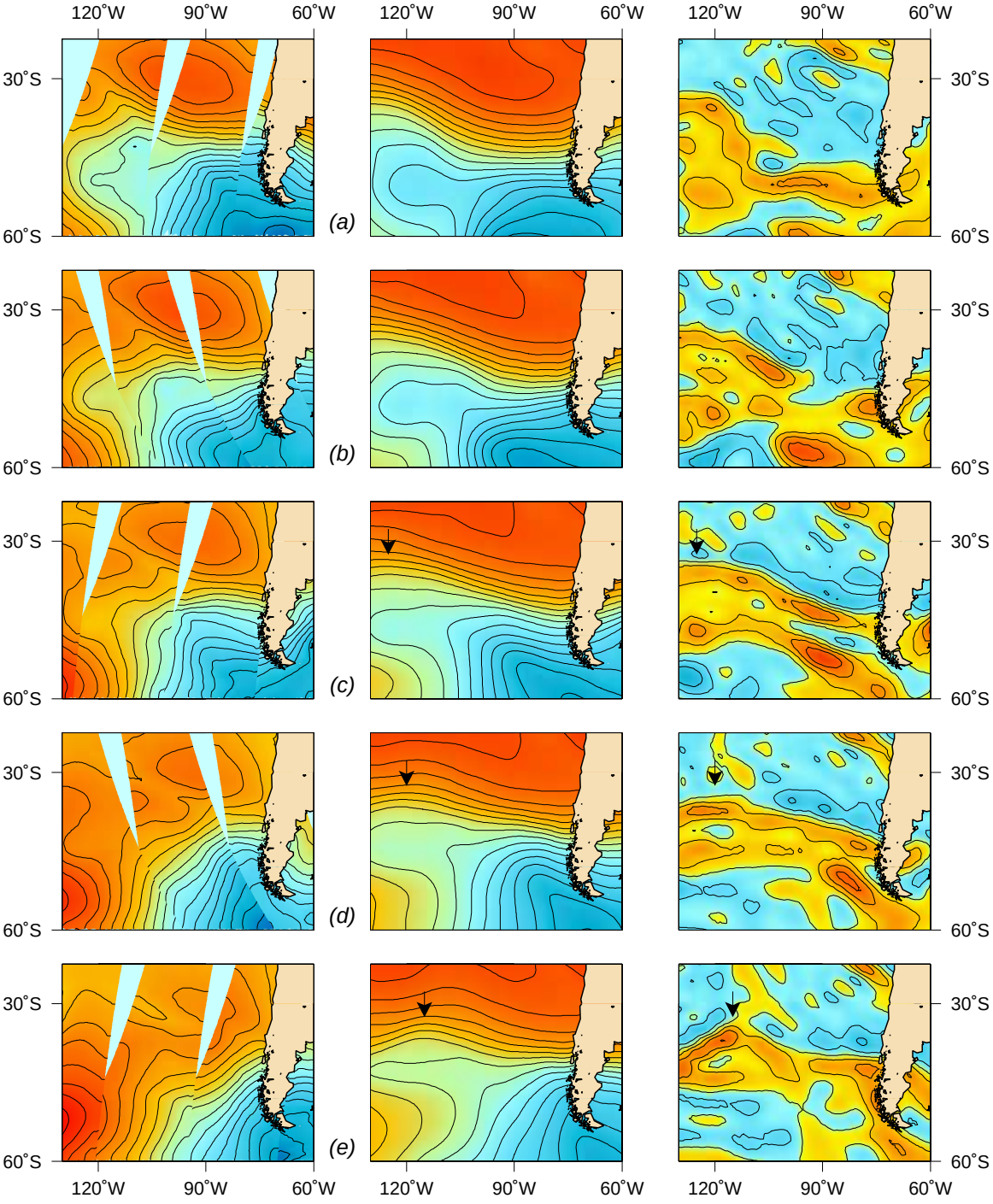

Figure 5.9: Comparison of surface and upper-level features in the development of two frontal waves. Left: surface pressure. Center: 500-mb heights. Right: 500-mb vorticity (same scales as figure 5.4). The black arrows indicate a short wave on the upper-level jet.

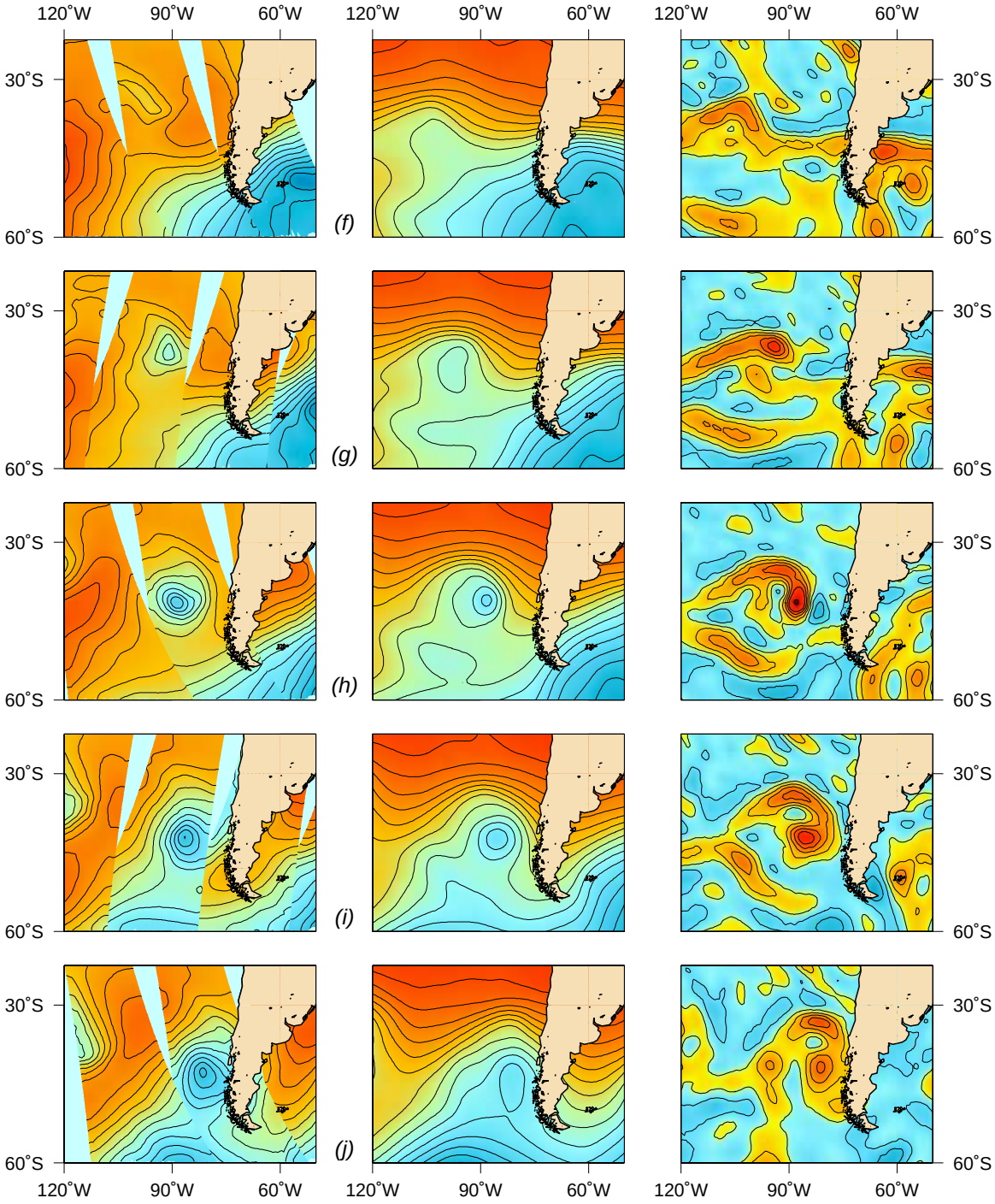

Figure 5.9: (Con't)

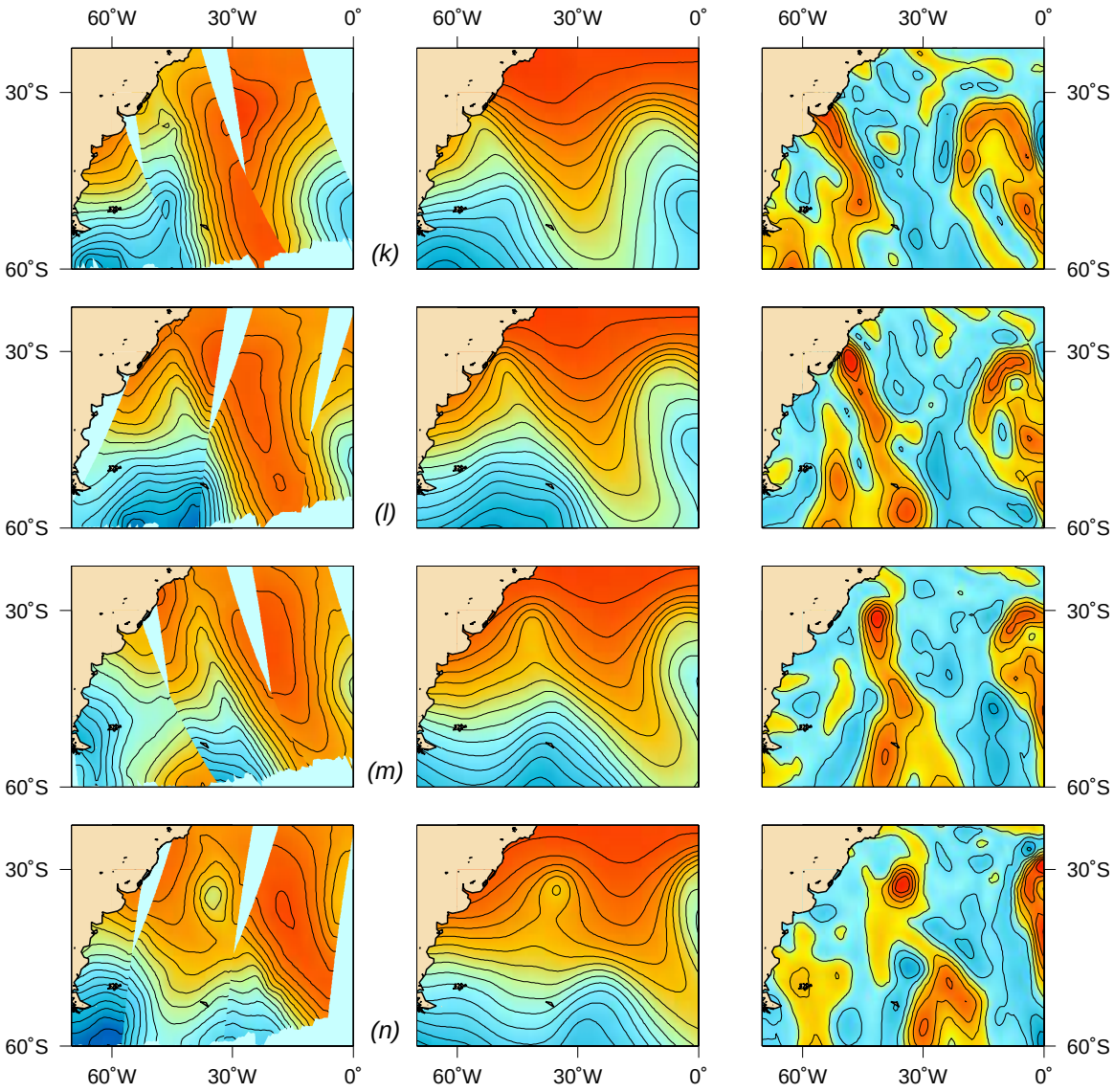

Figure 5.9: (Con't)

the surface front. Subsequent growth is then dependent upon a favorable configuration and timing of the two features.

In contrast, the environment in which the second surface frontal wave grows is very different. A large meridionally elongated surface trough extends North to Brazil and has a very similar counterpart at upper-levels, in the form of a meridionally elongated trough with a strong vorticity signature. The upper-level front is lagging slightly westward compared to the surface front. The upper-level trough and high-vorticity are already present above the surface front 48 hours before the occurrence of the frontal wave (panel (k)). However, the secondary cyclone starts to form only 48 hours later (panel (n)), when the upper-level depression stands out in the vorticity field as an isolated vortex.

These results suggest that the two frontal waves followed distinct scenarios:

1. In the first case, the front strengthens as a result of frontogenesis due mainly to the divergent ageostrophic cross-frontal circulation. Then three processes become important: (i) The along-front stretching associated with the environmental flow decreases with time and reaches a minimum of 0.2×10^{-5} s^{-1}. (ii) The environmental flow becomes frontolytic. (iii) A short upper-level wave moves in above the surface front. The front then becomes unstable and a secondary cyclone develops, with a clear signature in both the surface and upper-level fields.

2. In the second case, the large-scale trough in which the front is embedded also exists at upper-levels, with high values of vorticity. The frontal surface has a slight westward tilt with height. Frontogenesis is relatively high but *not* due for the most part to the divergent ageostrophic wind. The environmental flow does not become frontolytic although the along-front stretching associated with it decreases. When it reaches a minimum of 0.2×10^{-5} s^{-1}, the secondary cyclone develops.

This second scenario is reminiscent of Sinclair and Revell (2000)'s fourth type of extratropical cyclone (type T) forming beneath a preexisting upper-level trough. It is also reminiscent of Carleton (1981)'s instant occlusion, thought to be associated to strong meridional blocking (i.e. elongated meridional trough) and cold air surging to the west of a long wave trough. In contrast, the first scenario resembles the typical frontal waves observed in the North Atlantic (e.g. Rivals et al., 1998). In both cases, there is a clear connection between the surface and the upper-levels, and the subsequent cyclone growth seems to have a baroclinic component, as suggested in recent studies (e.g. Joly, 1995). However, the "timing" of the connection with the upper-level feature in the first case (i.e. with the fast-moving short wave in the upper-level jet) is more critical than in the second case.

As mentioned earlier, many fronts observed with the QS data are stable, long-lived and decay without breaking up. Moreover, many fronts showing "weaknesses", peaks in vorticity or wavy patterns, strengthen in the following hours or days and pursue their frontal life cycle. Many frontal waves are thus not developmental. The coincident action of the different factors listed above is thus critical in spawning a secondary cyclone. In order to better characterize their respective roles, two fronts are analyzed in the following sections: first a stable front, then a front in which an instability fails to grow.

5.3 Comparison with a stable front

The motivation in this section and the next is the following: various processes have been identified in the formation of two types of frontal waves in the previous analysis. Does the QS data set contain a similar frontal life cycle in which these processes would play similar roles, but with a different outcome?

The July 1999-June 2000 QS period was searched for such cases using animations

of pressure and divergence fields. The front analyzed here is described briefly in Fig. 5.10. Since the front is stable and long-lived, the 14-panel history is omitted here and replaced by a single panel in which three characteristic stages of the life cycle are presented. In panels (a) and (c) the three corresponding swaths of divergence and pressure respectively are shown. Note that the three swaths take place at different times (indicated below the swaths). However, plotting them together on the same map shows the distance traveled by the front in time and its geographical extent.

The front is a remnant of a storm over the Indian Ocean and is first shown on July 26, 1999 around 00:00 UTC (left swath). It bears the typical comma-type signature of mature storms, visible as a line of convergence in panel (a) and as a kink in the isobars in panel (c). The tail of the front is oriented southeast-northwest. Two days later (July 28, 1999 around 00:00 UTC), the front has rotated and is now taking on a more south-north orientation, with its tail reaching southwest Australia (middle swath in panels (a) and (c)). Two days later, the front is fully oriented south-north and has kept its identity in both the divergence and pressure fields. In the following days, the trough and the front weaken. Late during the decay, as the trough starts to merge with the polar trough, a small depression starts to form (3-4 mb) but then fills in (not shown here). Over the 8-day life cycle, there is no sign of instability or wave growth in the front.

In panels (b) and (d), the 500-mb vorticity and 500-mb heights respectively are shown at each of the three stages depicted in panels (a) and (c). They show that there is a well-formed upper-level trough corresponding to the surface trough. The position of the surface and upper-level fronts reveals that the front tilts westward with height. The upper-level trough already exists in the early stages of the front life cycle, in a manner similar to the Atlantic Ocean case east of South America described in the previous section. However, in contrast with the Atlantic Ocean case, no secondary vortex is formed.

The wind partitioning and kinematic analysis were applied to the 14 QS swaths

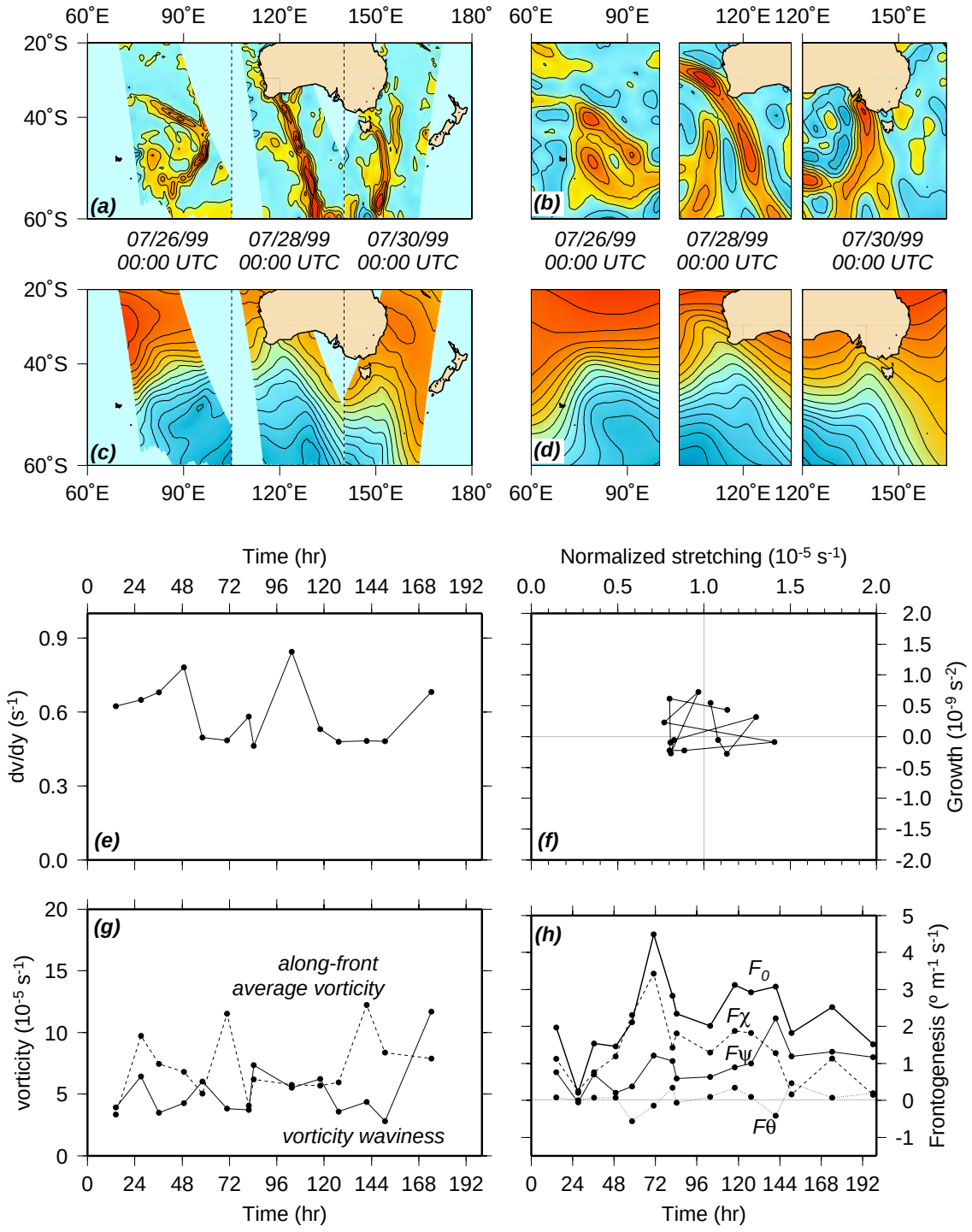

Figure 5.10: History of a stable front (a) Divergence from QS at three stages of the front life cycle (b) 500-mb vorticity (c) QS-derived surface pressure (d) 500-mb heights (e) Environmental along-front stretching (f) Growth vs. stretching (g) Vorticity waviness (h) Frontogenesis

describing the front life cycle. Panel (e) shows the resulting environmental along-front stretching. It varies between 0.46×10^{-5} s^{-1} and 0.85×10^{-5} s^{-1}. One will note that it never reaches the 0.2×10^{-5} s^{-1} observed in the Pacific and Atlantic cases (previous section). However, as in those cases, one will also note that it remains for long periods of time below BT94's critical threshold of 0.6×10^{-5} s^{-1}. This suggests either that the real-case threshold is lower than their theoretical result, or that a strain rate below 0.6×10^{-5} s^{-1} might be necessary but not sufficient for frontal wave growth.

Panel (g) shows the along-front average vorticity and vorticity waviness. Three peaks in average vorticity can be observed, which means that the front as a whole intensifies at those times (higher shear, higher vorticity). However, no isolated vorticity peak appears (i.e. no peak in waviness), except at the very end. This means that no individual vortex stands out in the front throughout most of the life cycle. This might be due to the fact that the environmental strain rate remains relatively high. The last peak in waviness happens at a time when the strain rate is increasing (0.68×10^{-5} s^{-1}), which might also explain why no vortex grows at that time either.

In panel (f), growth is plotted vs. normalized environmental along-front stretching as explained for Fig. 5.7. This plot emphasizes the fact that the stretching is contained within a narrow range of values and that no significant growth is observed throughout the time series. All the points are huddled together, which highlights the fact that the front and the environment overall keep their characteristics throughout the 8-day period.

Finally, panel (h) shows frontogenesis due to the total wind (F_0) and to each component (F_χ, F_ψ and F_θ). F_0 increases, remains relatively high and decreases only towards the end of the life cycle. The divergent ageostrophic component F_χ accounts for most of the frontogenesis in the early stages, then decreases towards the end, exhibiting a behavior very similar to that of F_χ in the Pacific/Atlantic case (previous section). F_ψ is small in the early stages and increases towards the end. Frontogenesis due to the environmental flow (F_θ), in contrast with the Pacific/Atlantic case, remains

overall constant and close to zero. In particular, it does not become significantly frontolytic for a long period of time.

In summary, the behavior of this stable front shares some similarities with the Pacific/Atlantic case. It starts as the remnant of the baroclinic zone associated with a mature storm. It rotates from a southeast-northwest to a fully north-south orientation and maintains its identity for several days. Frontogenesis is high in the early stages, with a major role played by the cross-frontal divergent ageostrophic circulation, and decreases with time. However, this front is different, with higher values of the environmental stretching and neither a frontolytic nor frontogenetic role played by the environmental flow. Since high values of vorticity do exist at upper-levels, these results suggest that the surface conditions might not be optimal in this case for the growth of a vortex on the tail of the front. The environmental stretching deformation might not relax to sufficiently small values. Note however that the present analysis does not encompass the full range of components involved in cyclone development.

5.4 Comparison with a non-developmental wave

In this last case study, the July 1999-June 2000 QS period was searched for a case of a long-lived front where an instability can be detected but no vortex deepens significantly. An "incipient frontal wave", as one might call it, appears at one synoptic time, but is damped out in the following hours by a strengthening of the front.

The 13-step life cycle is summarized in Fig. 5.11 where only 7 characteristic swaths are shown for reference. Since important details are necessary for the understanding of the frontal evolution, the full quasi-synoptic picture is shown at each stage, with QS divergence in the top row, QS-derived surface pressure in the second row, 500-mb heights in the third row and 500-mb vorticity in the bottom row.

In column (a), a mature cyclone is depicted south of the Cape of Good Hope on June 24, 2000 around 00:00 UTC. Its cold front is curving back to the west and

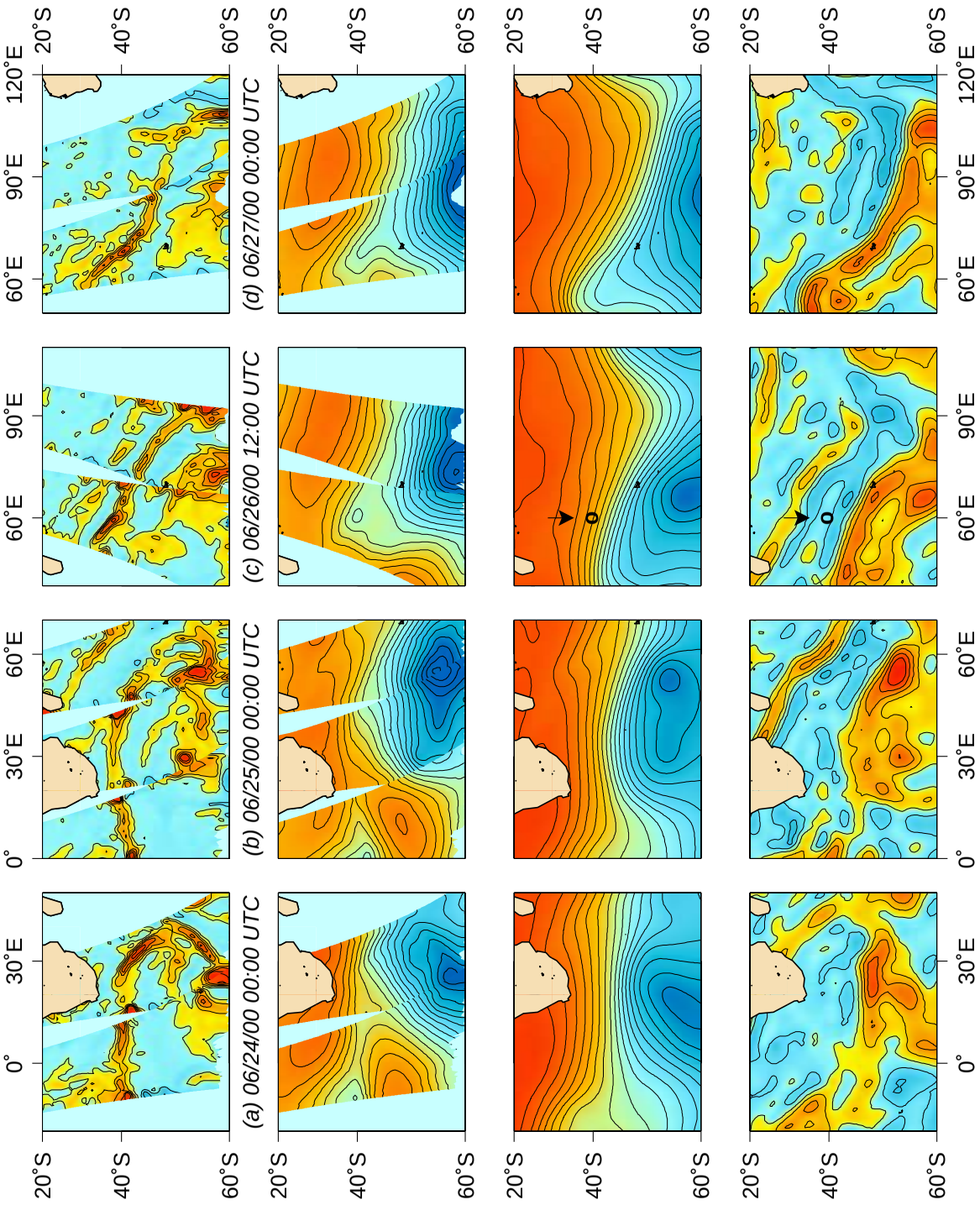

Figure 5.11: Life cycle of a front over the Indian Ocean. Top row: divergence from QS. Second row: QS-derived surface pressure. Third row: 500-mb heights. Last row: 500-mb vorticity

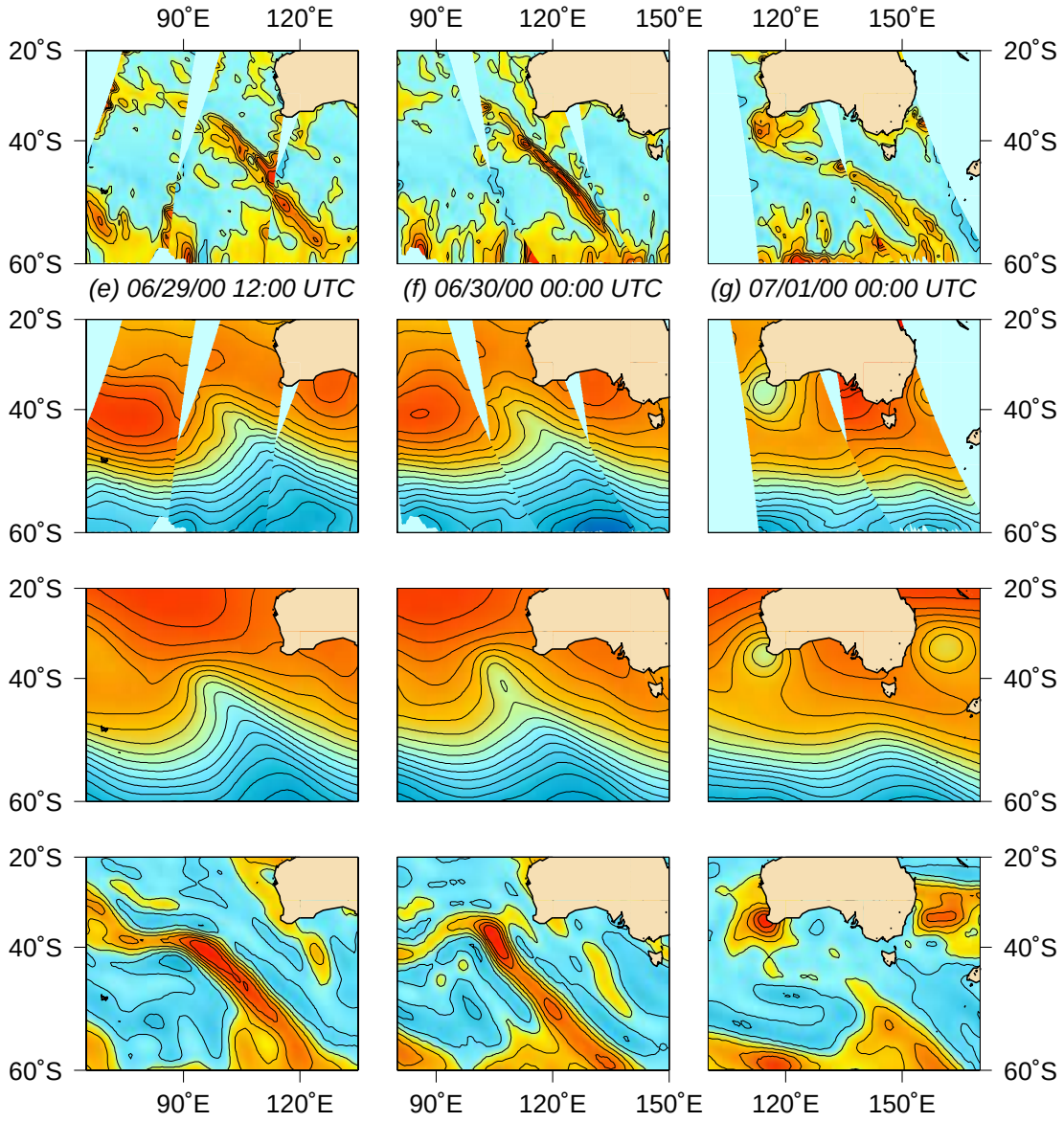

Figure 5.11: (Con't)

the storm can be seen in column (b) to have a wide zonal extent on 60 degrees of longitude. The feature of interest appears in column (c) in the form of a wavy pattern in the convergence line corresponding to the front and a small depression along the front in the pressure field. The position of this small low is highlighted by a black circle and a little black arrow in the 500-mb plots for future reference.

As can be seen in column (d) through (f), this depression does not deepen and the front maintains its shape (a straight line) and orientation (southeast-northwest) for 4 more days as it moves eastward. Then only, as the tail of the front approaches Australia, a vortex appears and grows into a small cyclone, as shown in column (g) on July 1st, 2000. The rest of the front can be seen to weaken and decay south of Tasmania.

This case is of particular interest because it shares many similarities with our original Pacific case study (the first frontal wave in section 5.2). However, the frontal instability does not deepen. The wind-partitioning and kinematic analysis was carried out on the 13 QS swaths describing the life cycle of this front to shed some light on the differences between the two waves. The results are summarized in Fig. 5.12.

Panel (a) shows the along-front stretching by the environmental flow. Letters corresponding to the time steps depicted in Fig. 5.11 are indicated for reference. The time step at which the frontal wave is first seen in the pressure and divergence fields is "c". The stretching can be observed to decrease over the 48 hours preceding step "c" to reach a minimum value of 0.33×10^{-5} s^{-1}. It then increases again to a maximum and decreases to 0.6×10^{-5} s^{-1} when the vortex develops on the tail of the cold front. The overall pattern of increasing and decreasing strain rate resembles the one observed in Fig. 5.6. The frontal waves appear when the strain rate is at a minimum.

Panel (c) shows the variations of the along-front average vorticity (dashed line). Note the larger variations at the beginning of the life cycle, when the vorticity doubles (10×10^{-5} s^{-1}) and then decreases back to 4×10^{-5} s^{-1} over 24 hours. In contrast the

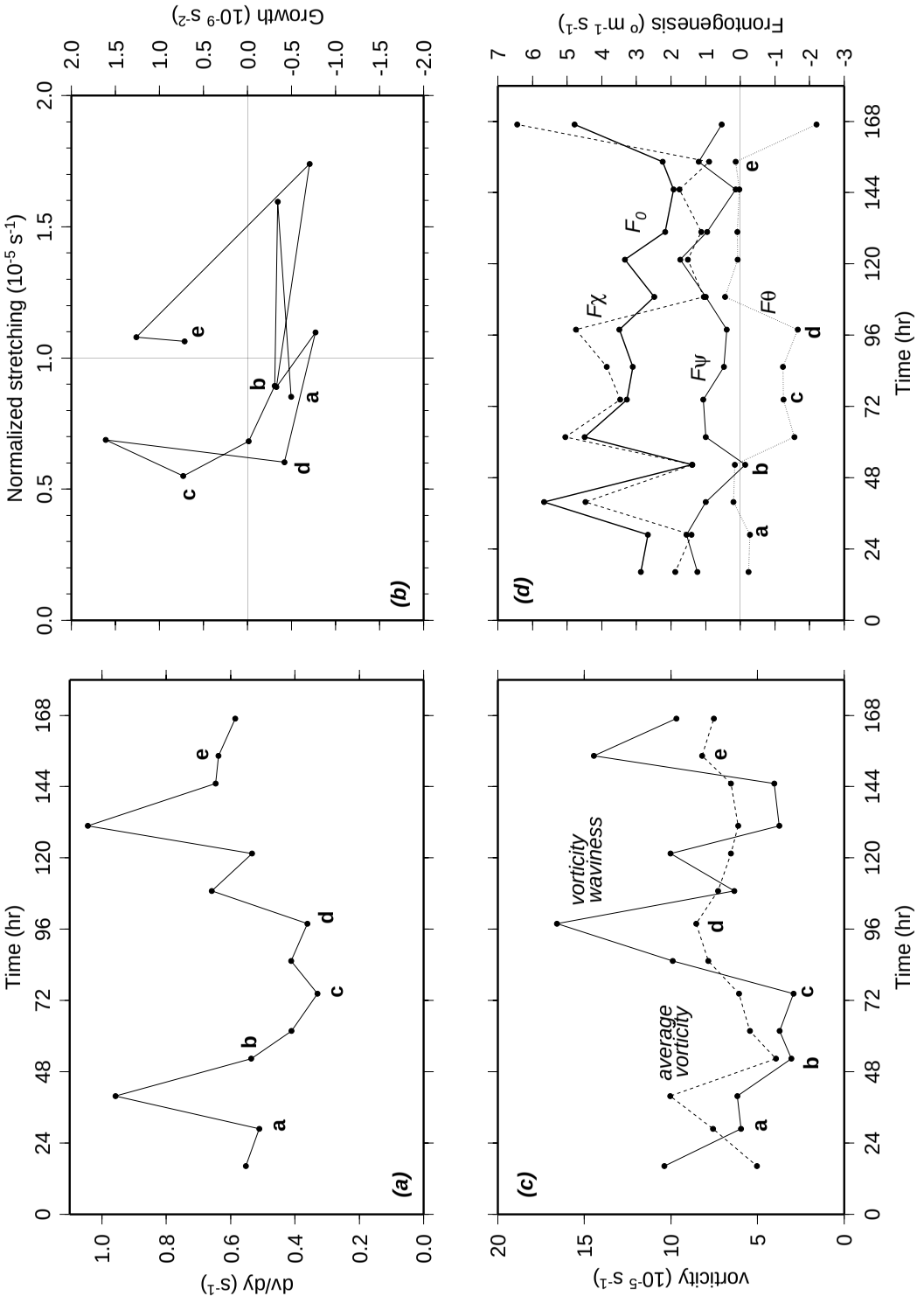

Figure 5.12: History of a front over the Indian Ocean (a) Environmental along-front stretching (b) Growth vs. stretching (c) Vorticity waviness (d) Frontogenesis

vorticity remains more or less constant in the subsequent stages (about 7×10^{-5} s^{-1}). The solid line shows two peaks in the vorticity waviness. The first one corresponds to the incipient frontal wave that fails to grow, whereas the second one corresponds to the vortex developing into a small cyclone off the coast of Australia. Note however that the first peak appears at step (d), 24 hours after the wave is first observed in the pressure and divergence fields. The wave was thus growing for at least 24 hours, even though the depression did not deepen significantly at later times. Note also that at step (c), when the incipient frontal wave first appears, the average vorticity is 6×10^{-5} s^{-1} and the peak vorticity 3×10^{-5} s^{-1}, which means a total of 9×10^{-5} s^{-1}. It then grows to a total of 25×10^{-5} s^{-1} over 24 hours. For comparison, in the Pacific Ocean case (see Fig. 5.6b), the total vorticity also grows from 9×10^{-5} s^{-1} to 24×10^{-5} s^{-1} in 24 hours. The two frontal waves are thus very similar in structure and environmental conditions. This is emphasized in Fig. 5.12b where growth is plotted as a function of normalized stretching. The growth phase of this incipient frontal wave also takes place in the 0.5-0.7 range of normalized stretching.

Fig. 5.12d highlights yet other similarities with the Pacific Ocean case. It shows total frontogenesis (F_0) and its components (F_χ, F_ψ and F_θ). Frontogenesis is high during the first phase of the front development and then decreases at later times, to increase at the very end when the secondary vortex grows. The divergent ageostrophic component (F_χ) is the main contributor to frontogenesis. F_ψ shows smaller values and variations. F_θ is close to zero and becomes frontolytic when the first frontal wave and the secondary vortex grow. Whereas frontogenesis is high during the strengthening and the rotation of the front (i.e. when the front is "young"), frontogenesis is lower later on (i.e. when the front is "mature").

These results are consistent with our previous discussion of the mechanisms involved in frontal wave growth. The front first strengthens mainly through the convergence of the cross-frontal ageostrophic circulation. Meanwhile, the environmental along-front stretching decreases and the environmental flow becomes frontolytic. The

conditions are then favorable to the growth of instabilities. However, in this particular case, even though the wave can be observed to grow for 24 hours, it does not deepen into a secondary cyclone.

An explanation for this can be found in Fig. 5.11c, where the location of the surface instability is shown at upper levels with a black circle and a small arrow. The instability appears under the upper-level jet, in no particular configuration favorable for growth (like the exit of the jet). No short wave or vorticity anomaly are present. Two bands of positive vorticity can be observed, one south corresponding to the decaying cyclone and one north corresponding to an older system, whose trailing front can also be seen in panel (b) in the top right corner. The surface instability, however, lies underneath a region of anticyclonic upper-level vorticity. This is thought to be the main reason why the frontal wave fails to deepen. Although the surface conditions are favorable, and the wave presumably grows for 24 hours from a predominantly barotropic conversion of energy from the frontal shear, it does not shift to the predominantly baroclinic mode necessary for deepening into a secondary cyclone.

At the end of the frontal life cycle, the environmental along-front stretching decreases again and the environmental flow becomes frontolytical. The upper-level trough has moved eastward and the surface and upper-level front are now in a favorable configuration. High upper-level vorticity exists above the tail of the surface cold front. At the end of the tail, a vortex grows into a secondary cyclone. Note that in this case, the environmental along-front stretching is 0.6×10^{-5} s^{-1} when the vortex grows, the threshold proposed by BT94. Note however that the upper-level vortex precedes the surface development and that the surface vortex seems from the start to be driven from upper-levels.

5.5 Discussion

Three marine fronts have been analyzed. Their evolution is followed for several days up to a week. By calculating divergence and pressure fields from QS surface wind vector measurements, a "snapshot" of the fronts is obtained roughly every 12 hours. With an attribution technique, the surface wind field around the front is partitioned in nondivergent, irrotational and harmonic (or environmental) components. The evolution of the environmental along-front stretching and frontogenesis due to each wind component are analyzed. Their role in enhancing or inhibiting frontal wave growth is assessed, in conjunction with the role played by upper-level features.

It was found that the three fronts shared some characteristics. Originally the remnant of a mature cyclone, they rotate from a southeast-northwest orientation to a south-north orientation and survive their parent cyclone for several days. In doing so, they maintain their identity in surface convergence and inflection of the isobars. Frontogenesis is high in the early stages and due for a large part to the convergence of the cross-frontal ageostrophic circulation at the surface. Frontogenesis decreases with time as the front matures.

In these three fronts, a total of 4 frontal waves can be detected. A comparison of the 4 cases reveals that the environmental along-front stretching drops to 0.6×10^{-5} s^{-1} or below (down to 0.2×10^{-5} s^{-1}) at the time the frontal waves start to grow. In contrast, the stretching does not decrease significantly in the case of the stable front. This agrees with the general idea that a strong strain rate will "stretch out" the wave and inhibit its growth, whereas a relaxation of the stretching will allow the wave to develop. The present results are consistent with BT94's theoretical threshold of 0.6×10^{-5} s^{-1} under which the strain rate should fall before an instability can transition from linear to non-linear mode and grow significantly, although they suggest a lower threshold of 0.4×10^{-5} s^{-1}.

Tied to the environmental along-front stretching is the frontogenetical or fron-

tolytical effect of the environmental flow. Following a similar argument, it is generally thought that as the background flow relaxes, it becomes frontolytical and favors the growth of instabilities at the expense of the front itself. This is observed here in the two cases of frontal waves appearing in the fronts when they are still "young", and in one of the two cases of vortices developing on the tail of the fronts at "maturity". Moreover, frontogenesis due to the background flow remains close to zero in the case of the stable front. A frontolytic environmental flow is thus probably necessary for instabilities to develop on young fronts experiencing overall frontogenesis otherwise. That frontolytic component can be thought of as counteracting the frontogenesis due to the divergent ageostrophic flow. In mature fronts, because total frontogenesis is not as strong, frontolysis by the background flow is not as necessary.

Out of the four observed frontal waves, three deepen significantly and evolve into secondary cyclones whereas one is damped by a subsequent strengthening of the front. It is argued here that the three cyclones deepen due to a favorable configuration between the surface front and the upper-levels. In the two cases of vortices growing on the tail of the "mature" front, the upper-level trough is meridionally elongated and contains a lot of vorticity coincident with the surface vortex. The front is tilting westward with height. The configuration is favorable to baroclinic development. In the third case, in which the frontal wave appears on a "young" front, a fast-moving short wave riding the upper-level jet is observed above the instability at the time the instability starts to grow. The surface wave might be initiated by a barotropic conversion of energy from the frontal shear, but subsequently grows baroclinically.

The fourth frontal wave, which does not deepen, can be observed to grow temporarily at the surface. But it lies underneath an upper region of anticyclonic vorticity. The surface wave might also be initiated barotropically, but lacks the connection with the upper-levels and the baroclinic component necessary for significant growth. Only four days later, as the upper-level trough extends to a better configuration, does a surface instability grow into a deeper vortex. These results also reinforce the concept

proposed in the past that some frontal waves might be shallow anomalies in their early stages and might only grow significantly if they extend vertically and connect with the upper-levels.

To give these statements some generality, one could think of frontal waves as instabilities occurring relatively often in trailing cold fronts. A simple visualization of the QS pressure and divergence fields for the July 1999-June 2000 period indeed reveals many such "wavy" patterns and "weaknesses". However, the extent to which these instabilities can deepen into secondary cyclones is dictated by the coincidence of several factors, among which the stretching deformation and frontolysis by the environmental flow and an optimal connection with the upper-levels. Few of the frontal waves detected in the QS period actually deepen into deep vortices. Frontal waves are common, but deep secondary cyclones are rare.

Chapter 6

CONCLUSIONS

Using the uniquely dense ocean surface wind vector measurements from the SeaWinds-on-QuikSCAT scatterometer, surface pressure and kinematic components of the surface wind field can be evaluated with unprecedented resolution and the evolution of fronts and frontal waves can be examined in detail. In this study, three fronts have been analyzed over the Southern Ocean in the July 1999-June 2000 period.

1. An attribution technique making use of free-space Green's functions has been applied to the surface wind field in the frontal region. It was shown that the technique, originally designed for model analyses by Bishop (1996a), can be adapted to scatterometer data. It provides an efficient way of partitioning the wind field into nondivergent and irrotational wind components associated with vorticity and divergence elements in the frontal region on one hand, and a harmonic component associated with the vorticity and divergence elements of the synoptic flow on the other hand. The role played by mesoscale features at the frontal scale and the environment at the synoptic scale can thus be studied separately.

2. Using this technique, properties of the fronts have been identified which characterize the development of the fronts, the growth of frontal waves and the deepening of secondary cyclones. In particular, the along-front stretching by the environmental flow, the average vorticity and vorticity waviness, frontogenesis and frontolysis by the different wind components and the presence of upper-level vorticity anomalies are considered.

3. By comparing the evolution of the three fronts and four frontal waves, several factors inhibiting or favoring the growth of frontal instabilities have been isolated and analyzed. In particular, the large-scale flow plays a role in stretching or relaxing the front and counteracting frontogenesis due to the divergent ageostrophic circulation across the front. It was shown that frontal waves grow when the along-front stretching decreases and the environmental flow becomes frontolytic. An optimal configuration with an upper-level cyclonic vorticity anomaly is then critical in deepening the instability into a full-scale secondary cyclone.

4. The results suggest that frontal waves might occur frequently over the Southern Ocean but less frequently deepen into secondary cyclones. The above factors play a crucial role in determining where and when frontal instabilities will occur and grow. Future scatterometer measurements will thus improve our understanding and prediction of secondary cyclone development.

Suggested future work

Although the attribution technique with free-space Green's functions reveals the role played by each component of the wind, it does not necessarily reveal the *cause* of the anomalies responsible for the appearance of the instabilities in the front. This remains a critical unknown in most frontal wave studies.

The two-dimensional approach presented here shares many conceptual similarities with a three-dimensional method called *piecewise frontogenesis* described by Morgan (1999) and Korner and Martin (2000). They use a piecewise PV inversion method to calculate the wind fields associated with discrete portions of the PV field. The resulting winds are used to estimate the frontogenetical contribution of each PV anomaly. In his example of a classical extratropical marine cyclone, Morgan (1999) shows that the frontogenesis associated with the lower-troposphere thermal ridge dominates in the early stage of the development, whereas the frontogenesis associated with the

upper-level PV anomaly and the surface potential temperature anomaly increases later on.

An improved method integrating the QS wind measurements and the free space Green's function wind partitioning into the piecewise PV inversion might shed some light on the interactions between the surface PV anomalies, the measured surface winds and the upper levels. One could, for example, envision calculating surface PV anomalies from observed winds and temperature measurements.

However, despite the ever-increasing number of satellite observations, global measurements of surface air temperature are still crucially missing. Model analyses can be used but the frontal features are not necessarily collocated with scatterometer fronts. Methods have been developed for "shifting" the fronts in space or interpolating the analyses to the time of the satellite pass (Dickinson and Brown, 1996). To the extent that temperature measurements or analyses could be incorporated consistently in the analysis, such a 3D inversion method applied to the above frontal waves would reveal quantitatively the respective roles played by the surface and the upper levels in the growth of the secondary cyclones.

The incorporation of both air and sea surface temperatures will also provide an estimate of the sensible and latent heat fluxes at the air-sea interface. It is thought that these fluxes might play a major role in creating the surface PV anomalies. Using the scatterometer winds to calculate these fluxes will be an improvement over the fluxes available from global analyses and will reveal their role in observed cases of secondary cyclogenesis.

A correct analysis of frontal wave development relies heavily on the identification of vorticity anomalies in the fronts. The location, intensity and timing of these anomalies is crucial for quantifying the wave growth. The current QS data are certainly a data set of choice for identifying the anomalies from the surface wind field. Improved geophysical model functions are currently under development for retrieving surface wind vectors at 12.5 km (Paul Chang, personal communication) and 1.2 km (David

Long, personal communication) grid-spacing from backscatter measurements. With such measurements, the inner structure of fronts and instabilities will be revealed in even greater detail.

Understanding the development of secondary cyclones has obvious implications for forecasting. The last of the three cases analyzed above is a good example: an incorrect estimation of the timing of the cyclone will affect weather forecasts in southwest Australia. This problem is well-known to forecasters in Western Europe, as well as on the West Coast of the U.S. The ability to forecast such cyclones depends on the ability to detect "precursors" or precursor conditions in the atmosphere. The present study points to the environmental flow, surface and upper-level PV anomalies as potential candidates for relevant precursors. With a large amount of cases and observations, a statistical analysis of these precursors will be possible. The Northern Pacific Ocean, where the observation network is denser and the model analyses are more reliable than over most of the Southern Ocean, will be a good starting point. Frontal waves spawning secondary cyclones in the Gulf of Alaska will be the subject of a future project.

During the QuikSCAT-ADEOS II tandem mission, beginning in Spring 2003, 6-hour snapshots of the ocean will be available, which will greatly improve the analyses. Beyond the scope of fronts and frontal waves, the analysis tools presented here will find other applications. In particular, the attribution technique and scatterometer measurements will be applied to the analysis of hurricanes and the transition from tropical to extratropical cyclones, in an attempt to estimate the respective roles played by these systems and the synoptic-scale flow in which they are embedded.

BIBLIOGRAPHY

Ablowitz, M. J. and A. S. Fokas, 1997: *Complex Variables: Introduction and Applications*. McGraw-Hill.

Acheson, D. J., 1990: *Elementary Fluid Dynamics*. Clarendon Press, Oxford.

Atlas, R., S. Bloom, R. N. Hoffman, E. Brin, J. Ardizzone, J. Terry, D. Bungato and J. C. Jusem, 1999: Geophysical validation of NSCAT winds using atmospheric data and analyses. *J. Geophys. Res.*, **104(C5)**, 11,405–11,424.

Ayrault, F., F. Lalaurette, A. Joly and C. Loo, 1995: North atlantic ultra high frequency variability. an introductory survey. *Tellus*, **47A**, 671–696.

Bender, C. M. and S. A. Orszag, 1978: *Advanced Mathematical Methods for Scientists and Engineers*. McGraw-Hill.

Bishop, C. H., 1993: On the behaviour of baroclinic waves undergoing horizontal deformation. II: Error-bound amplification and Rossby wave diagnostics. *Q.J.R. Meteorol. Soc.*, **119**, 241–267.

Bishop, C. H., 1996a: Domain independent attribution. I: Reconstructing the wind from estimates of vorticity and divergence using free space Green's functions. *J. Atmos. Sci.*, **53**, 241–252.

Bishop, C. H., 1996b: Domain independent attribution. II: Its value in the verification of dynamical theories of frontal waves and frontogenesis. *J. Atmos. Sci.*, **53**, 253–262.

Bishop, C. H. and A. J. Thorpe, 1994: Frontal wave stability during moist deformation frontogenesis. part II: The suppression of nonlinear wave development. *J. Atmos. Sci.*, **51**, 874–888.

Bjerknes, J. and H. Solberg, 1922: Life cycle of cyclones and the polar front theory of atmospheric circulation. *Geofys. Publ.*, **3**.

Bouniol, D., Y. Lemaître and A. Protat, 2002: Upper- and lower-troposphere coupling processes involved in the FASTEX IOP16 frontal cyclone. *Q. J. R. Meteorol. Soc.*, **128**, 1211–1228.

Bouniol, D., A. Protat and Y. Lemaître, 1999: Mesoscale dynamics of a deepening secondary cyclone in FASTEX IOP16: Three-dimensional structure retrieved from dropsonde data. *Q. J. R. Meteorol. Soc.*, **125**, 3535–3562.

Bromwich, D. H. and T. R. Parish, 1998: Meteorology of the antarctic. in D. Koroly and D. Vincent, editors, *Meteorology of the Southern Hemisphere*, Chap. 4, pp. 175–200. Amer. Meteor. Soc.

Brown, R. A., 1974: *Analytical Methods in Planetary-Layer Modelling.* Adam Hilger Ltd., London.

Brown, R. A., 1978: Similarity parameters from first-order closure and data. *Bound.-Layer Meteor.*, **14**, 381–396.

Brown, R. A., 1980: Longitudinal instabilities and secondary flows in the planetary boundary layer: a review. *Rev. of Geophys. and Sp. Phys.*, **18**, 683–697.

Brown, R. A., 1982: On two-layer models and the similarity functions for the planetary boundary layer. *Bound.-Layer Meteor.*, **24**, 451–463.

Brown, R. A. and G. Levy, 1986: Ocean surface pressure fields from satellite sensed winds. *Mon. Wea. Rev.*, **114**, 2197–2206.

Brown, R. A. and L. Zeng, 1994: Estimating central pressures of oceanic mid-latitude cyclones. *J. Appl. Meteor.*, **33**, 1088–1095.

Carleton, A. M., 1981: Climatology of the instant occlusion phenomenon for the Southern Hemisphere winter. *Mon. Wea. Rev.*, **109**, 177–181.

Charney, J. G., 1947: The dynamics of long waves in a baroclinic westerly current. *J. Meteor.*, **4**, 35–162.

Charney, J. G. and M. E. Stern, 1962: On the stability of internal baroclinic jets in a rotating atmosphere. *J. Atm. Sci.*, **19**, 159–172.

Conaty, A. L., J. C. Jusem, L. Takacs, D. Keyser and R. Atlas, 2001: The structure and evolution of extratropical cyclones, fronts, jet streams, and the tropopause in the GEOS general circulation model. *Bull. Amer. Meteor. Soc.*, **82**, 1853–1867.

Dickinson, S. and R. A. Brown, 1996: A study of near-surface winds in marine cyclones using multiple satellite sensors. *J. Appl. Meteor.*, **35**, 769–781.

Duchateau, P. and D. W. Zachmann, 1986: *Schaums Outline of Theory and Problems of Partial Differential Equations*. McGraw-Hill.

Eady, E., 1949: Long waves and cyclonic waves. *Tellus*, **1**, 33–52.

Harlan, J. and J. J. O'Brien, 1986: Assimilation of scatterometer winds into surface pressure fields using a variational method. *J. Geophys. Res.*, **91, D7**, 7816–7836.

Hilburn, K. A., M. A. Bourassa and J. O'Brien, 2003: Development of scatterometer-derived research-quality surface pressures for the southern ocean. *J. Geophys. Res.*, p. submitted.

Holton, J. R., 1992: *An Introduction to Dynamic Meteorology*. Academic Press.

Hoskins, B. J., 1982: The mathematical theory of frontogenesis. *Annu. Rev. Fluid Mech.*, **14**, 131–151.

Hoskins, B. J. and F. P. Bretherton, 1972: Atmospheric frontogenesis models: Mathematical formulation and solution. *J. Atmos. Sci.*, **29**, 11–37.

Joly, A., 1995: The stability of steady fronts and the adjoint method: Nonmodal frontal waves. *J. Atmos. Sci.*, **52**, 3082–3108.

Joly, A., D. Jorgensen, M. A. Shapiro, A. Thorpe, P. Bessemoulin, K. A. Browning, J.-P. Cammas, J.-P. Chalon, S. A. Clough, K. A. Emanuel, L. Eymard, R. Gall, P. H. Hildebrand, R. H. Langland, Y. Lemaître, P. Lynch, J. A. Morre, P. O. G. Persson, C. Snyder and R. M. Wakimoto, 1997: Definition of the Fronts and Atlantic Storm-Track Experiment (FASTEX). *Bull. Amer. Meteorol. Soc.*, **78**, 1917–1940.

Joly, A. and A. J. Thorpe, 1990: Frontal instability generated by tropospheric potential vorticity anomalies. *Q. J. R. Meteorol. Soc.*, **116**, 525–560.

Joly, A. and A. J. Thorpe, 1991: The stability of time-dependent flows: An application to fronts in developing baroclinic waves. *J. Atmos. Sci.*, **48**, 163–182.

Keyser, D. and M. J. Pecnick, 1985: A two-dimensional primitive equation model of frontogenesis forced by confluence and horizontal shear. *J. Atm. Sci.*, **42**, 1259–1282.

Keyser, D., M. J. Reeder and R. J. Reed, 1988: A generalization of petterssen's function and its relation to the forcing of vertical motion. *Mon. Wea. Rev.*, **116**, 762–780.

Korner, S. O. and J. E. Martin, 2000: Piecewise frontogenasis from a potential vorticity perspective: Methodology and a case study. *Mon. Wea. Rev.*, **128**, 1266–1288.

Levy, G., 1989: Surface dynamics of observed maritime fronts. *J. Atmos. Sci.*, **46**, 1219–1232.

Levy, G., 1994: Southern hemisphere low level wind circulation statistics from the Seasat scatterometer. *Ann. Geophysicae*, **12**, 65–79.

Levy, G. and R. A. Brown, 1991: Southern Hemisphere synoptic weather from a satellite scatterometer. *Mon. Wea. Rev.*, **119**, 2803–2813.

Ley, B. E. and W. R. Peltier, 1978: Wave generation and frontal collapse. *J. Atmos. Sci.*, **35**, 4–17.

Liu, W. T., 2002: Progress in scatterometer application. *J. Oceanog.*, **58**, 121–136.

Malardel, S., A. Joly, F. Courbet and P. Courtier, 1993: Nonlinear evolution of ordinary frontal waves induced by low-level potential vorticity anomalies. *Q. J. R. Meteorol. Soc.*, **119**, 681–713.

Mallet, I., P. Arbogast, C. Baehr, J.-P. Cammas and P. Mascart, 1991: Effects of a low-level precursor and frontal stability on cyclogenesis during FASTEX IOP17. *Q. J. R. Meteorol. Soc.*, **125**, 3415–3437.

McMurdie, L. A. and K. B. Katsaros, 1991: Satellite-derived integrated water-vapor distribution in oceanic midlatitude storms: Variation with region and season. *Mon. Wea. Rev.*, **119**, 589–605.

Milliff, R. F., T. J. Hoar and H. van Loon, 1999: Quasi-stationary wave variability in NSCAT winds. *J. Geophys. Res.*, **104**, 11,425–11,435.

Morgan, M. C., 1999: Using piecewise potential vorticity inversion to diagnose frontogenesis. part I: A partitioning of the Q vector applied to diagnosing surface frontogenesis and vertical motion. *Mon. Wea. Rev.*, **127**, 2796–2821.

Orlanski, I. and B. Ross, 1977: The circulation associated with a cold front. part I: Dry case. *J. Atmos. Sci.*, **34**, 1619–1633.

Orlanski, I. and B. Ross, 1984: The evolution of an observed cold front. part II: Mesoscale dynamics. *J. Atmos. Sci.*, **41**, 1669–1703.

Orlanski, I., B. Ross, L. Polinsky and R. Shaginaw, 1985: Advances in the theory of atmospheric fronts. in *Issues in atmospheric and oceanic modeling*, Vol. 28, Chap. 5, pp. 223–252. Academic Press.

Parker, D. J., 1998: Secondary frontal waves in the North Atlantic region: A dynamical perspective of current ideas. *Q. J. R. Meteorol. Soc.*, **124**, 829–856.

Parrish, D. F. and J. C. Derber, 1992: The National Meteorological Center's spectral statistical-interpolation analysis system. *Mon. Wea. Rev.*, **120**, 1747–1763.

Patoux, J., 2000: *UWPBL 3.0, the University of Washington Planetary Boundary Layer (UWPBL) model*. University of Washington.

Patoux, J. and R. A. Brown, 2001a: A scheme for improving scatterometer surface wind fields. *J. Geophys. Res.*, **106,D20**, 23,985–23,994.

Patoux, J. and R. A. Brown, 2001b: Spectral analysis of QuikSCAT surface winds and two-dimensional turbulence. *J. Geophys. Res.*, **106,D20**, 23,995–24,005.

Patoux, J. and R. A. Brown, 2002: A gradient wind correction for surface pressure fields retrieved from scatterometer winds. *J. Applied Meteor.*, **41**, 133–143.

Patoux, J., R. C. Foster and R. A. Brown, 2002: Global pressure fields from scatterometer winds. *J. Applied Meteor.*, p. in press.

Petterssen, S., 1936: Contribution to the theory of frontogenesis. *Geofys. Publ.*, **11(6)**, 1–27.

Phillips, N. A., 1956: The general circulation of the atmosphere: A numerical experiment. *Q. J. R. Meteorol. Soc.*, **82**, 123–164.

Reed, R. J. and M. D. Albright, 1997: Frontal structure in the interior of an intense mature ocean cyclone. *Wea. and Forecasting*, **12**, 866–876.

Reeder, M. J. and R. K. Smith, 1998: Mesoscale meteorology. in D. J. Koroly and D. G. Vincent, editors, *Meteorology of the Southern Hemisphere*, Chap. 5, pp. 201–241. Amer. Meteor. Soc.

Renfrew, I. A., A. J. Thorpe and C. H. Bishop, 1997: The role of environmental flow in the development of secondary frontal cyclones. *Q. J. R. Meteorol. Soc.*, **123**, 1653–1675.

Rivals, H., J.-P. Camas and I. A. Renfrew, 1998: Secondary cyclogenesis: The initiation phase of a frontal wave observed over the eastern Atlantic. *Q. J. R. Meteorol. Soc.*, **124**, 243–267.

Schär, C. and H. C. Davies, 1990: An instability of mature cold fronts. *J. Atmos. Sci.*, **47**, 929–950.

Schultz, D. M., D. Keyser and L. F. Bosart, 1998: The effect of large-scale flow on low-level frontal structure and evolution in midlatitude cyclones. *Mon. Wea. Rev.*, **126**, 1767–1791.

Shapiro, M. A. and D. A. Keyser, 1990: Fronts, jet streams, and the tropopause. in C. W. Newton and E. O. Holopainen, editors, *Extratropical Cyclones: The Erik Palmén Memorial Volume*, Chap. 5, pp. 167–191. Amer. Meteor. Soc.

Simmonds, I., 2000: Size changes over the life of sea level cyclones in the NCEP reanalyses. *Mon. Wea. Rev.*, **128**, 4118–4125.

Simmonds, I. and K. Keay, 2000: Variability of southern hemisphere extratropical cyclone behavior, 1958-97. *J. Climate*, **13**, 550–561.

Sinclair, M. R., 1997: Objective identification of cyclones and their circulation intensity, and climatology. *Wea. Forecast.*, **12**, 595–612.

Sinclair, M. R. and M. J. Revell, 2000: Classification and composite diagnosis of extratropical cyclogenesis events in the southwest pacific. *Mon. Wea. Rev.*, **128**, 1089–1105.

Thorncroft, C. D. and B. J. Hoskins, 1990: Frontal cyclogenesis. *J. Atmos. Sci.*, **47**, 2317–2336.

Wakimoto, R. M. and H. Cai, 2002: Airborne observations of a front near a col during FASTEX. *Mon. Wea. Rev.*, **130**, 1898–1912.

Williams, R. T., 1967: Atmospheric frontogenesis: A numerical experiment. *J. Atmos. Sci.*, **24**, 627–641.

Williams, R. T., 1974: Numerical simulation of steady-state fronts. *J. Atmos. Sci.*, **31**, 1286–1296.

Yeh, H.-C., G.-J. Chen and W. Liu, 2002: Kinematic characteristics of a Mei-yu front detected by the QuikSCAT oceanic winds. *Mon. Wea. Rev.*, **130**, 700–711.

Yuan, X., D. J. Martinson and W. T. Liu, 1999: The effect of air-sea interaction on winter 1996 Southern Ocean subpolar storm distribution. *J. Geophys. Res.*, **104**, 1991–2007.

Zierden, D. F., M. A. Bourassa and J. J. O'Brien, 2000: Cyclone surface pressure fields and frontogenesis from NASA scatterometer (NSCAT) winds. *J. Geophys. Res.*, **105**, 23,967–23,981.

Appendix A

LOW-PASS FILTER

For a given field $f(x,y)$ defined at (x_i, y_j), $i = 1, N_i$, $j = 1, N_j$, of a regular grid, the filtered value $\overline{f}$ at (x_0, y_0) is defined as:

$$\overline{f}(x_0, y_0) = \frac{1}{W} \sum_{i=1}^{N_x} \sum_{j=1}^{N_y} w_{ij} f(x_i, y_j) \tag{A.1}$$

where the weighting coefficients w_{ij} are defined as:

$$w_{ij} = \begin{cases} (1 - D_{ij}^3)^3 & \text{if } 0 \leqslant D \leqslant 1 \\ 0 & \text{otherwise} \end{cases} \tag{A.2}$$

with

$$D_{ij} = \left(\left(\frac{x_i - x_0}{h_x} \right)^2 + \left(\frac{y_j - y_0}{h_y} \right)^2 \right)^{1/2} \tag{A.3}$$

$$W = \sum_{i=1}^{N_x} \sum_{j=1}^{N_y} w_{ij} \tag{A.4}$$

and h_x,h_y the filtering scales in the zonal and meridional directions respectively. Figure A.1a shows how the weight decreases as a function of distance. Figures A.1b and A.1c show the impact of the filter on the power spectrum of a randomly generated series.

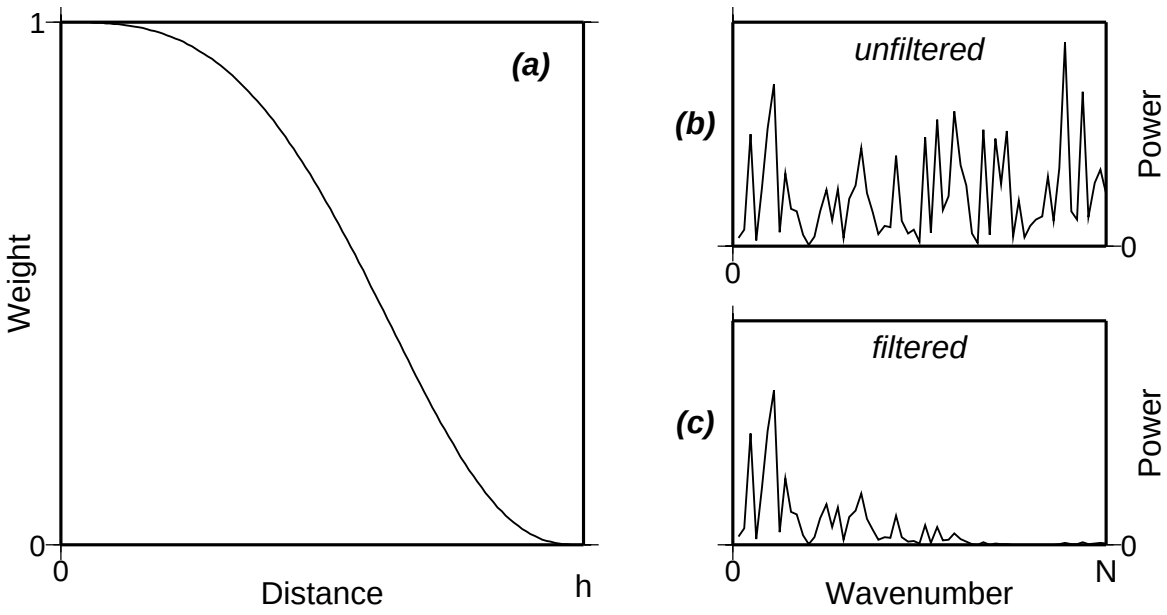

Figure A.1: (a) Weight of the low-pass filter as a function of distance (b) Power spectrum of a randomly generated series (c) Power spectrum of the filtered series

Appendix B

GREEN'S FUNCTION FOR THE LAPLACIAN

The solution to

$$\nabla^2(\phi) = \delta(\boldsymbol{x}) \qquad in\ \mathbb{R}^2\ \ or\ \mathbb{R}^3 \tag{B.1}$$

where $\delta(\boldsymbol{x})$ is the Dirac distribution, is often mentioned in textbooks but rarely derived completely. Bender and Orszag (1978) solve it in one dimension whereas Duchateau and Zachmann (1986) leave it as an exercise to the reader. Ablowitz and Fokas (1997) suggest a lengthy derivation using Fourier and inverse Fourier transforms in x and y. A simpler derivation follows.

In two dimensions, the problem is first converted to cylindrical coordinates and becomes:

$$\frac{\partial^2\phi}{\partial r^2} + \frac{1}{r}\frac{\partial\phi}{\partial r} + \frac{1}{r^2}\frac{\partial^2\phi}{\partial\theta^2} = \delta(r)\delta(\theta) \tag{B.2}$$

By circular symmetry, the third term on the left is zero and the homogeneous solution to the resulting equation is:

$$\phi(r) = C_1 \ln(r) + C_2 \tag{B.3}$$

where the constant C_2 is of little interest here and can be set to zero (in physical terms, if the whole streamfunction or velocity potential is increased or decreased by a constant, the corresponding wind field is unchanged). The constant C_1 is obtained by integrating the original equation on a disk D of radius ϵ centered at the origin:

$$\oint_D \nabla^2\phi dA = \oint_D \delta(r) dA \tag{B.4}$$

By definition of the Dirac distribution, the right-hand side is 1. Using Gauss' theorem, the left-hand side can be written:

$$\oint_D \nabla^2 \phi dA = \oint_D \boldsymbol{\nabla}.\boldsymbol{\nabla}\phi dA = \oint_C \boldsymbol{\nabla}\phi.\boldsymbol{n} ds = \oint_C \frac{\partial \phi}{\partial r} ds \tag{B.5}$$

where C is the boundary of the disk and bold letters represent vectors (note that the first two integrals are two-dimensional - on the disk D - and the last two integrals are one-dimensional - on the circle C). Using $\partial\phi/\partial r = C_1/r$, equation B.4 becomes:

$$\int_0^{\epsilon} \int_0^{2\pi} \frac{C_1}{r} r d\theta = \int_0^{2\pi} C_1 d\theta = 2\pi C_1 = 1 \tag{B.6}$$

which yields the final solution:

$$\phi(r) = \frac{1}{2\pi} \ln(r) \tag{B.7}$$

In $\mathbb{R}^3$, the problem is converted to spherical coordinates and becomes:

$$\frac{\partial^2 \phi}{\partial r^2} + \frac{2}{r}\frac{\partial \phi}{\partial r} + \frac{1}{r^2 sin\theta}\frac{\partial}{\partial \theta}\left(sin\theta \frac{\partial}{\partial \theta}\right)\phi + \frac{1}{r^2 sin^2\theta}\frac{\partial^2 \phi}{\partial \lambda^2} = \delta(r)\delta(\theta)\delta(\lambda) \tag{B.8}$$

By circular symmetry, the problem becomes:

$$\frac{\partial^2 \phi}{\partial r^2} + \frac{2}{r}\frac{\partial \phi}{\partial r} = \delta(r) \tag{B.9}$$

which has as homogeneous solution:

$$\phi(r) = C_1/r \tag{B.10}$$

(the constant C_2 has been set to zero). The constant C_1 is obtained by integrating the original equation on a sphere Ω of radius ϵ centered at the origin:

$$\oint_\Omega \nabla^2 \phi dV = \oint_\Omega \delta(r) dV \tag{B.11}$$

By definition of the Dirac distribution, the right-hand side is 1. Using Gauss' theorem, the left-hand side can be written:

$$\oint_\Omega \nabla^2 \phi dV = \oint_\Omega \boldsymbol{\nabla}.\boldsymbol{\nabla}\phi dV = \oint_S \boldsymbol{\nabla}\phi.\boldsymbol{n} dA = \oint_S \frac{\partial \phi}{\partial r} dA \tag{B.12}$$

where S is the surface of the sphere (note that the first two integrals are three-dimensional - on the sphere Ω - and the last two integrals are two-dimensional - on the surface S). Using $\partial\phi/\partial r = -C_1/r^2$, equation B.11 becomes:

$$\int_0^{\epsilon}\int_0^{2\pi}\int_0^{\pi}\frac{-C_1}{r^2}r^2 sin\theta dr d\lambda d\theta = 2\pi\int_0^{\pi} -C_1 sin\theta d\theta = -4\pi C_1 = 1 \tag{B.13}$$

which yields the final solution:

$$\phi(r) = \frac{-1}{4\pi r} \tag{B.14}$$

VITA

Jérôme Patoux

Education:

Ph.D., Atmospheric Sciences, University of Washington (Seattle), 2003. Thesis: "Frontal wave development over the Southern Ocean".

Diplôme d'Études Approfondies, Université Paul Sabatier (Toulouse, France), 1997 - Thesis: "Étude de la Variabilité de l'océan dans les bassins Açores et Canaries (Study of the ocean variability in the Azores and Canaries basin)".

M.S., University of Texas at Austin, 1994. Thesis: "Water balance of Texas".

Engineering Degree, École Centrale de Lille (Lille, France), 1993.

Employment:

1993, Research Internship, Ocean Physics Lab, Université de Bretagne Occidentale, Brest, France.

1993-1995: Research Assistant, University of Texas at Austin.

1994: Teaching Assistant, University of Texas at Austin.

1995-1996: Research Cooperation, ORSTOM (Research Institute for Development in Cooperation), Antofagasta, Chile.

1997: Research Internship, CLS (Collecte, Localisation, Satellite), Toulouse, France.

1999, 2001: Teaching Assistant, Department of Atmospheric Sciences, University of Washington.

1999, NASA Space Grant mentor, University of Washington.

1999, 2000: Seattle School District Summer Science Teacher.

1997-2003: Research Assistant, Department of Atmospheric Sciences, University of Washington.

Publications:

Journal articles:

Patoux, J. and R.A. Brown, 2001: Spectral analysis of QuikSCAT surface winds and two-dimensional turbulence. *Journal of Geophysical Research*, **106**, D20, 23,995-24,005.

Patoux, J. and R.A. Brown, 2001: A scheme for improving scatterometer surface wind fields. *Journal of Geophysical Research*, **106**, D20, 23,985-23,994.

Patoux, J. and R.A. Brown, 2002: A gradient wind correction for surface pressure fields retrieved from scatterometer winds. *Journal of Applied Meteorology*, **41**, 133-143.

Patoux, J. and R.A. Brown, 2003: Global pressure fields from scatterometer winds, *Journal of Applied Meteorology* (in press).

Conference Proceedings:

"QuikSCAT analysis of marine atmospheric fronts", J. Patoux and R. A. Brown, AMS Annual Meeting, February 9-13, 2003, Long Beach, CA.

"Analysis of midlatitude storms with winds and pressures from QuikSCAT", R. A. Brown and J. Patoux, AMS Annual Meeting, February 9-13, 2003, Long Beach, CA.

"Global pressure fields from scatterometer winds", J. Patoux, R. C. Foster and R. A. Brown, AMS Annual Meeting, February 9-13, 2003, Long Beach, CA.

Awards:

Rotary outstanding student travel award, Essen, Germany, 1989.

Lavoisier Scholarship, Paris, France, 1993.

Scholarship, Université Paul Sabatier, Toulouse, France, 1996.

Project Kaleidoscope PKAL fellowship, Keystone, CO, 2000.